FLOW BOILING OF R245FA IN MICROGAPS WITH STAGGERED CIRCULAR AND HYDROFOIL PIN FINS

A Dissertation
Presented to
The Academic Faculty

by

Pouya Asrar

In Partial Fulfillment
of the Requirements for the Degree
Doctor of Philosophy in the
School of Mechanical Engineering

Georgia Institute of Technology
December 2018

FLOW BOILING OF R245FA IN MICROGAPS WITH STAGGERED CIRCULAR PIN FINS

Approved by:

Dr. Yogendra K. Joshi, Chairman
School of Mechanical Engineering
Georgia Institute of Technology

Dr. Muhannad S. Bakir
School of Electrical and Computer Engineering
Georgia Institute of Technology

Dr. S. Mostafa Ghiaasiaan
School of Mechanical Engineering
Georgia Institute of Technology

Dr. Satish Kumar
School of Mechanical Engineering
Georgia Institute of Technology

Dr. Suresh K. Sitaraman
School of Mechanical Engineering
Georgia Institute of Technology

Date Approved: [Nov. 2, 2018]

To

My Loving Family

ACKNOWLEDGEMENTS

Firstly, I would like to express my deep gratitude to my advisor, Professor Yogendra K. Joshi, for his crucial research guidance, continuous support of my Ph.D. study and related research, for his patience, and immense knowledge. Besides my advisor, I would like to thank Professor S. Mostafa Ghiaasiaan for his ever present support especially during the last stages of my Ph.D. journey. I am also thankful to my other committee members, Dr. Sitaraman, Dr. Bakir, and Dr. Kumar for their support and valuable advice. My sincere thanks also goes to the staff members of the Mechanical Engineering departments Ms. Glenda Johnson, Ms. Camellia Henry, and Katherine Drake who have always been helpful and present to assist. I will be always thankful for the opportunity that I was given in this department to learn and to grow.

I thank my fellow labmates in METTL lab for the stimulating discussions, for the sleepless nights we were working together before deadlines, and for all the fun we have had in the last five years: Daniel Lorenzini, Sangbeom Cho, Justin Broughton, Thomas Sherer, Trevar Kingston, Michael Delfanti, Steven Isaac, and many others. I thank my friends in the Mechanial Engineering department . In particular, I am grateful to Dr. Craig Green for enlightening me the first glance of research.

I would like to thank my close friends, Kamal Shadi, Hadi Panahi, and Amir Hossein Salahshour for their encouragement and unconditional support.

Furthermore, I appreciate incredible support of my beautiful wife, Neda, during my Ph.D. program. I am also grateful to my lovely parents, Manijeh and Ahmad as well as my

adorable siblings, Paria and Pouriya. This dissertation would not have been possible without their warm love, continued patience, and endless support.

TABLE OF CONTENTS

LIST OF TABLES

LIST OF FIGURES

LIST OF SYMBOLS AND ABBREVIATIONS

A_{cf} pin fin cross-sectional area, m^2

A_p footprint area of the microgap, m^2

A_s surface area, m^2

C_p specific heat, kJ/(kg K)

D_h hydraulic diameter, m

H microgap height, m

$\bar{h}_{sp}$ average single-phase heat transfer coefficient,

$W/(m^2K)$

$\bar{h}_{tp}$ average two-phase heat transfer coefficient, $W/(m^2 K)$

I electrical current, A

k_s silicon thermal conductivity, W/(m K)

k_f fluid thermal conductivity, W/(m K)

L microgap length, m

L_{sp} single-phase region length, m

L_{tp} two-phase region length, m

m_f fin parameter

$\dot{m}$ mass flow rate, kg/s

N_f number of pin fins

P_f pin fin perimeter, m

q'' heat flux, W/cm^2

q''_{loss} heat flux loss, W/cm^2

q''_{eff} effective heat flux, W/cm^2

R_{total} Total chip thermal resistance, (K/W)

t_s silicon block thickness, m

t_p SiO_2 passivation layer thickness, m

$\bar{T}$ average surface temperature, ^oC

$\bar{T}_H$ average heaters temperature, ^oC

T_{in} fluid inlet temperature, ^oC

T_{out} fluid outlet temperature, ^oC

T_{sat} saturation temperature, ^oC

T_{se} surface temperature at the end of single-phase region, ^oC

T_{si} surface temperature at the inlet, ^{o}C

$\bar{T}_{sp}$ average single-phase region temperature, ^{o}C

$\bar{T}_{surf}$ average surface temperature, ^{o}C

$\bar{T}_{tp}$ average two-phase region temperature, ^{o}C

V Applied Voltage to the chip, V

W microgap width, m

S_L Longintudinal Pitch

Greek symbols

η_f fin efficiency

Subscripts

tp two-phase

sp single-phase

SUMMARY

Dielectric fluids, including refrigerants, are electrically inert and are a good candidate as working fluid in two-phase microsystem cooling applications. In this study, R245fa is investigated for flow boiling in microgaps with height of 200 μm, spacing in the ranges of 200-225 μm (dense device) and 400-450 μm (sparse device) are studied. For heat fluxes up to 498 W/cm^2, mass flux values ranging from 193 kg/m^{2}s to 7896 kg/m^{2}s and inlet temperatures ranging from 10 ^{o}C to 18 ^{o}C, average two-phase heat transfer coefficient up to 60 kW/m^{2}K the devices are tested. High speed flow visualizations at frame rate of 2229 fps elucidate the flow boiling patterns inside the microgaps. The visualizations have shown different two-phase flow regimes such as bubbly, foggy, and slug flows that are generated in the pin finned area. The surface temperature values are calculated based on the obtained heaters temperature data and are plotted against the dissipated power for a wide range of heat flux for each experiment. An uncertainty analysis is also performed for the reported data. Single-phase and two-phase heat transfer coefficients and a comprehensive flow regime mapping is represented as part of this documentation. Also, pressure drop and heat transfer coefficients characterizations are done by developing correlations for single-phase and two-phase pressure drops, single-phase and two-phase heat transfer coefficients that perfectly match on all experimental data from devices.

CHAPTER 1. INTRODUCTION

Microfluidic cooling has been demonstrated to achieve relatively high heat removal capacity using microchannels and microgaps via single-phase and two-phase cooling [1-4]. To further enhance the cooling capacity, the frontal flow surface area can be increased by integrating microscale pin fins extending from bottom to top of the flow passage [5]. Flow boiling in a microgap can provide improved thermal performance compared to single-phase flow condition at similar flow rates (Reeser et al. 2014; Woodcock et al. 2015). Surface heat fluxes in excess of 100 W/cm^2 in microsystems have driven the interest in single phase liquid, and phase change cooling. Studies have shown that in pre-cooled flow boiling situations, the flow behavior changes less with variation of heat flux compared to higher inlet temperature conditions. In fact, subcooled boiling can enhance convective heat transfer coefficient and make delay on critical heat flux. It also play a significant role in bubbles formation and growth in microchannels. At a given wall temperature, subcooling can result in an increase in the maximum heat flux. [6-9].

1.1 Flow Boiling in Microchannels

Two-phase flow in the interconnectors with microchannels have been considered a promising tool in advancing electronics technology [10-15]. There has been numerous work in the literature focusing on two-phase flow investigation in microchannels in the past decade [11, 16-25]. Flow boiling in narrow volumes creates independent regimes depending on the operating conditions. In fact, size and shape of the microchannel can directly affect the appearance of these regimes, and may change the heat transfer performance [26]. Yen et al. [27] investigated the visualization of convective flow boiling

in two different types of microchannels: square and circular. They found out that the number of nucleation bubbles are more in the square shape microchannel than the circular types. This proved that square microchannel had performed better in terms of heat removal capacity. Different regimes of flow boiling such as bubbly, plug, and annular patterns were observed using a high-speed camera. A periodic [28] variation in flow regimes was concluded by the flow visualizations for both square and circular shape channels.

Different regimes of flow boiling in the microchannels such as slug, confined annular, and bubbly have been observed carefully. At each of these regimes, knowing the transition point; the heat flux and mass velocity of vapor can be individually calculated. Microchannel size can directly affect the appearance of these regimes and may change the heat transfer performance of the microchannel [26]. Bogojevic et al. [28] investigated the flow boiling instabilities by looking at bubble dynamics. The microchannel had 40 rectangular channels. They utilized deionized water as the working fluid for mass fluxes ranging between 7-204 kg/m^2s. Using a microscope and a high-speed camera the effect of heat flux and mass flux on bubble growth was investigated. They categorized the bubbles grown in the microchannel into two different types: bottom wall bubbles and sidewall bubbles. The projected area of bottom wall bubbles and sidewall bubbles were observed to be a circle and a truncated circle, respectively. The diameter of the circle was considered as the reference to determine the bottom wall bubble growth whereas the height of the bubble was measured to be reported as the sidewall bubble growth.

Flow morphologies for a range of mass fluxes were studied by Kuo et al. [29]. They considered 200 μm × 253 μm parallel microchannels for a range of mass flux between 83 kg/m^2s to 303 kg/m^2s. Bubbly flow was only detected for a limited range of mass velocity

of flow. For heat fluxes as high as 53 W/cm^2 the flow was recognized to experience a direct transition from single phase to slug flow.

Flow boiling instabilities of water in 8 microchannels for a range of heat flux and mass were visualized by Wang et al. [30]. The microchannels were arranged in parallel, as well as on a single microchannel. For the first experiment, the flows running in each channel had interactions with each other at the header of microchannels.

Microchannels are characterized here as having $D_h < 1$mm and $W/H \leq 10$. Here D_h is the hydraulic diameter given by $2WH/(W+P)$ for a rectangular duct. For $D_h < 1$mm and $W/H > 10$, we employ the term microgap. Both are often enhanced with microstructures, such as micropillars, or micro-pin arrays. Spanwise flow enabled in the microgap may mitigate two-phase flow instabilities by enabling better temperature uniformity across the heat sink. Additionally the pin fins also provide the ability to route vertical electrical and fluidic interconnections in 3D electronics, where multiple chips may be stacked. Increased flow frontal surface area enabled through microstructures strongly enhances the convective heat transfer performance. Using microfabrication techniques, the pin fins can be fabricated in different cross-sectional shapes such as square, circular, hydrofoil, and piranha, and arranged in-line, or staggered along the microgap [5, 12, 31-34].

1.2 Flow Boiling in Microgap

Increasing flow frontal surface area strongly enhances the heat transfer performance in the microfluidic devices. Microgaps with microstructures such as pin fins represent this

topic in two phase studies. The pin fins are fabricated in different shapes such as square, circular, hydrofoil, and piranha shapes. They are also either arranged via in-line or staggered patterns across the microgap [12, 31-47]. A recent work has shown that the staggered square shape pin-fin arrays causes higher pressure drop than the in-line pattern with the same base area in both of arrangements [33]. Hydrofoil pin-fins are typically designed to gain higher surface area and therefore higher heat transfer performance compared to the circular pin-finned microgaps [32, 35]. Two-phase flow in extremely small clearance geometries of microgap (in the range of a few hundreds of μm) guarantees the potential for hundreds of W/cm^2 of heat flux dissipation [5, 48-55].

Kosar et al. [56] studied two-phase flow of R-123 refrigerant in a microgap populated with hydrofoil arrays of pin fins. In a wetted perimeter of 1,030 μm, they tested the chip for a range of heat flux between 19-312 W/cm^2 and mass flux of 976-2,349 kg/m^2s. The heat transfer coefficient showed an increasing trend by increasing heat flux until the maximum value was reached. The convective boiling heat transfer mechanism was dominant at high heat fluxes which caused the heat transfer coefficient to decrease.

Isaacs et al. [31] considered a 1×1 cm silicon mircochannel having circular pin fins of 150 μm diameter. They studied the two-phase flow of refrigerant R245fa as the working fluid running around a thermal loop. They visualized the flow inside the microgap and were able to identify the vapor nucleation zones. They found out that those locations are strongly dependent on the heat flux range. They observed the triangle-shaped wakes for low heat fluxes and high flow rates towards the end of the microgap.

1.3 Working Fluid Candidates

There is a wide variety of coolants that have been considered as working fluid in the two-phase cooling systems. De-ionized (DI) water, the most accessible and low-cost liquid with high thermal capacity and conductivity, has been utilized in numerous flow boiling studies [57-64]. However, one of the drawbacks of using water is that its saturation temperature at atmospheric pressure is too high for electronic cooling purposes [59]. On contrary, dielectric fluids such as refrigerants are electrically inert and have been recently selected as working fluids in many electronic cooling systems. There are coolants that are commonly utilized in the flow boiling investigations such as R245fa, R134a, R113, and R123. These refrigerants are dielectric liquids and are safe to be in direct contact with electronic components in the system since they are chemically and electrically inert. Refrigerants such as R134a need to operate at high pressures at the electronics devices relevant temperatures. This adds additional considerations for mechanical strength of the flow thermodynamic system. R245fa refrigerant is one of the dielectric fluids that has been used in centrifugal chillers for cooling purposes and in Organic Rankine Cycles for energy recovery systems. R245fa has saturation temperature of 15.3 ^{o}C at atmospheric pressure. This characteristic allows R245fa to be a good candidate for electronic cooling field [65-67].

1.4 Research Objectives

There has been limited number of works in the literature on investigation of two phase flow of refrigerants in enhanced microgap. Also, flow boiling of refrigerants in microgaps as large as 1 cm^2 has not been studied in the literature. Two silicon chips with two different pin fin configurations inside the microgap are considered for investigating the flow boiling of R245fa. The objectives of this research are:

- Investigation of flow boiling of R245fa as working fluid running in microgaps with four different pin fin configurations.
- Investigation of the flow regimes using high speed flow visualizations which in order to obtain a comprehensive understanding of fluid behavior in the microgap.
- Investigation of flow mapping based on the recorded flow visualizations as well as the thermal measurements.
- Developement Pressure drop, single-phase and two-phase heat transfer coefficient correlations that match all experimental data from four chips.

A comprehensive experimental study was conducted to analyze the flow boiling pattern of R245fa refrigerant and thermal performance of semiconductor chips through which above-mentioned working fluid. The structures are circular pin fins and hydrofoil pin fins with a diameter of 150 μm and horizontal and vertical pitches in the range of 250-450 μm and200-400 μm, respectively. The chips have only one inlet and one outlet which can easily be applied in the design of 3D IC stacked systems. Moreover, the foot print area for all tested devices has dimension 1 cm x 1cm. This guarantees that the flow length is long enough to be considered in CMOS fabrications. The maximum heat flux of ~500 W/cm^2, coolant mass flux of 7896 kg/m^2s, and maximum exit vapor quality of about unity are assessed.

CHAPTER 2. EXPERIMENTAL SETUP AND DATA REDUCTION

2.1 Experimental Flow Loop

Figure 2.1 depicts the schematic of the closed loop assembled using 6.35 mm OD stainless steel tubes and Swagelok fittings. The system is initially evacuated by a vacuum pump (VN-200N, JB Industries Inc.) to a pressure of 4 kPa to ensure that the air inside the loop is removed. A refrigerant source tank heated up to a temperature up to 15 ^{o}C above the ambient (50 ^{o}C) is connected to the control valve (charging point) to introduce the working fluid to the system. In order to have the flow always going towards the syringes, the accumulator is heated up to 15 ^{o}C above the room temperature. By having one syringe pushing and the other one pulling, continuous flow around the loop is ensured. There are multiple check valves upstream of each syringe pump that guarantee the flow runs only from the pumps to the rest of the loop (no back flow to the syringes). Initially, the refrigerant passes through the pre-cooler to insure liquid phase. It then enters the flow meter (S-114, Mcmillan Co.). Particulate contaminants are removed by running the refrigerant through a 0.5 μm in-line filter (SS-4F-05, Swagelok Co.). A back-wash circuit is incorporated at the test section zone to clean the chip prior to the actual test. It enables running the refrigerant through the test device in both directions. A liquid-to-liquid nickel brazed plate heat exchanger (LL510G14, Lytron Co.) is located right after the test section to bring back the refrigerant into liquid phase, before returning it back to the accumulator. A high-speed video camera (Phantom V211, VISION Research Inc.) is utilized to capture the flow boiling phenomena inside the microgap at 2,229 fps.

In order to assure steady state conditions prior to each thermal test, the system is run with the test chip unpowered for a few hours. Temperature and pressure values around the loop are collected and recorded by the data acquisition unit (Agilent 34972A, Keysight Technologies). Once temperature and pressure data are stabilized (0.1 ^{o}C for temperature and 0.5 kPa for pressure), the heater powers are incremented gradually, starting from heat flux of ~1 W/cm^2. The fluid temperature is obtained at 5 different locations in the loop, including immediately before inlet, and after the outlet of the device, using 1.56 mm diameter thermocouple probes (OMEGA TMQSS-062G). Also, four pressure transducers (OMEGA PX219-100A5V) provide the fluid pressure measurement around the loop.

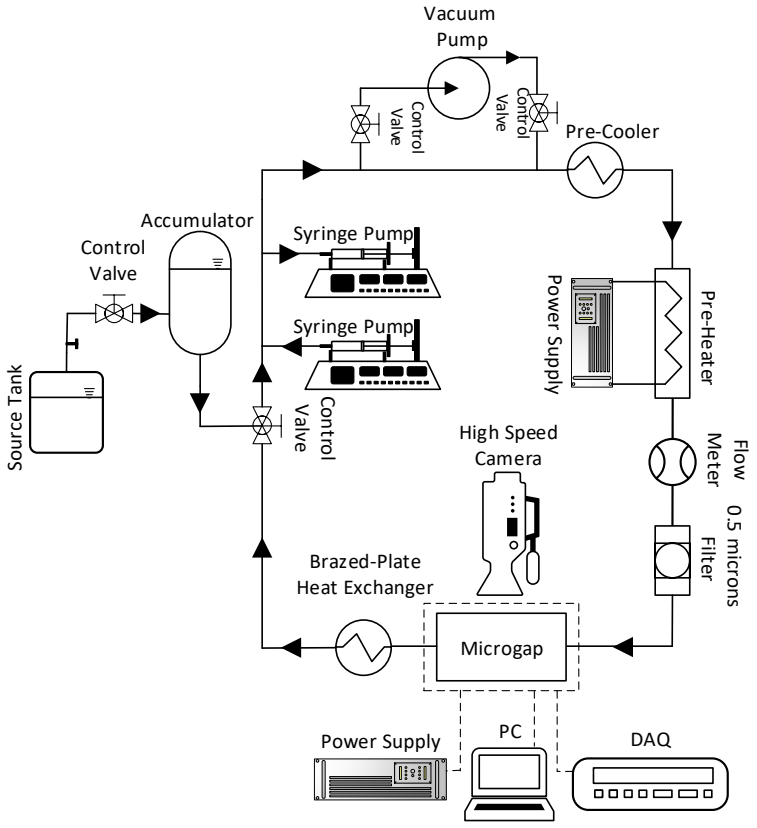

Figure 2.1 Flow loop schematic

2.2 Data Reduction

The voltage and current values are utilized to calculate the input power to the chip. A heat loss experiment is also performed under vacuum condition in the loop to assess heat loss to ambient and from the package. This was found to be 1% or less for all cases and was subtracted from the input power:

$$q" = VI/A_s \tag{1}$$

$$q"_{eff} = q" - q"_{loss} \tag{2}$$

2.2.1 Single-phase heat transfer

The average surface temperature is calculated by assuming 1-D conduction through the silicon layer at the bottom of the chip:

$$\bar{T}_{surf} = \bar{T}_H - q"_{eff} A_s t_s/(k_s A_p) \tag{3}$$

$$q"_{eff} A_s = \bar{h}_{sp}(\eta_f N_f P_f H + WL - N_f A_{cf})[\bar{T} - \frac{T_{in} + T_{out}}{2}] \tag{4}$$

$$\eta_f = \frac{\tanh(m_f H)}{m_f H} \text{ where } m_f = \sqrt{(\bar{h}_{sp} P_f)/(k_f A_{cf})} \tag{5}$$

$$T_{out} = T_{in} + q"_{eff} A_s/(\dot{m} C_p) \tag{6}$$

Where the fin efficiency, η_f, is calculated using the adiabatic expression.

2.2.2 Two-phase heat transfer

The microgap is divided into two separate regions: a single-phase region where no boiling was observed, and a two-phase region where the flow boiling was occurring. It is assumed that the single-phase heat is all transferred to the two-phase flow. Based on the high-speed flow visualizations, these regions are determined. The inlet, outlet, and average

wall temperature values for the single-phase region are obtained by the following equations:

$$T_{si,sp} = T_{in} + q"/\bar{h}_{sp} \quad (7)$$

$$T_{se,sp} = T_{sat} + q"/\bar{h}_{sp} \quad (8)$$

$$\bar{T}_{sp} = (T_{si,sp} + T_{se,sp})/2 \quad (9)$$

Using a weighted average of the single-phase and two-phase temperatures, the average temperature of the two-phase region is calculated by:

$$R_{total} = (t_p/k_p + t_s/k_s)/A_p \quad (10)$$

$$\bar{T} = \bar{T}_H - \left(q"_{eff} A_s\right) R_{total} \quad (11)$$

$$\bar{T}_{tp} = (\bar{T}L - \bar{T}_{sp} L_{sp})/L_{tp} \quad (12)$$

The single-phase and two-phase lengths are obtained based on the flow visualizations. The lengths are determined based on the number of pin fin columns under either single-phase and two-phase condition.

Finally, the average two-phase heat transfer coefficient is obtained using the Newton's law of cooling as follows:

$$q"_{eff} A_s = \bar{h}_{tp}(\eta_f N_f P_f H + WL - N_f A_{cf})[\bar{T}_{tp} - T_{sat}] \quad (13)$$

2.2.3 Uncertainty Analysis

The Kline-McClintock method is applied to calculate the uncertainty in the reported results, based on determination of the uncertainties of multiple primary measurements [31]. Thermocouples are calibrated in the range of 19 ºC to 110 ºC using a four-wire precision

platinum thermometer connected to a heating and cooling block calibrator (OMEGA CL122). Pressure transducers are calibrated using a pressure calibrator (OMEGA DPI 610).

CHAPTER 3. FLOW BOILING OF R245FA IN A MICROGAP WITH DENSE CIRCULAR PIN FIN STRUCTURE

In this chapter, flow boiling of refrigerant R245fa is investigated in a microgap of height 200 μm populated with a staggered pin fin array of diameter 150 μm and spacing 200 μm. For heat fluxes up to 498 W/cm^2, mass flux values up to 7,896 kg/m^{2}s, and inlet temperatures of 13 ^{o}C and 18 ^{o}C, average two-phase heat transfer coefficient up to 60 kW/m^{2}K are measured. High speed flow visualizations at frame rate of 2,229 fps elucidate the flow boiling patterns inside the microgaps, including bubbly and foggy that are generated in the pin finned area. Surface temperatures are measured for heat fluxes up to to 498 W/cm^2 which enable determination of heat transfer characteristics.

3.1 Test Vehicle Configuration

The schematic of the test package is depicted in Figure 3.1 The package is made of Polyether ether ketone (PEEK), which has a melting point of 343 ^{o}C. The device is placed in the pocket at the center of the package, and sealed by O-rings. Finally, a printed circuit board (PCB) is placed around the chip, which is wirebonded to provide electrical power. Refrigerant compatible Chemraz O-rings (Wyatt Seal Co.) are used to seal the I/O, as well as measurement ports on the back of the chip.

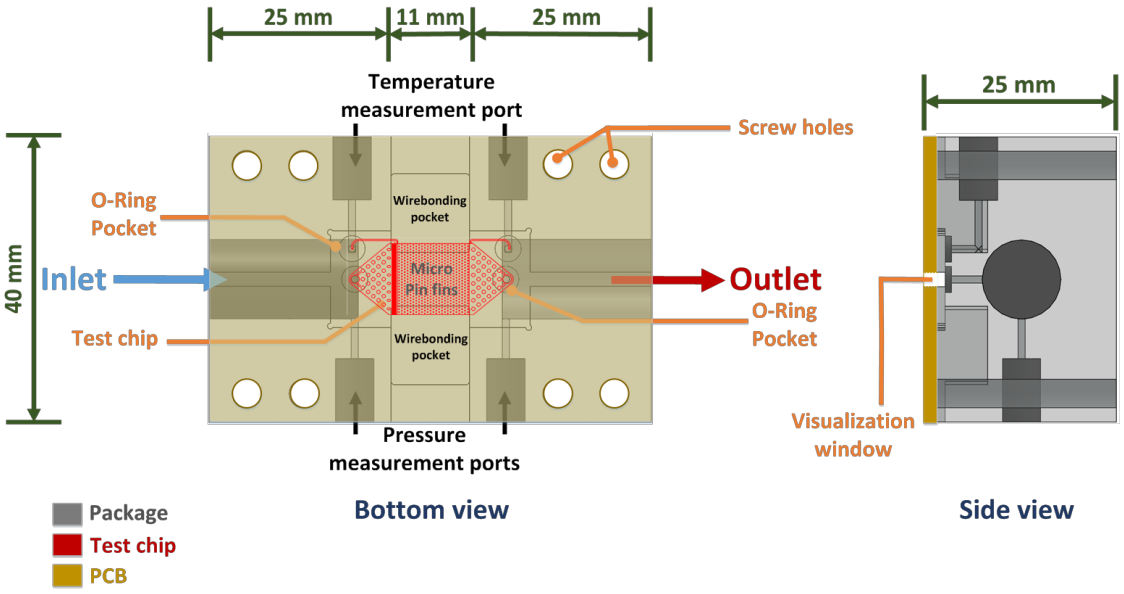

Figure 3.1 Test vehicle components

Figure 3.2 shows the schematic of the test chip, including the key dimensions. The device has a 1 cm^2 pin finned area. Four columns of oval flow redistribution pin fins upstream of the microgap pin fins direct the incoming fluid to the test region. The redistribution pin fins also provide a large pressure drop to prevent backflow due to two-phase flow instabilities. Mechanical support pins of 500 µm were added near the inlet and outlet for enhancing structural strength. In addition to fluid inlet and outlet ports, pressure ports are also included on either side of the micro-pin fin array to accurately measure pressure drop across it, while excluding pressure drop due to rapid flow constriction/expansion at the inlet and outlet ports.

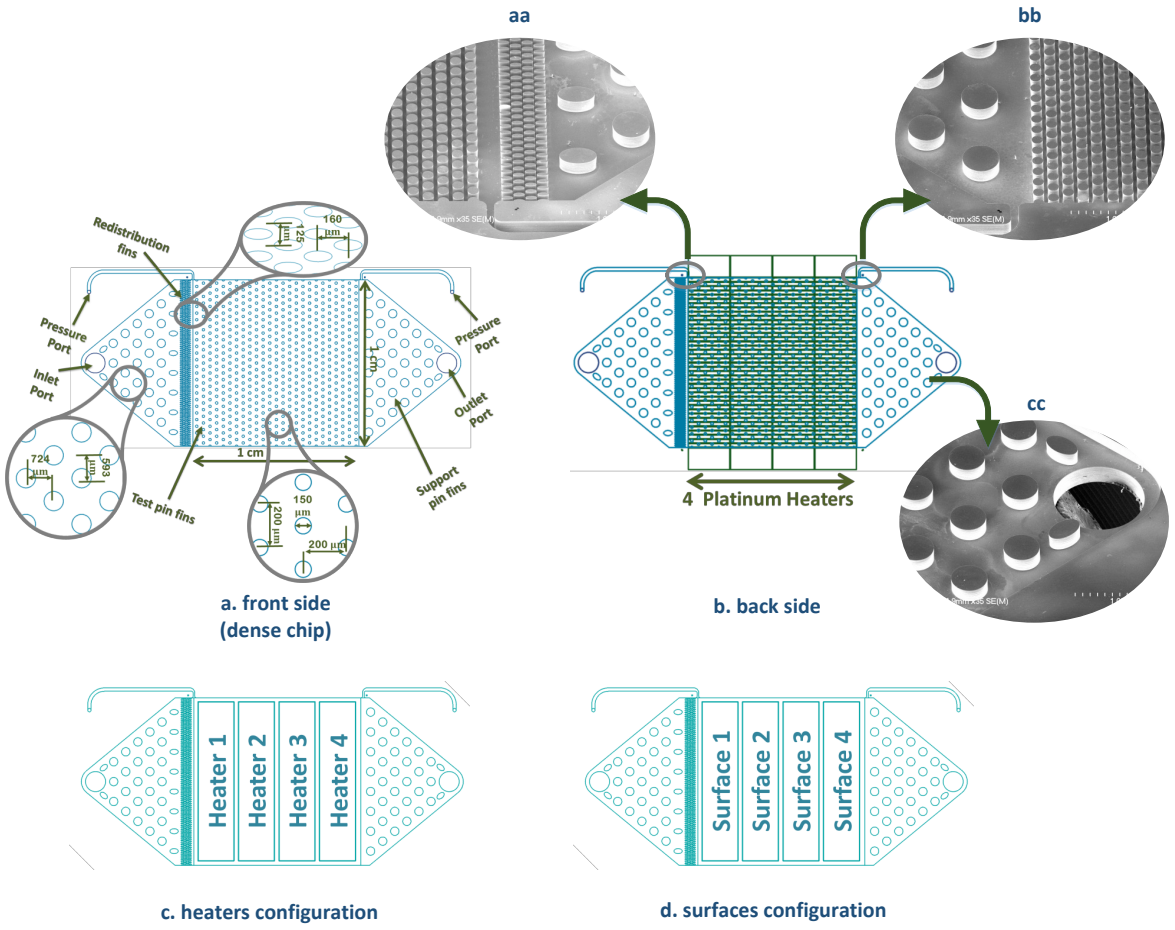

Figure 3.2 Detailed chip configuration

Four serpentine platinum heaters are deposited on the back of the chip, which provide power, and also serve as resistance temperature detector (RTDs). The chip is placed in an oven whose temperature is ramped up to 140 ºC before turning it off. The calibration process is done through a quasi-steady-state when the oven is turned off and the chip is cooled off over about 7 hours Figure 3.3 shows a representative calibration curve, which is nearly linear. At the beginning, the cooling is faster due to the larger difference between the heater and the ambient temperature.

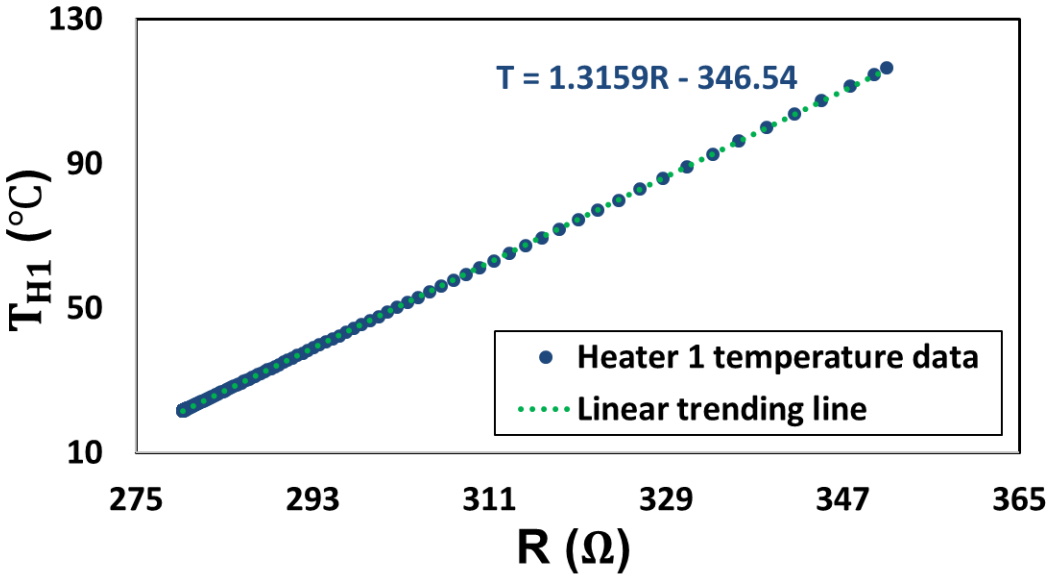

Figure 3.3 A representative calibration curve (heater 1)

3.2 Chip Manufacturing Process

Microfabrication process used to fabricate the surface enhanced microgap is shown in Figure 3.4. It starts with a 500 μm thick double side polished wafer. A standard Bosch process with alternating SF_6 (for etching) and C_4F_8 (for Si passivation) was used to create the 200 μm height micropin-fins and manifolds. Next, the etched silicon wafer was cleaned with piranha solution (5:1 mixture of 98% sulfuric acid and 30% hydrogen peroxide) at 125 ^oC. The cavities formed during etching were capped with a pyrex wafer using anodic bonding with voltage of 800 V at 350 ^oC. The bonded wafer was then flipped over, and a 1 μm thick insulating silicon dioxide layer was deposited using chemical vapor deposition (CVD). 200 nm thick Platinum heaters and 500 nm thick gold pads were then deposited on the SiO_2 layer. Another 1 μm thick silicon dioxide passivation layer was deposited on the heater for protection and thermal isolation. Lastly, inlet, outlet, and pressure measurement ports were etched using the Bosch process from the same side of the wafer.

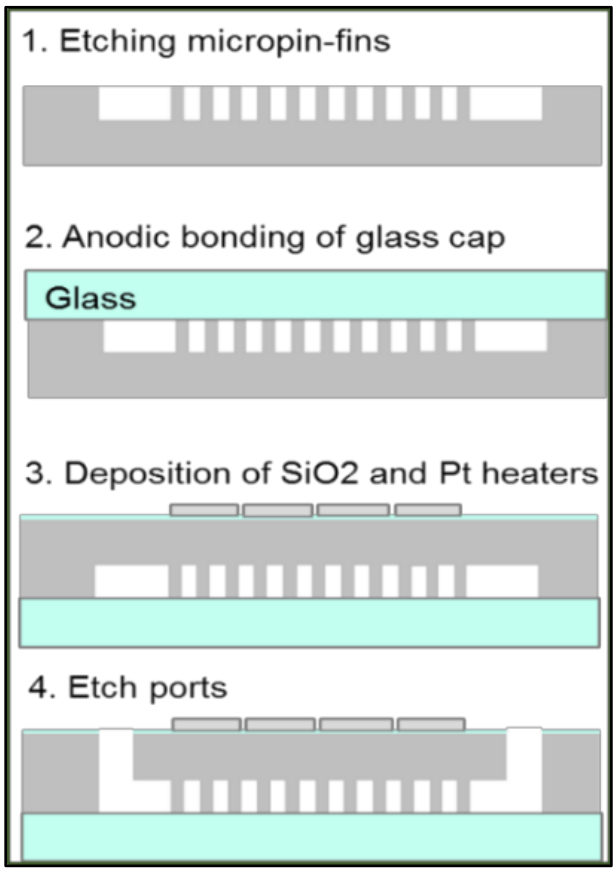

Figure 3.4 Fabrication process

3.3 Uncertainty Analysis

Using the Kline-McClintock method that was described in previous chapter, the uncertainties for the measurements in this set of experiments are presented here in Table 3.1. Thermocouples are calibrated in the range of 19 ^{o}C to 110 ^{o}C using a four-wire precision platinum thermometer connected to a heating and cooling block calibrator (OMEGA CL122). Pressure transducers are calibrated using a pressure calibrator (OMEGA DPI 610).

Table 3.1 Uncertainties

Quantity	Uncertainty
Temperature (^{o}C)	0.03
Pressure (%)	2
Voltage (%)	0.01
Current (%)	0.01
Flow rate (%)	0.04
Heat flux (%)	0.09
Single-phase HTC (%)	11.5
Two-phase HTC (%)	18.6

3.4 Results and Discussions

The following table summarizes the conditions for each test. The maximum mass flux values based on the open cross-sectional area of the microgap are also listed here:

Each of the low, medium, and high mass flux experimental data sets is discussed with the corresponding flow visualization for better understanding of boiling phenomena.

Table 3.2 Experimental conditions

	Test No.	Inlet Temperature	Flow Rate (mL/min)	Max. Mass Flux (kg/m²s)
Dense Device	1	T_{in} = 13 °C	150	7,896
	2		50	2,632
	3		30	1,579
	4	T_{in} = 18 °C	100	5,210
	5		50	2,605
	6		15	781

3.4.1 Test No. 1: T_{in} = 13 °C, Q = 150 mL/min (maximum heat flux reached)

Figure 3.5 shows a set of flow visualizations for a fixed flow rate of 150 mL/min for the entire range of heat fluxes. The flow boiling started around the outlet plenum support pin fins at 199 W/cm^2 (Fig. 6.a). Increasing the heat flux from 199 W/cm^2 to 402 W/cm^2, the flow boiling was observed to enter the microgap and surrounded the pin fins. The boiling region covered a nearly perfect rectangle, indicating spanwise uniformity. This zone grew gradually towards the inlet section of the chip at higher heat fluxes. The calculated mass fluxes for all test conditions are listed in Table 3.2.

In Figure 3.6, the surface temperatures in all four zones are presented. These are estimated from the heater temperature data, by applying one-dimensional thermal resistance corrections. At 230 W/cm^2, the surface 4 temperature slope has slightly decreased, indicating the onset of boiling, confirmed by the visualization in Fig. 7. For the maximum heat flux of 498 W/cm^2, surface 4 was at a temperature of 142 °C, which approached the limits of long term use of bonding materials used, and experiments were

restricted to this maximum value. As heat flux increases, surface 3 and 4 temperatures approach each other. This is as expected, as in flow boiling a more uniform surface temperature is achieved due to the very high heat transfer coefficients.

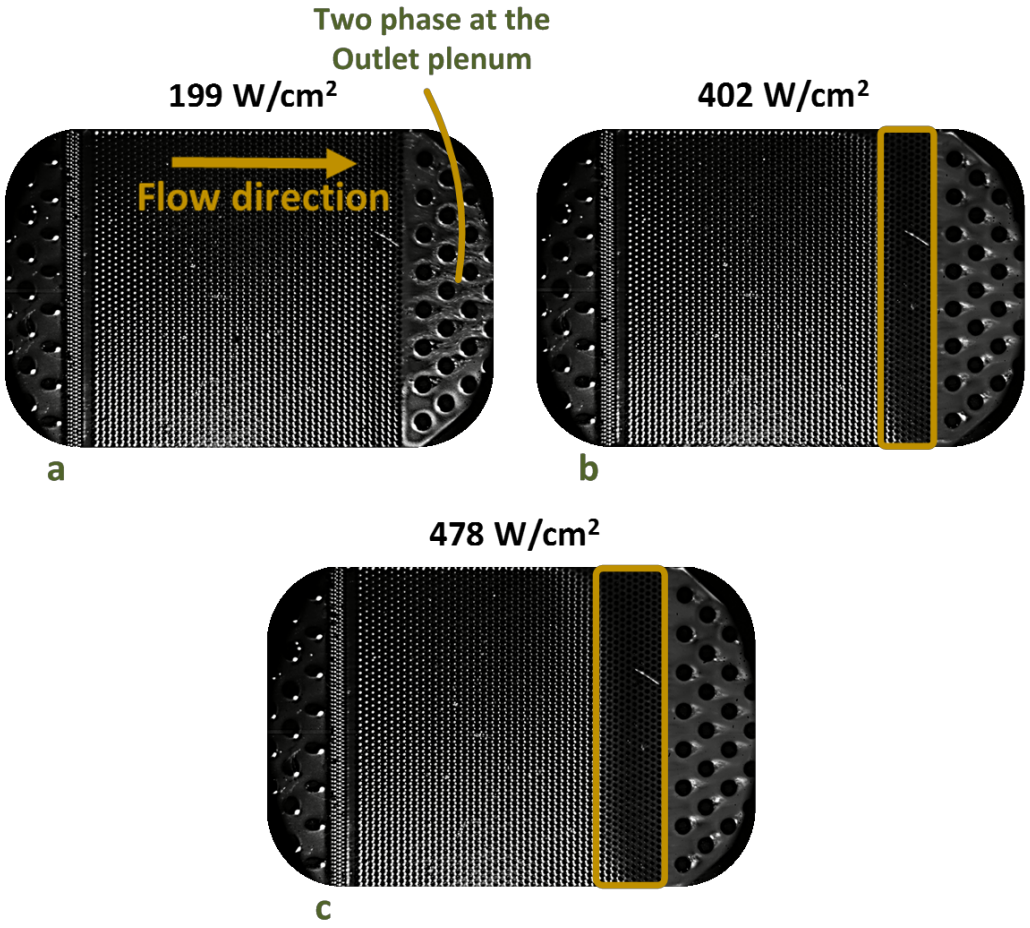

Figure 3.5 Flow Visualizations for Test 1: Flow boiling grows across the microgapat increasing heat flux

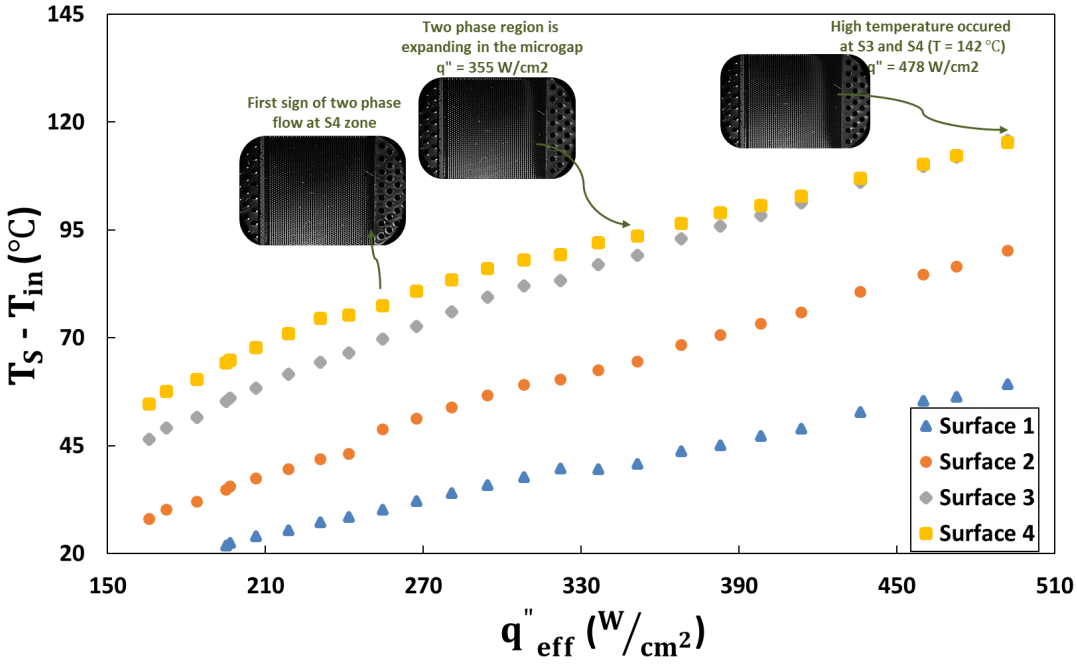

Figure 3.6 Surface temperature distribution (Tin = 13 °C, Q = 150 mL/min) and observed flow regimes

3.4.2 Test No. 2: T_{in} = 13 °C, Q = 50 mL/min (first observation of foggy regime in the microgap)

When the mass flux is reduced by a factor of 3 (G = 2632 kg/m^{2}s), the flow visualizations (Figure 3.7) illustrate a more extensive presence of the two-phase region in the microgap, compared to the previous experiment. More than half of the micropin covered area in the microgap is covered by boiling at heat flux of 258 W/cm^2 (Figure 3.7d) where the experiment is stopped due to high temperature at surface 4 region (128 °C). According to Figure 3.7c, signs of boiling appeared inside the microgap at 247 W/cm^2 in the form of a "foggy" regime. This regime was first observed in the subcooled boiling of water in a 2 mm inner diameter tube for mass fluxes of 10,000 and 25,000 kg.m^{2}s [68]. The vapor inside the test section started to appear around 90 percent of the CHF at 10,000 kg/m^{2}s in a "foggy" shape. The fogs around the pin fins are made of extremely small

bubbles that are gathered together and run along the stream of the fluid flow. Figure 3.8 demonstrates that at a heat flux of 114 W/cm^2, surface 4 temperature falls below the surface 3 temperature due to establishment of flow boiling. This trend persists until the heat flux of 218 W/cm^2. Dry-out condition appeared around the outlet support pin fins at the slightly higher heat flux of 242 W/cm^2. Liquid traces around fins running from left to right in the flow direction are seen in an otherwise vapor region (Figure 3.8).

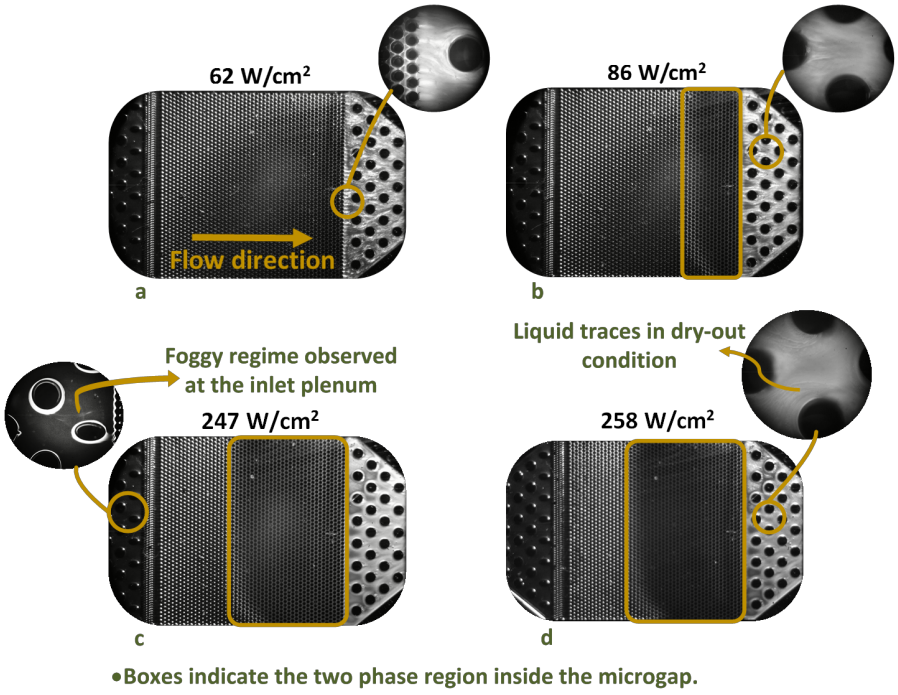

Figure 3.7 Flow Visualizations for Test 2: As heat flux increases, the flow boiling around the exit pin fins becomes more vigorous (close-up visualization sets).

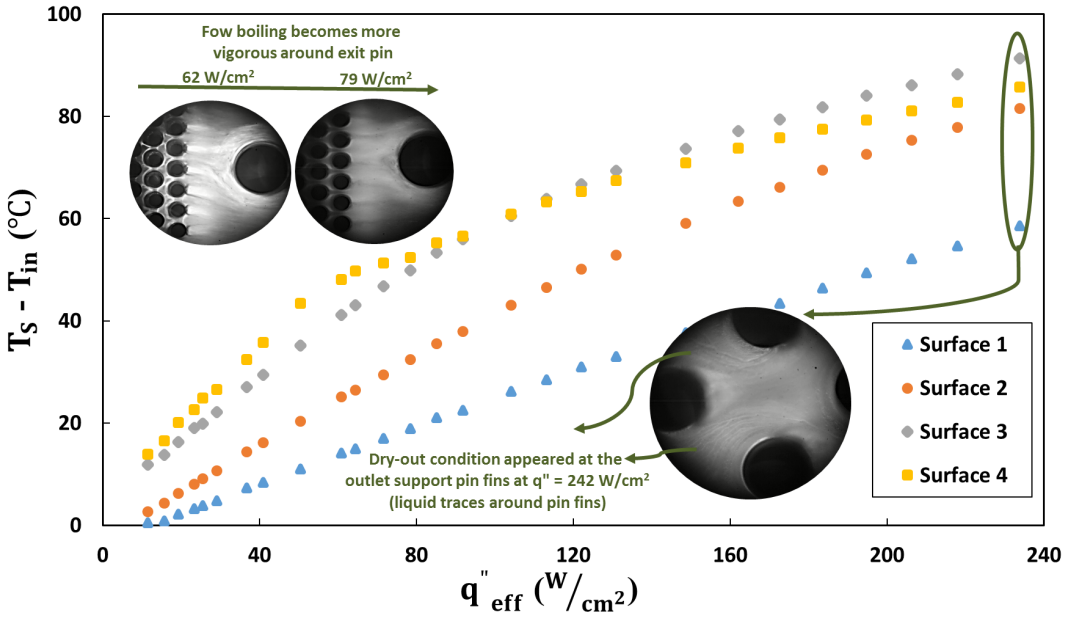

Figure 3.8 Surface temperature distribution (T_{in} = 13 °C, Q = 50 mL/min)

3.4.3 Test No. 3: T_{in} = 13 °C, Q = 30 mL/min (first observation of triangular wakes in the microgap)

For these experiments, the flow rate is further reduced to 30 mL/min, and the inlet temperature is at 13 °C. Triangular two-phase wakes were observed at 33 W/cm^2 as the unique flow boiling pattern for this specific condition (Figure 3.9b). The wakes disappeared by increasing the heat flux to a higher value of 44 W/cm^2. At the highest heat fluxes of 132 W/cm^2, the area of the microgap displaying two-phase transport increased. Chip surface temperature in Figure 3.10, showed a temperature drop at surface 4, due to the local flow boiling. Surfaces 2, 3, and 4 were the only zones that experienced two-phase flow. The temperature responses for these surfaces almost converge at the maximum heat flux. A dry-out condition is clearly recognizable based on the flow visualizations, where the liquid traces move around the exit support pin fins. In this particular test condition, two regions of liquid are observed on the back of the support pin fins that remain firmly attached

to the fins. For this condition, temperature at surface 4 increases sharply, due to the lack of two-phase background flow.

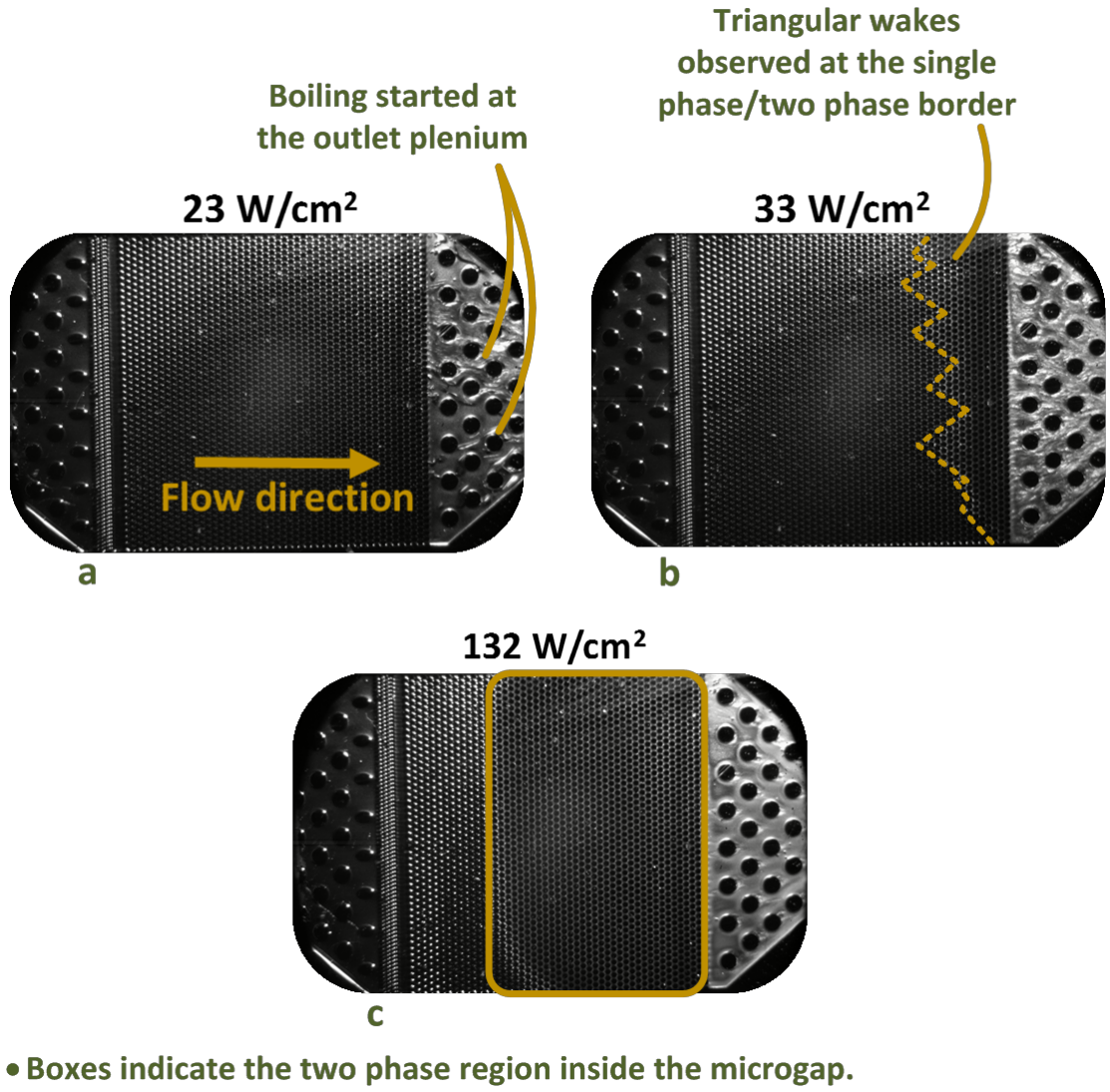

Figure 3.9 Flow visualizations for Test 3: Triangular wakes were observed only at 33 W/cm^2, and disappeared at higher heat fluxes.

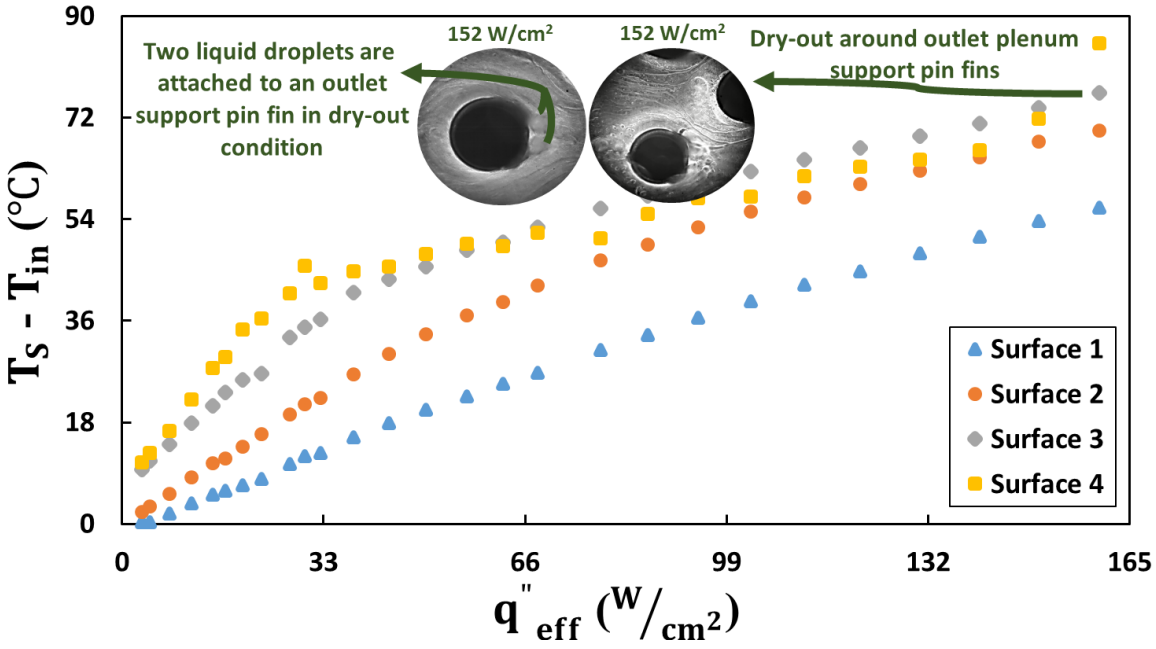

Figure 3.10 Surface temperature distribution (T_{in} = 13 °C, Q = 30 mL/min)

3.4.4 Test No. 4: T_{in} = 18 °C, Q = 100 mL/min (first time observing a clear boundary between single-phase and two-phase region in the microgap)

At a higher fluid inlet temperature, Figure 3.11b and Figure 3.11c show the two-phase flow columns attached to the exit line of microgap pin fins. These columns have different vapor quality compared to the background flow. The columns become more enhanced and merge with the background flow boiling at heat fluxes above 218 W/cm^2. Figure 3.11c illustrates the zones in the microgap where the single-phase area overlaps with the two-phase section. Outlet plenum support pin fins experience more vigorous flow boiling as heat flux increases. The surface temperature data followed the same behavior as the previous test conditions. Surfaces 3 and 4 were nearly at the same temperature of 103 °C at the maximum heat flux of 248 W/cm^2.

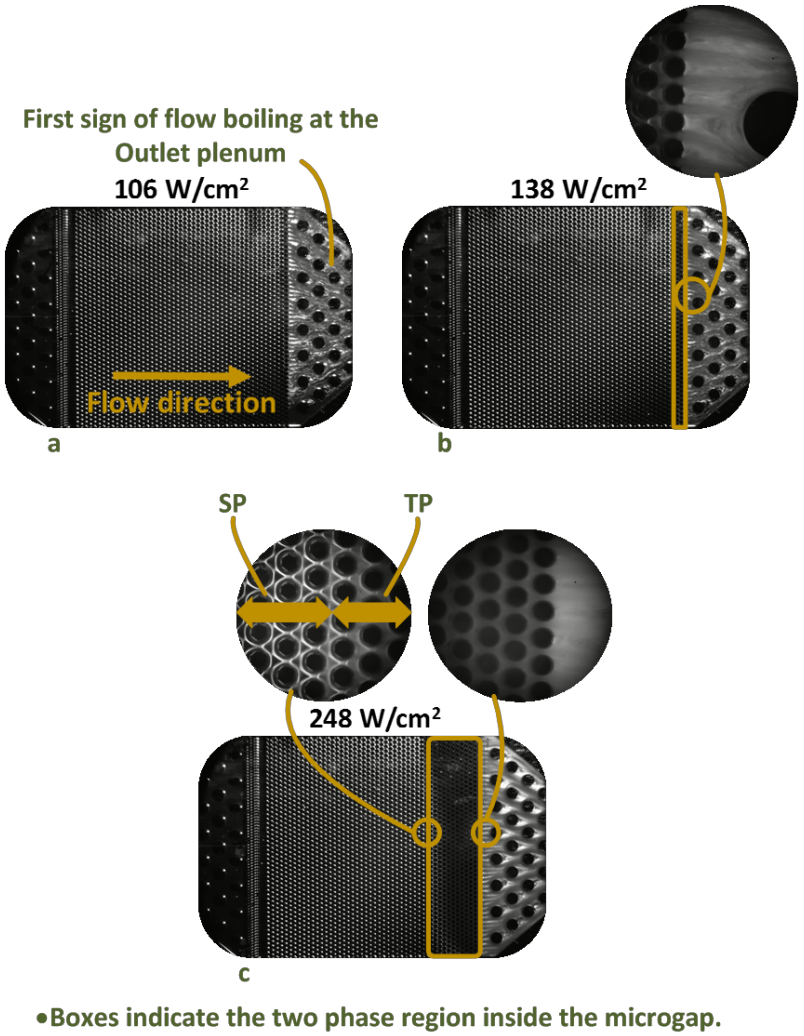

Figure 3.11 Flow visualizations for Test 4: The two-phase region around the microgap pin fins create a darker area compared to the single-phase region.

3.4.5 Test No. 5: T_{in} = 18 °C, Q = 50 mL/min

In this section, the flow rate is reduced to 50 mL/min, but the inlet temperature is kept as 18 °C. As shown in Figure 3.12a, at the heat flux of 39 W/cm^2 the boiling has not entered the microgap, yet distinct two-phase wakes are shed behind the last row of pin fins. Larger rectangle shaped two-phase flow regions are seen at higher heat fluxes (Figure 3.12b). Based on the surface temperature distribution in Figure 3.13, surface 4 experiences flow

boiling above around 70 W/cm^2, accompanied with a temperature drop. At around 110 W/cm^2, this happens for both surface 3 and 4, accompanied with surface temperature reduction, as shown in Figure 3.13.

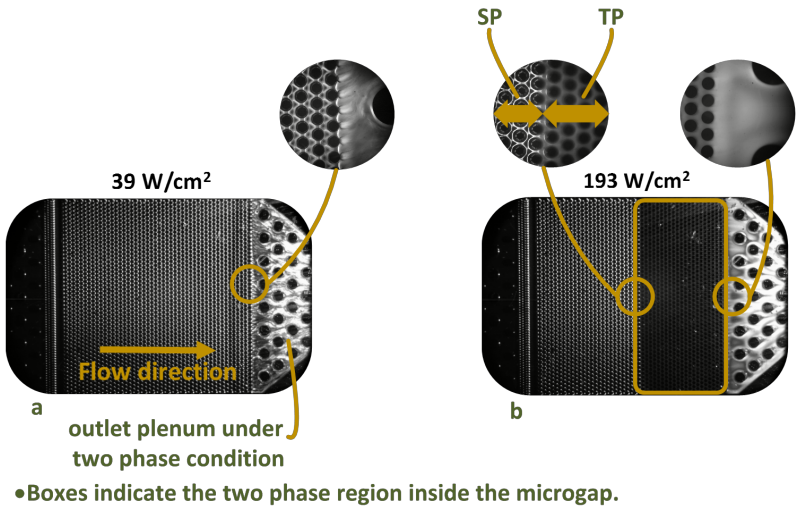

Figure 3.12 Flow visualizations for Test 5: Two-phase region in the microgap is nearly rectangular. Flow boiling around pin fins becomes more aggressive as heat flux increases.

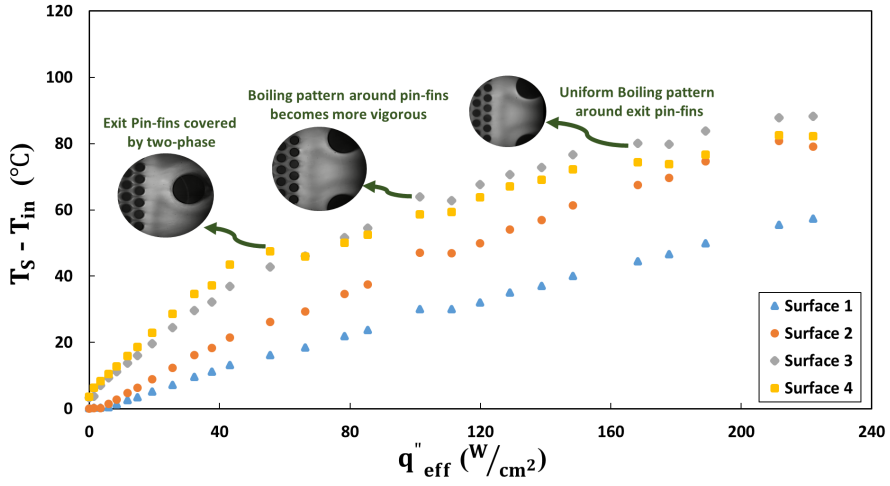

Figure 3.13 Surface temperature distribution (T_{in} = 18 °C, Q = 50 mL/min)

3.4.6 Test No. 6: T_{in} = 18 °C, Q = 15 mL/min (first observation of bubbly regime)

In this last experiment set, the flow rate is set to 15 mL/min and the fluid inlet temperature is 18 °C. Flow boiling started at heat flux of 11 W/cm^2 at the outlet plenum (Figure 3.14a). Due to the low flow rate, by slightly increasing the heat flux, the area inside the microgap under two-phase conditions increased significantly. Figure 3.14b and Figure 3.14c show the two-phase single-phase boundary occupying nearly 75% and 80% of the heated area, respectively. Also, the boiling is more vigorous around the exit pin fins as the heat flux is increased (Figure 3.14b, close-up visualization). First signs of dry-out appeared around the support pin fins at the outlet plenum at heat flux of 76 W/cm^2, depicted in Figure 3.14c. A unique boiling nucleation pattern was observed at the same heat flux around the microgap pin fins at the junction between single phase and two-phase regions. Several bubbles were generated around the pin fins in this region (Figure 3.14c).

The dry-out zone covered the entire outlet plenum at the maximum heat flux 84 W/cm^2 (Figure 3.14d). Figure 3.15 illustrates the surface temperature in all 4 zones for the entire range of heat fluxes. At heat flux of 10 W/cm^2, the flow boiling enters zone 4 and this causes surface 4 temperature to reduce by 5 °C. This happened for surface 3 at heat flux of 14 W/cm^2 when the two-phase region had covered a larger area in the microgap and caused the temperature of this region to drop by 2 °C. Surfaces 2 and 1 each experienced a 1 °C drop in temperature at heat fluxes of 31 W/cm^2 and 33 W/cm^2, respectively. At the maximum heat flux, 84 W/cm^2, heater 4 was at temperature of 101 °C.

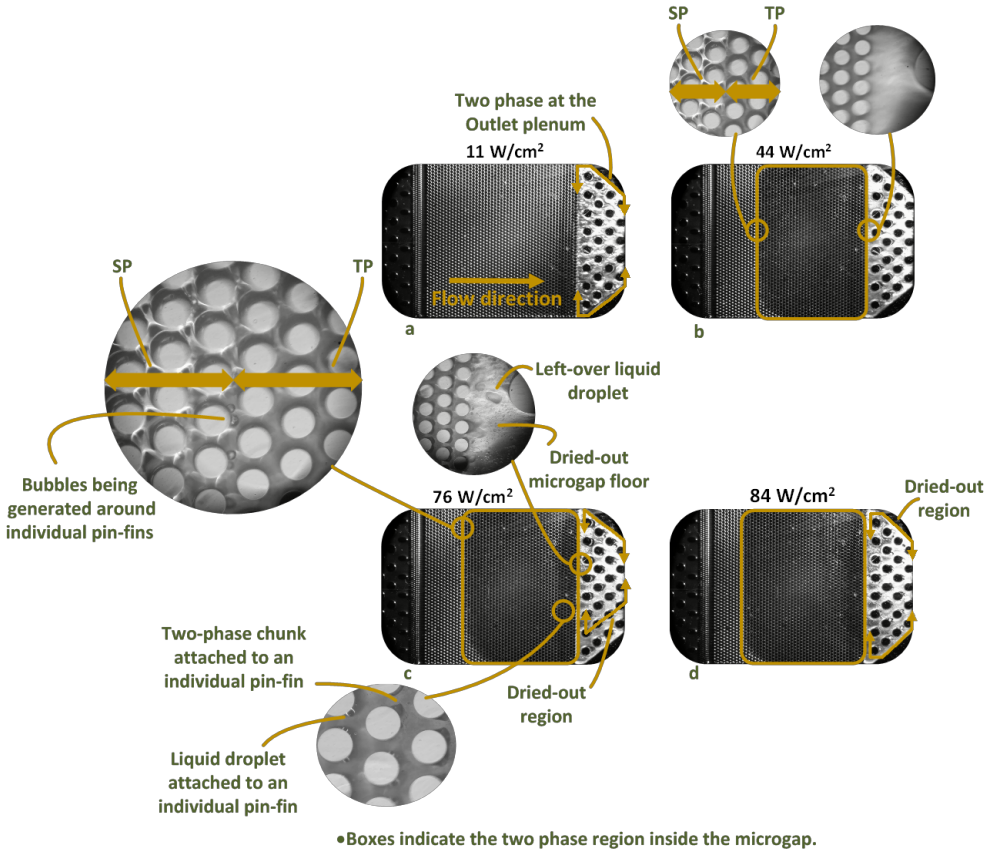

Figure 3.14 Flow visualizations for Test 6: Boiling nucleation was observed at q'' = 76 W/cm² around the pin-fins at the transition spot from single-phase to two-phase flow.

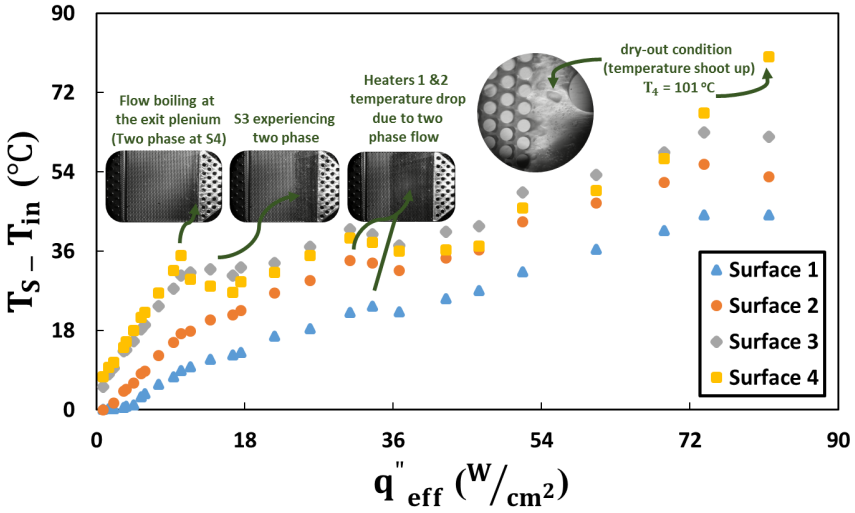

Figure 3.15 Surface temperature distribution (T_{in} = 18 °C, Q = 15 mL/min)

3.5 Single-Phase Heat Transfer Coefficient

The average single-phase heat transfer coefficients are shown in Figure 3.16. As expected, the highest heat transfer coefficients occur at the maximum mass flux of 7,896 kg/m^{2}s. At a given mass flux, the heat transfer coefficients slightly increase with heat flux. This could be due to decrease in the viscosity. The heat transfer coefficient is improved by moving to the two-phase at higher temperature condition, as described in the next section. The single-phase heat transfer coefficient results are compared to [69] at a representative mass flux of 1,036 kg/m^{2}s for R-123 in five 1 cm long, 200 µm wide, and 264 µm deep microchannel array. The comparison shows a good agreement in behavior and the range of the single-phase heat transfer coefficient even though R-123 has slightly different thermophysical properties.

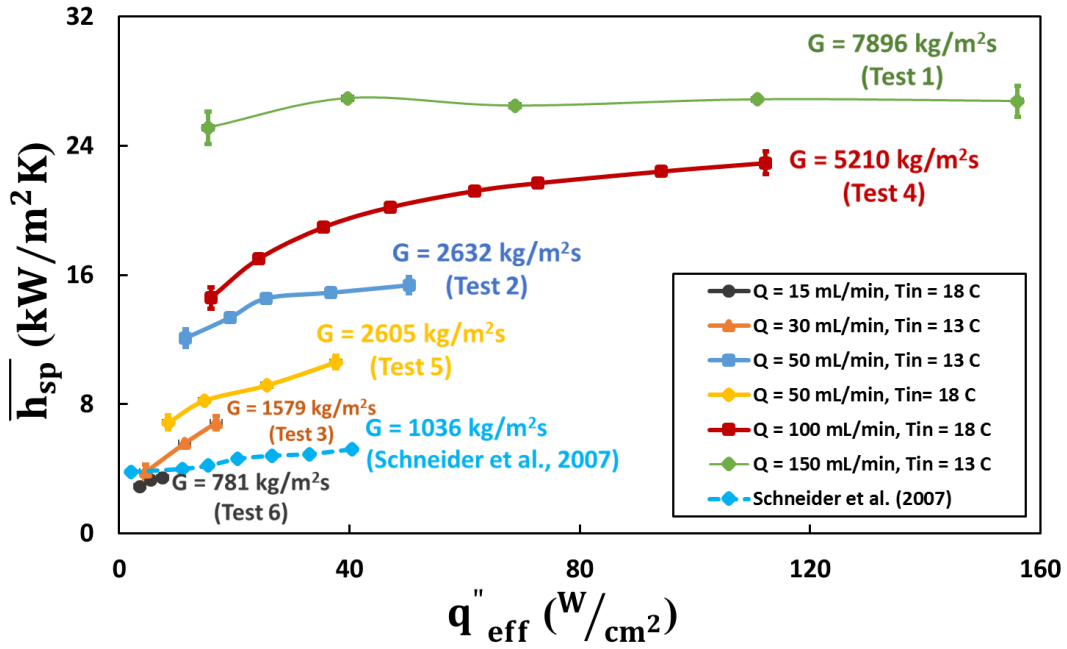

Figure 3.16 Average single-phase heat transfer for all test conditions

3.6 Two-Phase Heat Transfer Coefficient

During boiling, the microgap is divided into two regions, including single phase and two-phase, based on the flow visualizations. The single-phase section is defined as the length of the region between inlet of the microgap, and the first nucleation point around the micro-pin fins. The two-phase length is calculated by subtracting the single-phase length from the entire heated microgap length. A 1-D fin analysis with the adiabatic tip assumption, Equation 13, is used and the average two-phase heat transfer coefficient is computed and shown in Figure 3.17. Test 2 shows the highest thermal performance, since more than half of the microgap foot print area was covered by flow boiling. In Test 1, even though the mass velocity is the highest, the minimum calculated two-phase heat transfer coefficient among all the test conditions is found, since only quarter of the footprint area in the microgap was covered by two-phase flow. Tests 3 and 6 experienced dry-out condition at the maximum heat flux, resulting in drop in thermal performance. The results are compared with the existing literature [69] for R123 at G = 622 kg/m^{2}s, which shows good agreement in trend with the current work.

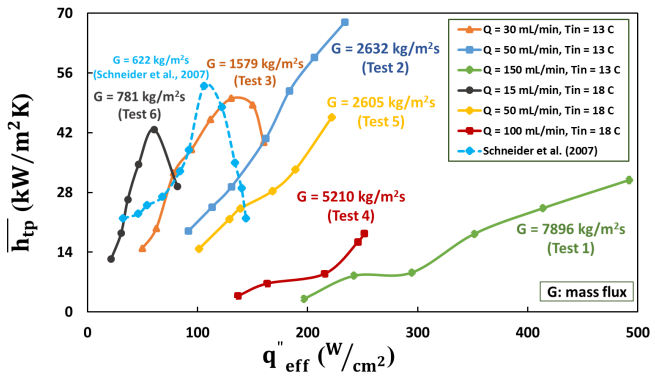

Figure 3.17 Average two-phase heat transfer for all test conditions

3.7 Pressure Drop, Exit Vapor Quality and Single-Phase Length Trend

The pressure drop data between inlet and outlet are presented in Figure 3.18. Each of the plots is divided into two parts: single-phase and two-phase. For the single-phase condition, the pressure drop is lower and independent of heat flux. The pressure drop drastically increases as the flow boiling initiates in the microgap. The maximum pressure drop was about 500 kPa, at the heat flux of 498 W/cm^2, and pertains to Test 1.

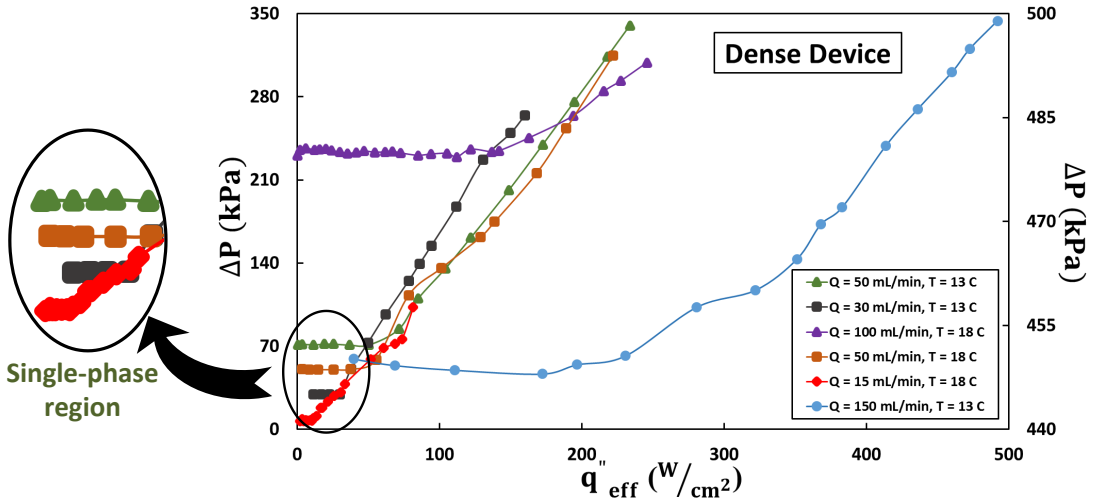

Figure 3.18 Refrigerant pressure drop between inlet and outlet

Figure 3.19 shows the results for the vapor exit quality computed based on the inlet and exit pressure and temperature values. At the inlet temperature of 13 ºC and flow rate of 150 mL/min, the exit vapor quality was nearly zero, as only a small region in the microgap was covered by flow boiling. In contrast, for the inlet temperature of 18 ºC and flow rate of 15 mL/min where the majority of the microgap was covered by two-phase flow. At the flow rate of 50 mL/min, the exit quality did not change much by increasing the inlet temperature from 13 ºC to 18 ºC.

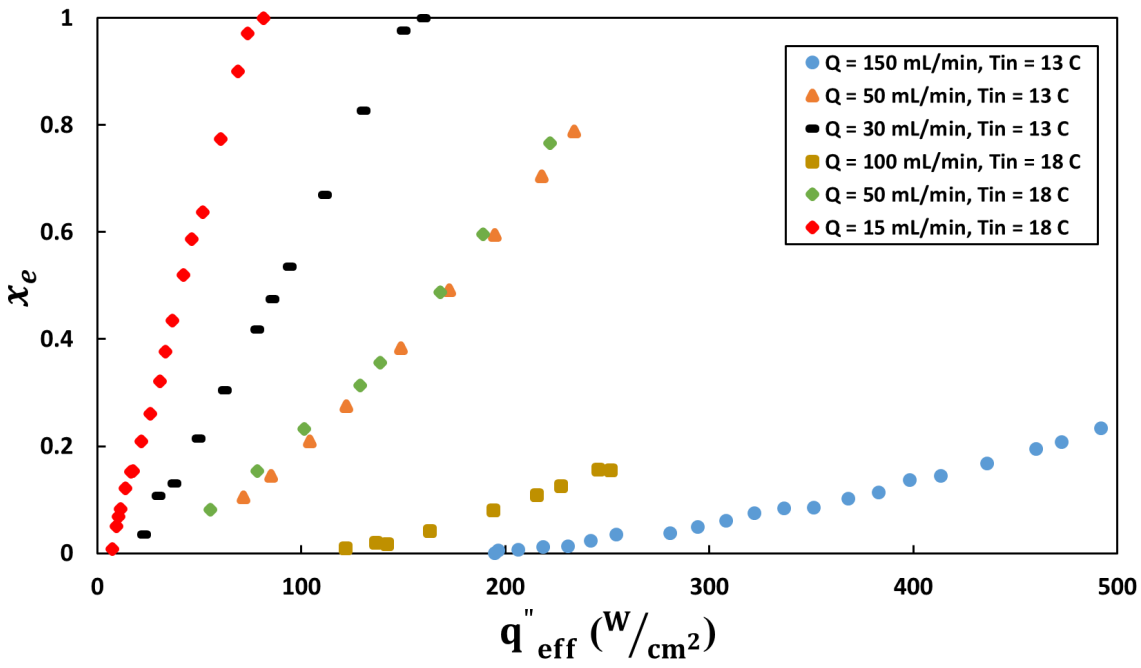

Figure 3.19 Vapor exit quality: Vapor quality reached unity in tests 3 and 6 since the mass flux was the minimum among all test conditions.

Figure **3.20** depicts the trend of single-phase length in the microgap with respect to the effective heat flux for all inlet test conditions. It shows that for lower inlet fluid temperature the single-phase length is longer, compared to an identical test at higher inlet temperature. Also, the data show that the single-phase length decreased at a slower pace in the tests with higher mass flux.

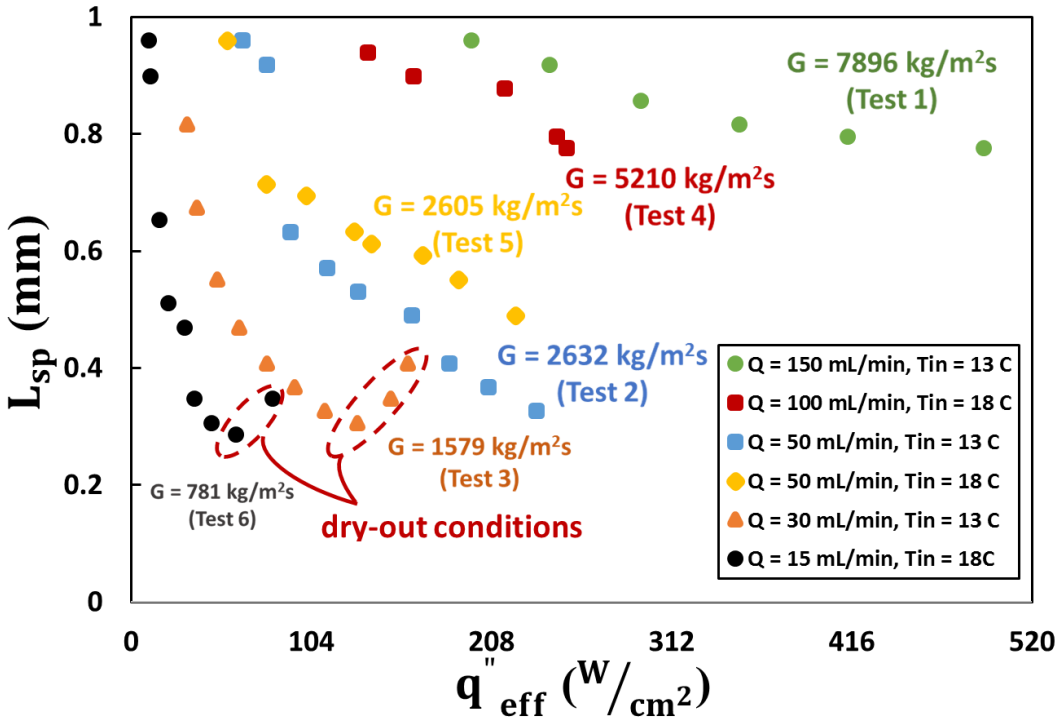

Figure 3.20 The effect of heat flux on the length of single-phase part in the microgap for different test conditions

CHAPTER 4. FLOW BOILING OF R245FA IN A MICROGAP WITH SPARSE CIRCULAR PIN FIN STRUCTURE AND COMPARING IT TO THE DENSE DEVICE

Experimental investigation of the flow boiling of dielectric refrigerant R245fa is conducted in this chapter to study the two-phase flow behavior of this refrigerant in microgaps. Two different silicon microgaps of height 200 μm populated with pin fin arrays of diameter 150 μm with spacing 200 μm (sparse chip) and 400 μm (dense chip) are examined. For 12 different test conditions and in a wide range of heat flux up to 498 W/cm^2 and mass flux up to 7,896 kg/m^{2}s, and inlet temperature in the range of 13 ^{o}C – 18 ^{o}C, average single-phase and two-phase coefficient, flow regime mapping, pressure drop, and exit vapor quality are reported. Three major flow regime patterns are observed in the pin finned area using a high-speed flow visualization at frame rate of 2,229 fps: foggy, bubbly, and slug flow.

4.1 Test Vehicle and Device Configuration

The schematic of the test package is illustrated in Figure 4.1. The package is made of Polyether ether ketone (PEEK) with the melting point of 343 ^{o}C. The device is placed in the pocket at the center of the package (shown in Figure 4.1a), and sealed by four O-rings. Refrigerant compatible Chemraz O-rings (Wyatt Seal Co.) are utilized to seal the I/O, as well as temperature and pressure measurement ports on the back of the chip. Finally, a printed circuit board (PCB) is placed around the chip, which is wirebonded to provide electrical power. The detailed dimensions of the package are shown on Figure 4.1b).

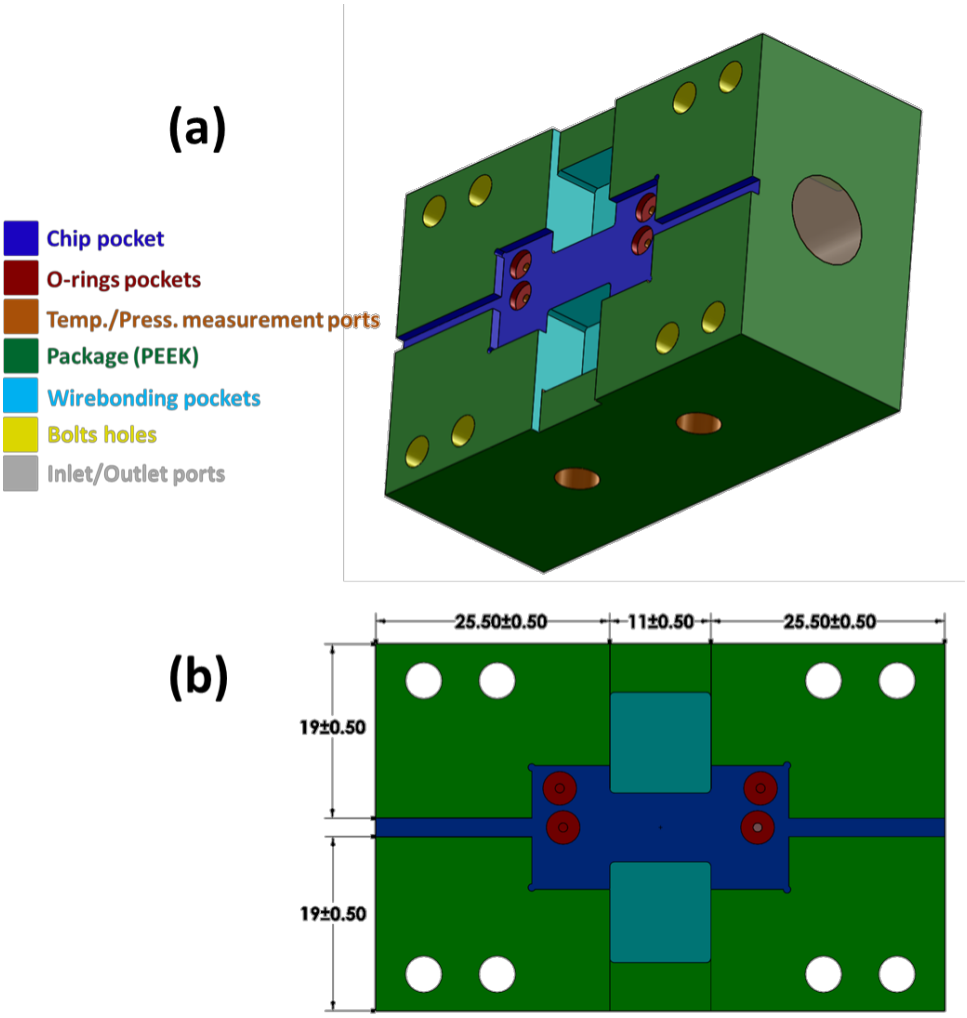

Figure 4.1 Test vehicle package

There are two different silicon-base chips that will be discussed in this chapter: sparse and dense as seen in Figure 4.2. The sparse and dense chips have spacing of 400 µm and 200 µm in both horizontal and vertical directions, respectively.

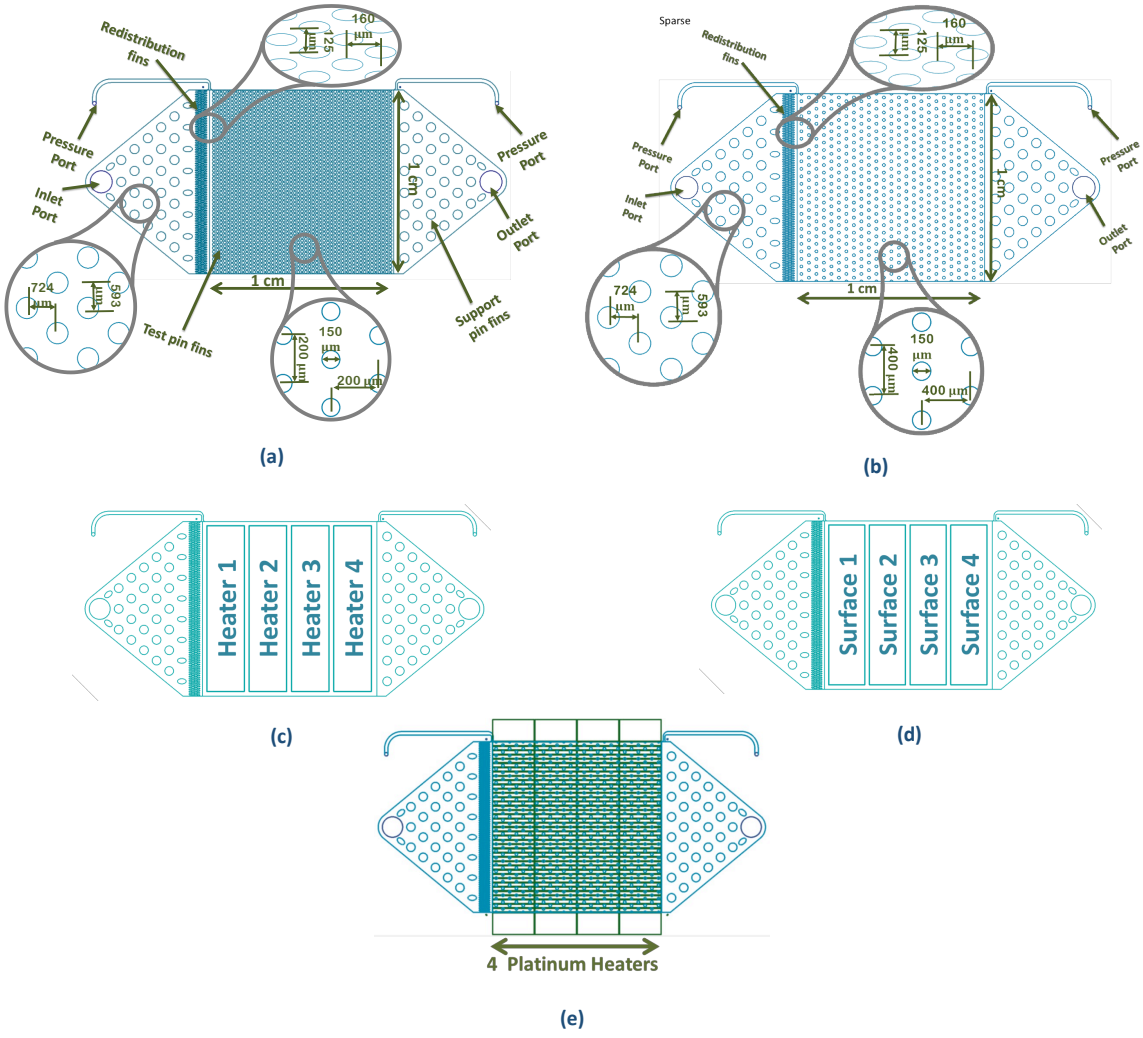

Figure 4.2 Detailed chip configuration: a. front side (dense chip), b. front side (sparse chip), c. heaters configuration, d. surfaces configuration, e. platinum heaters on the back side.

Four serpentine platinum heaters which are deposited on the back of the chip (Figure 4.2e), provide power, and also serve as resistance temperature detector (RTDs). In order to calibrate the heaters, the chip is heated in an oven up to 140 ^{o}C before turning it off. The calibration process is performed based on a quasi-steady-state when the oven is turned off and the chip is cooled off over a few hours. The calibration curves were nearly

linear. The details of the fabrication process of test devices is described in detail in the previous chapter.

4.2 Uncertainty Analysis

The Kline-McClintock method is implemented to find out the uncertainty in the analyzed results, based on determination of the uncertainties of multiple primary measurements [70]. Thermocouples are calibrated in the range of 19 ^{o}C to 110 ^{o}C using a four-wire precision platinum thermometer connected to a heating and cooling block calibrator (OMEGA CL122). Pressure transducers are calibrated using a pressure calibrator that can instantly generate a voltage correspondent to an input pressure (OMEGA DPI 610). The uncertainty in temperature using thermocouples, pressure, voltage, current, flow rate, heat flux, single-phase heat transfer coefficient, and two-phase heat transfer coefficient are 0.03 ^{o}C, 2%, 0.01%, 0.01%, 0.04%, 0.09%, 1%, and 1.2% respectively.

4.3 Data Reduction

A comprehensive data reduction procedure is represented in detail in the previous chapter. The main equations are given here:

$$q^{"}_{eff}A_s = \bar{h}_{sp}(\eta_f N_f P_f H + WL - N_f A_{cf})[\bar{T} - \frac{T_{in} + T_{out}}{2}] \quad \text{(Single-phase HTC)} \qquad (1)$$

$$q^{"}_{eff}A_s = \bar{h}_{tp}(\eta_f N_f P_f H + WL - N_f A_{cf})[\bar{T}_{tp} - T_{sat}] \quad \text{(Two-phase HTC)} \qquad (2)$$

4.4 Results and Discussions

The table below summarizes the conditions for each test. The maximum mass flux values that are calculated based on the open cross-sectional area of the microgap, are also listed here:

Table 4.1 Test conditions

	Test No.	Inlet Temperature	Flow Rate (mL/min)	Max. Mass Flux (kg/m^{2}s)
Dense Device	1	T_{in} = 13 °C	150	7,896
	2		50	2,632
	3		30	1,579
	4	T_{in} = 18 °C	100	5,210
	5		50	2,605
	6		15	781
Sparse Device	1	T_{in} = 13 °C	100	2,105
	2		50	1,052
	3	T_{in} = 18 °C	100	2,084
	4		50	1,042
	5		15	314

The tests for the dense device was presented in the previous chapter. The sparse chip experimental data sets as well as the corresponding flow visualizations are presented here.

4.4.1 Test No. 1: Q = 100 mL/min, T_{in} = 13 °C (Observation of the foggy regime in the entire heat flux range)

In Figure 4.3, the surface temperatures of the last heater (H4) on the back of the device for both sparse and dense devices are presented. These temperature values are the results of the one-dimensional thermal resistance correction (eq. 3). Starting at q" = 30 W/cm^2, in the sparse device, the signs of boiling appeared inside the microgap in the form of "foggy" regime at the top center section in the microgap. This regime was first observed

in the subcooled boiling of water in a 2 mm inner diameter tube for mass fluxes of 10,000 and 25,000 kg.m^{2}s [68]. The vapor inside the test section started to appear around 90 percent of the CHF at 10,000 kg/m^{2}s in a foggy shape. This regime was followed by the bubbly flow regime at heat flux of 174 W/cm^2 which displayed the tiny bubbles at the bottom hot surface of the microgap. The decrease in temperatures of surface 4 at 93 W/cm^2, indicates the onset of boiling. A separate group of bubbles started forming on the back side of the pin fins by increasing the heat flux to 181 W/cm^2, as shown in Figure 4.3. This figure also shows the surface temperature distribution for the dense device as a reference, where the heat flux and temperature data were collected in a wider range which proves better heat transfer performance for the dense chip compared to the sparse chip. It should be noted that the flow rate was set to 150 mL/min for this experiment.

$$R_{total} = \frac{1}{A_s}(t_p/k_p + t_s/k_s) \quad (3)$$

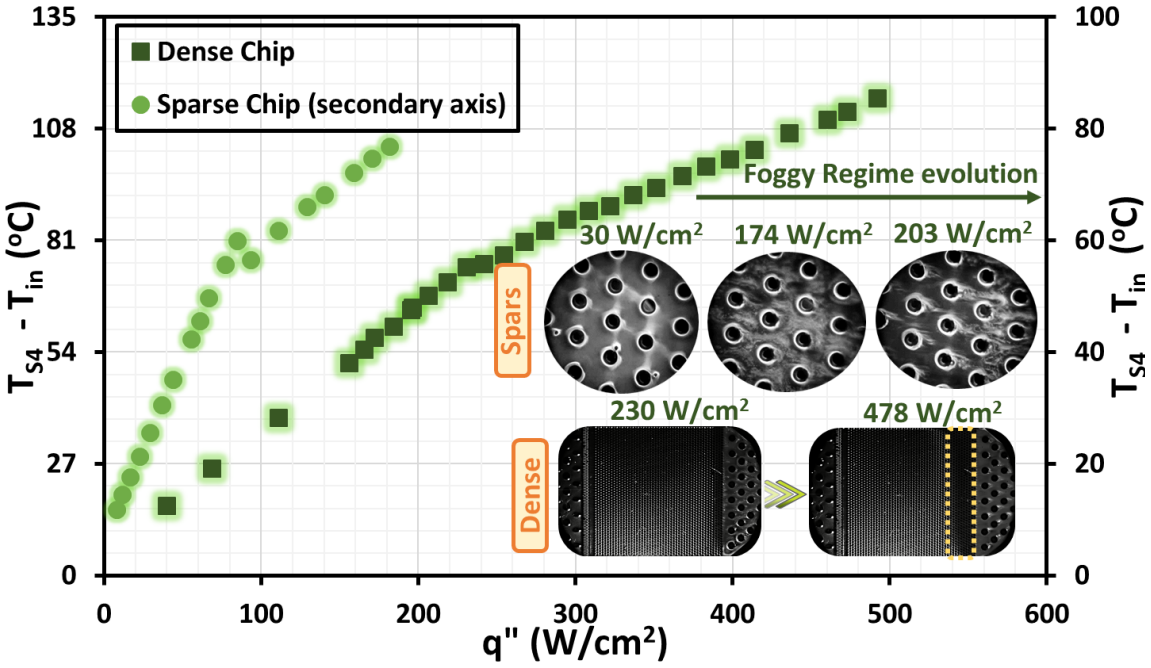

Figure 4.3 Surface temperature distribution (T_{in} = 13 °C, Q = 100 mL/min)

Figure 4.4 shows set of flow visualizations for a fixed flow rate of 100 mL/min for the entire range of heat fluxes. The two-phase flow started around the middle columns of the microgap pin fins at 30 W/cm^2 (Figure 4.4a). Increasing the heat flux to 87 W/cm^2, the bubbly flow and slug flow regimes were also observed around the center and exit of the microgap, respectively. These flow boiling regimes started becoming more vigorous upon increasing the chip power. Upon increasing the heat flux slightly above 203 W/cm^2, the boiling appeared to be in unstable condition.

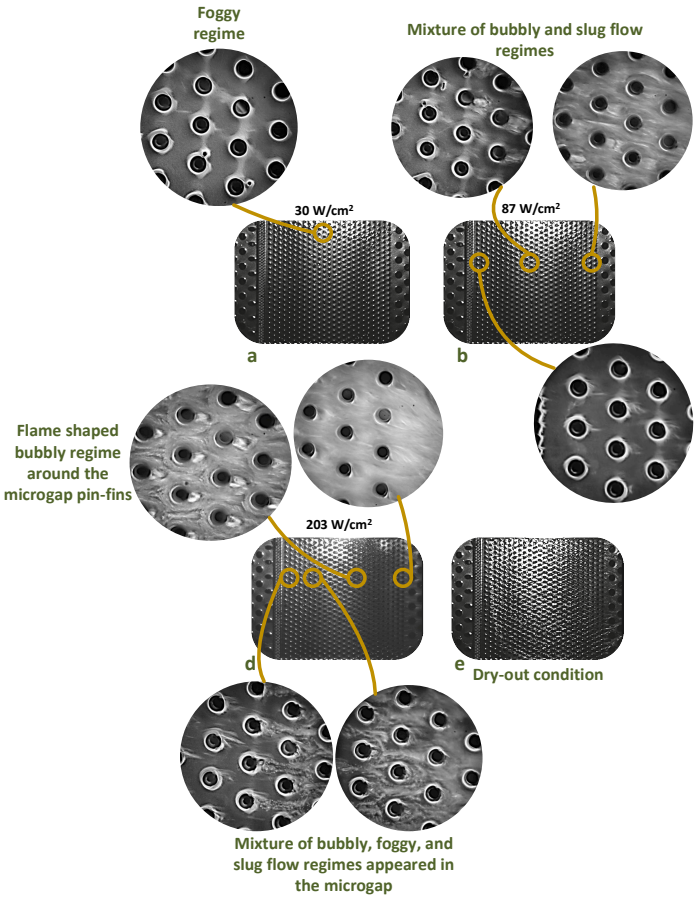

Figure 4.4 Flow visualizations for Test 1: Foggy regime was first observed at q'' = 30 W/cm^2 around the pin-fins in the microgap.

4.4.2 Test No. 2: 50 mL/min, T_{in} = 13 °C (Evolution of flow boiling around individual pin fins)

Reducing the flow rate by a factor of 2 (G = 1052 kg/m^{2}s), decreased the maximum heat flux from 181 W/cm^2 in the previous test to 147 W/cm^2 here (Figure 4.5). The change in the flow regime from foggy to slug flow regimes around individual pin fins for 63 W dissipated power is presented in Figure 4.5. There is again a wider range of the heat flux and temperature data distribution for the dense chip compared to the sparse chip. As shown in Figure 4.5, the liquid traces are appeared in the dense chip microgap at the maximum

heat flux of 242 W/cm^2 due to the high surface temperature which never happened for the sparse chip throughout the experiments. The flow visualization set (Figure 4.6) illustrated that exit pin fins were partially covered by two-phase flow at q" = 76 W/cm^2 which extended to almost the entire microgap upon increasing the heat flux to 150 W/cm^2. At this heat flux, both foggy and bubbly regimes formed around the pin fins.

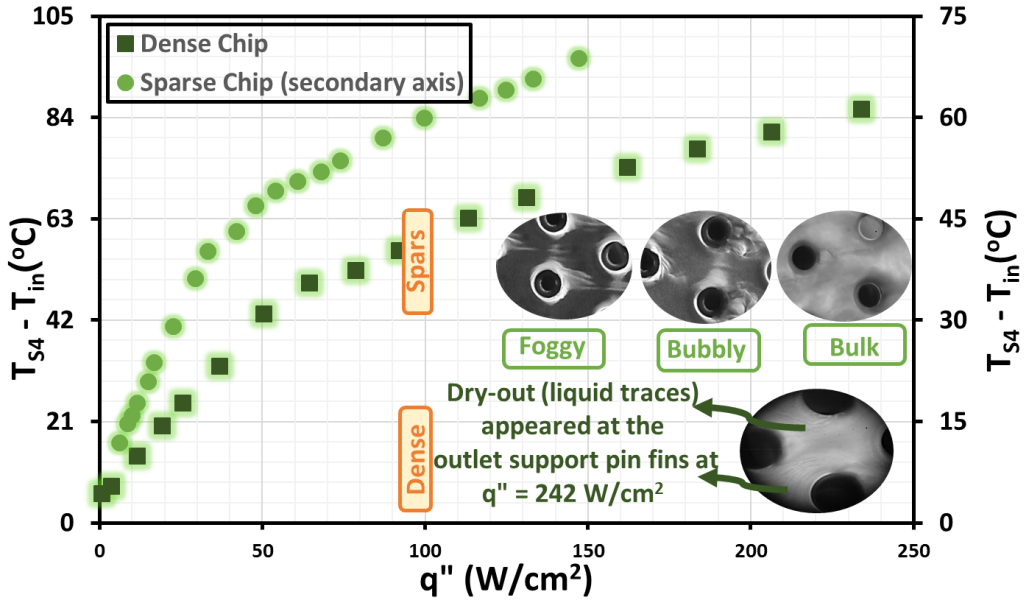

Figure 4.5 Surface temperature distribution (T_{in} = 13 °C, Q = 50 mL/min)

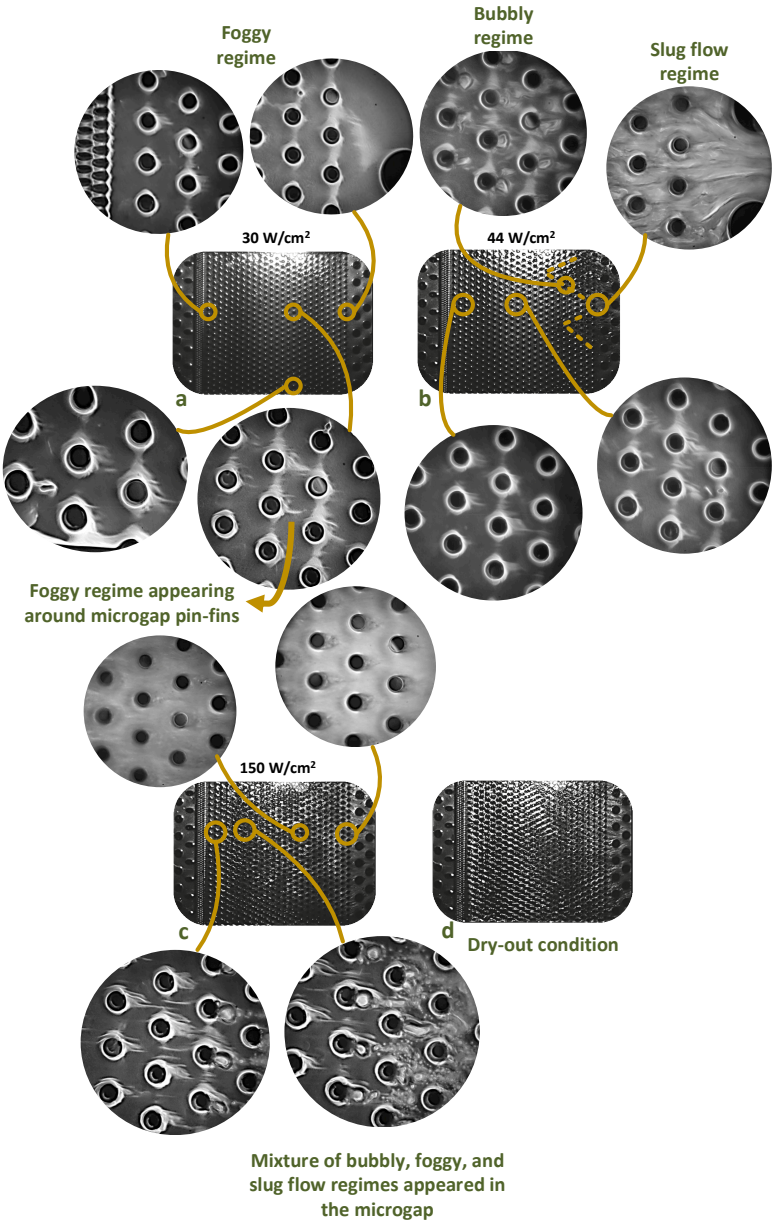

Figure 4.6 Flow visualizations for Test 2: Dry-out condition followed by an unstable flow boiling in the microgap that covered the whole pin finned area.

4.4.3 Test No. 3: Q = 100 mL/min, T_{in} = 18 °C (Observation of the dried-out region on the floor of the microgap)

In this experiment set on sparse device, the flow rate is fixed at 100 mL/min and the liquid flow enters the microgap at 18 °C. When the heat flux reached 79 W/cm^2, two-

phase flow was observed around the last columns of pin fins in the microgap in slug flow regime. The slug regime developed in the microgap by increasing the heat flux to higher value such as 207 W/cm^2. (Figure 4.7). This regime moved to the inlet sections of the microgap at heat fluxes above 200 W/cm^2.

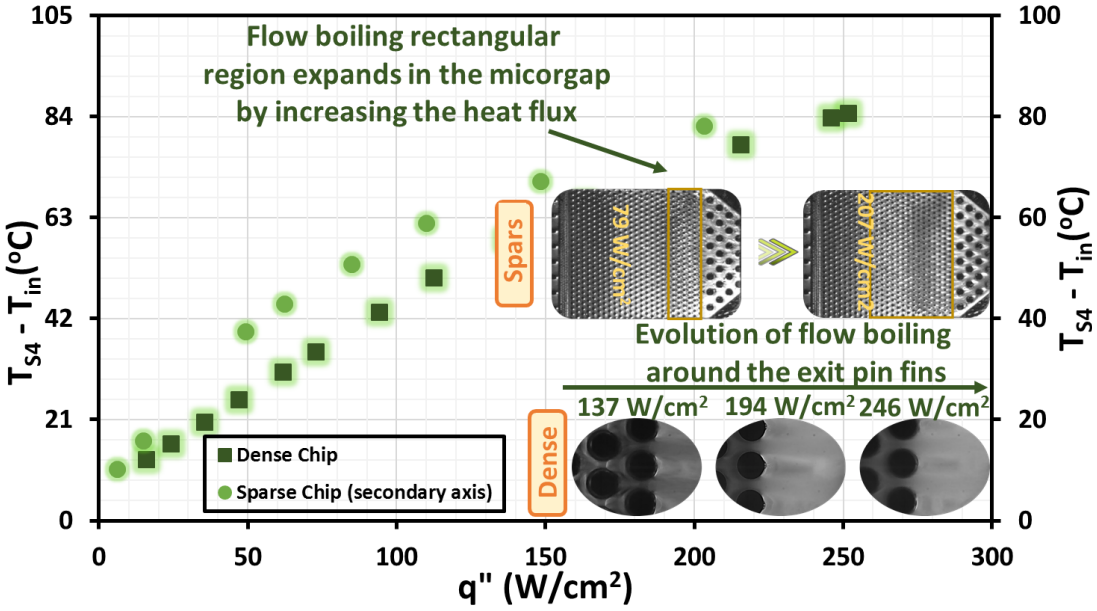

Figure 4.7 Surface temperature distribution (T_{in} = 18 °C, Q = 15 mL/min): Bubbly and Slug flow regime both appeared around the pin fins in the middle section of the microgap at $q^{"}$ = 44 W/cm^2.

4.4.4 Test No. 4: Q = 50 mL/min, T_{in} = 18 °C (Triangular wakes shaped a two-phase region in the microgap)

At a higher inlet temperature (T_{in} = 18 °C), triangular two-phase wakes made a unique flow boiling pattern in the microgap at 49 W/cm^2 (Figure 4.8). This flow shape was not observed for the dense device experiment in an identical initial condition. At heat flux of 130 W/cm^2, the entire microgap was covered by flow boiling and the outlet plenum of the chip started to dry-out. On the contrary, the dense chip microgap did not face dry-out up until 222 W/cm^2 of heat flux.

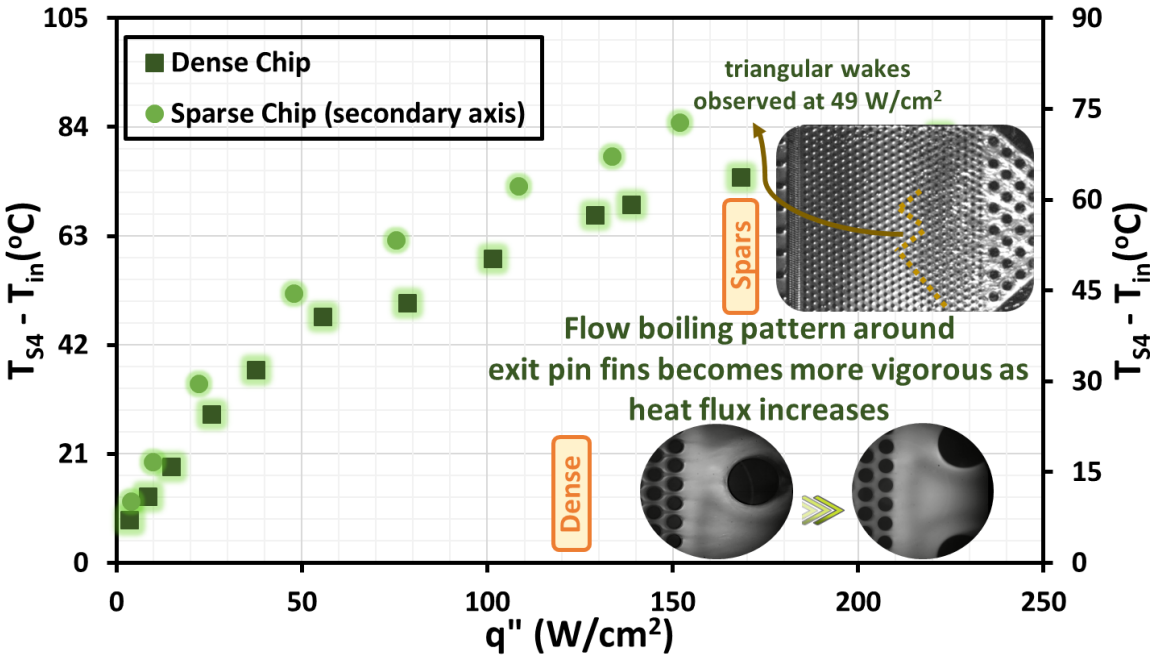

Figure 4.8 Surface temperature distribution (Tin = 18 °C, Q = 50 mL/min): triangular wakes were observed in the microgap at heat flux of 49 W/cm².

4.4.5 Test No. 5: Q = 15 mL/min, T_{in} = 18 °C (Liquid droplets were observed attached to the glass cover at maximum heat flux)

The flow rate is further reduced to 15 mL/min for this set of experiments. Both bubbly and slug flow regimes formed a two-phase flow area around pin fins at the maximum heat flux of 60 W/cm². In this condition, the area in the microgap closer to the exit was under dry-out situation. The exit vapor quality reached 0.83, and only a few liquid droplets survived which were firmly attached to the glass cover due to the surface tension (Figure 4.9). The results show that the sparse device was capable of removing less heat (60 W/cm² vs. 81 W/cm² in the dense device case) due to the less density of the pin fins in the microgap.

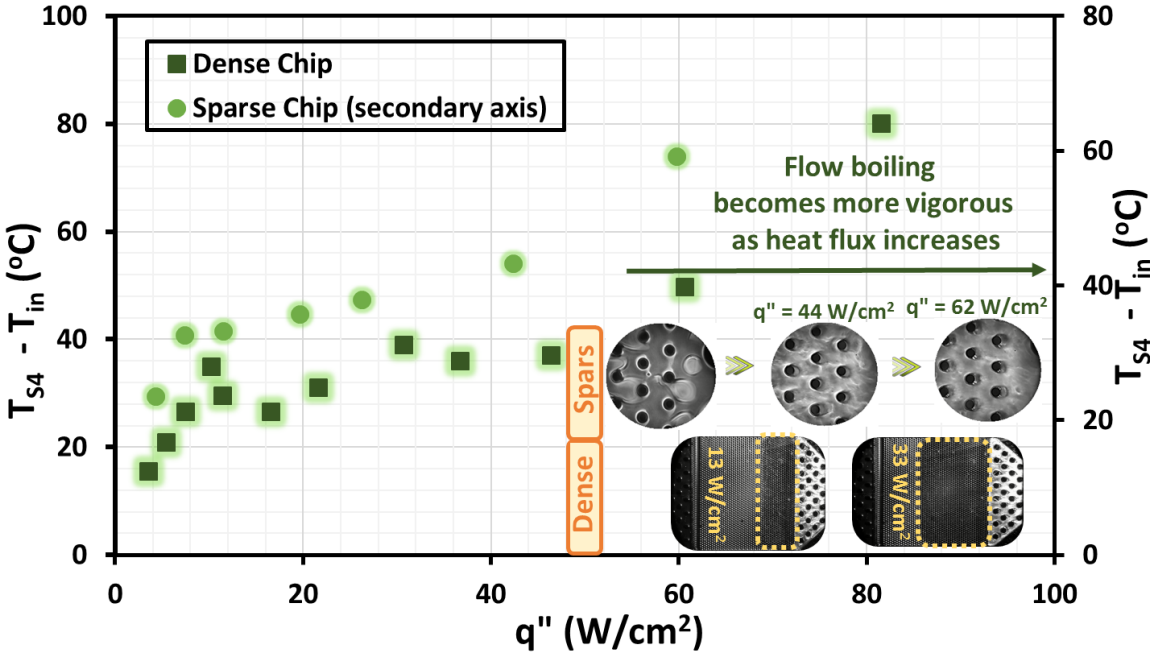

Figure 4.9 Surface temperature distribution (T_{in} = 18 °C, Q = 15 mL/min): At q'' = 44 W/cm², bubbly regime disappeared and was replaced by slug flow.

4.5 Single-Phase Heat Transfer Coefficient

The average single-phase heat transfer coefficients are shown in Figure **4.10**. As expected, the highest heat transfer coefficients occur at the maximum mass flux of 7,896 kg/m²s. At a given mass flux, the heat transfer coefficients slightly increase with heat flux. This could be due to a decrease in the liquid viscosity. The heat transfer coefficient is improved by moving to two-phase conditions at higher temperature condition, as described in the next section. The single-phase heat transfer coefficient results are compared to [68] at representative mass fluxes of 3,000 kg/m²s and 7,000 kg/m²s for HFE7000 in a silicon microgap having a 2.5 mm long, 2.4 mm wide pin finned microgap with 200 μm of depth. The comparison shows a good agreement in behavior and the range of the single-phase

heat transfer coefficient even though HFE7000 has slightly different thermophysical properties.

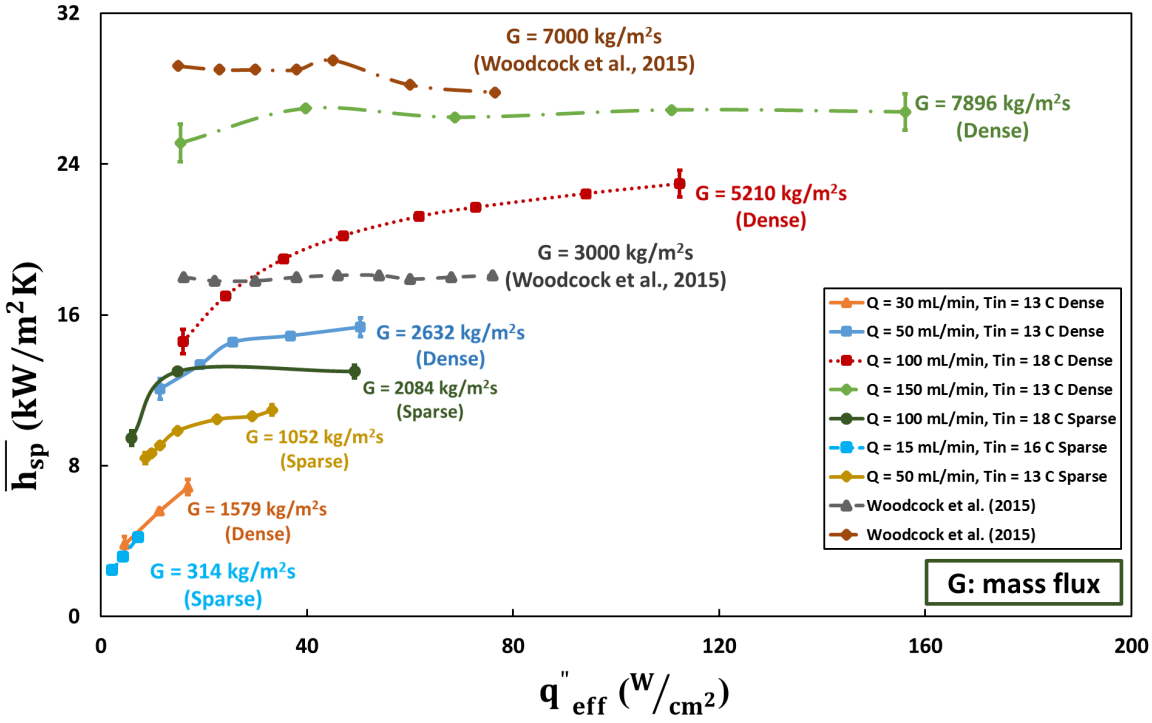

Figure 4.10 Average single-phase heat transfer for representative test conditions and comparison with the existing literature.

4.6 Two-Phase Heat Transfer Coefficient

During boiling, the microgap is divided into single-phase and two-phase regions, based on the flow visualizations. The single-phase part is defined as the length of the region between inlet of the microgap, and the first nucleation point around the micro-pin fins. The two-phase length is calculated by subtracting the single-phase length from the entire heated microgap length. A 1-D fin analysis with the adiabatic tip assumption is used and the average two-phase heat transfer coefficient is computed, and shown in Figure **4.11**. The test on the sparse device at mass flux of 2,084 kg/m^{2}s shows the highest thermal performance, since more than half of the microgap foot print area was covered by flow

boiling. In the test on the dense chip with mass flux of 7,896 kg/m^{2}s, even though the mass velocity is the highest, the minimum calculated two-phase heat transfer coefficient among all the test conditions for this device is found, since only quarter of the footprint area in the microgap was covered by two-phase flow. The dry-out condition which was observed in the dense device test at G = 1579 kg/m^{2}s at the maximum heat flux, resulted in drop in thermal performance.

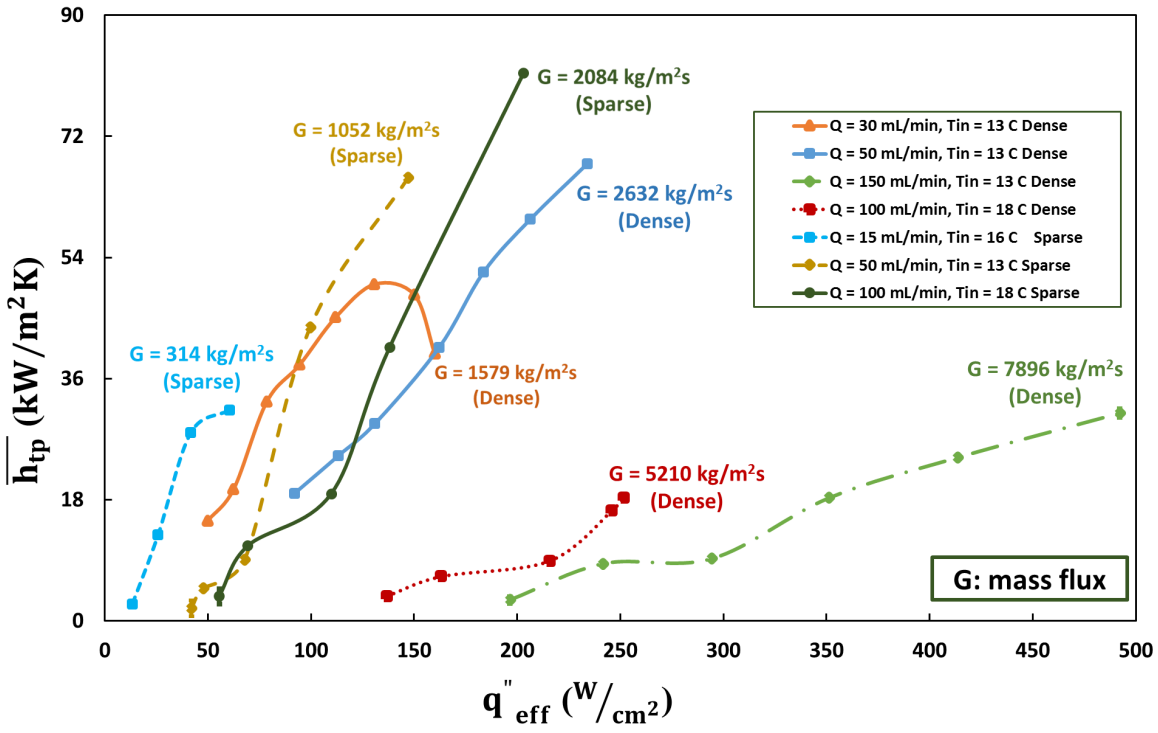

Figure 4.11 Average two-phase heat transfer for representative test conditions and comparison with the existing literature

4.7 Pressure Drop and Vapor Exit Quality

Figure 4.12 depicts the calculated exit vapor quality with respect to heat flux for all tests that are performed on both dense and sparse devices. Among the dense chip results, the exit vapor quality was nearly zero at the inlet temperature of 13 ^{o}C and flow rate of 150

mL/min, as the microgap was only slightly under flow boiling. In contrast, a large area in the microgap was covered by two-phase flow for the inlet temperature of 18 °C and flow rate of 15 mL/min. The exit vapor quality results for the sparse device tests represented that for the tests with the inlet temperature of 15 °C, not much of a change was observed with the identical condition in dense device tests. The experiments with the flow rate of 50 mL/min resulted in a similar behavior in exit vapor quality results.

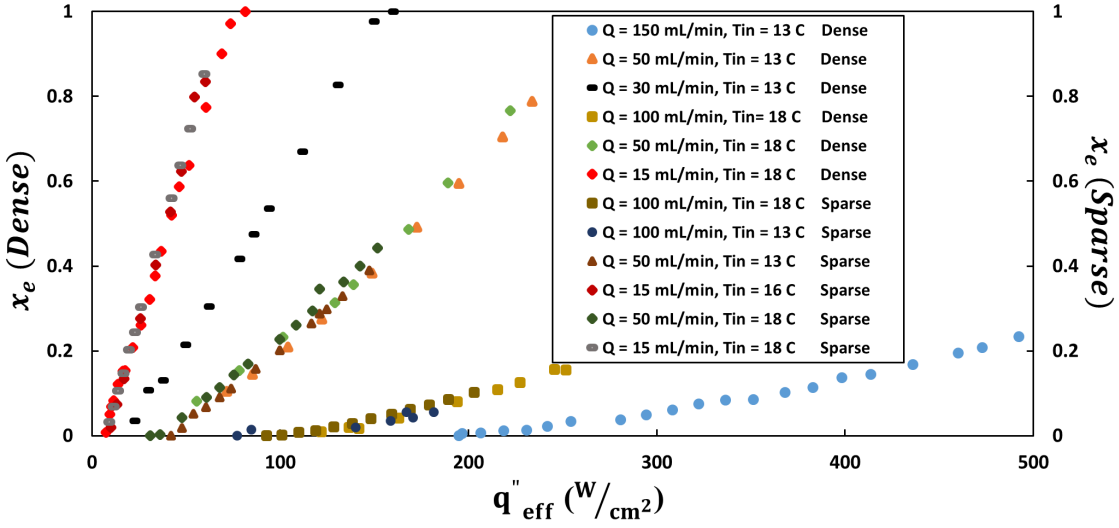

Figure 4.12 Vapor exit quality for all test conditions

The pressure drop across both devices are represented in Figure 4.13. The data for the sparse device are limited to a very small range, compared to the dense device experiments. For the single-phase condition, the pressure drop is independent of heat flux and lower than the two-phase condition. Once the flow boiling occurs in the microgap, the pressure drop drastically increases. The maximum value is calculated to be about 500 kPa, at the heat flux of 498 W/cm^2, and pertains to dense device test 1.

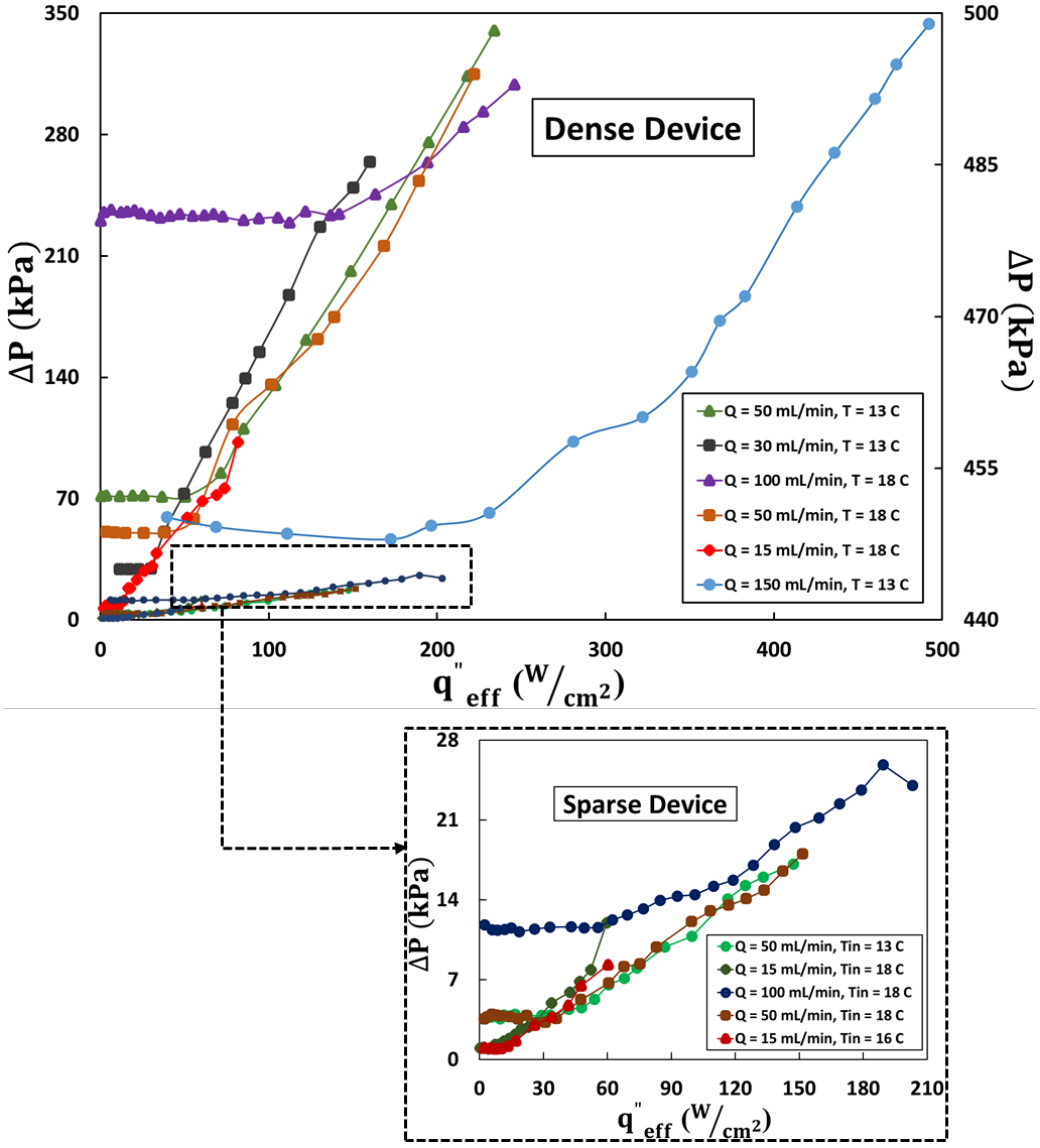

Figure 4.13 Pressure drop across the dense and sparse devices for all test conditions

4.8 Comprehensive Flow Regime Mapping

In this work, a comprehensive flow regime map for microgap flow boiling of R245fa was developed based on the flow visualizations. The experimental investigation of two-phase flow of R245fa in two different microgaps over a wide range of heat flux and mass flux was considered. A database with 160 data points was gained. In order to determine the flow patterns that exist under different operating conditions, the dimensionless boiling

number (eq. 12) and the thermodynamic vapor quality were selected as the representative coordinates for this flow regime map. The data points are distributed within a wide range of vapor quality ranging from – 0.55 to almost 1. Three major regimes of Foggy, Bubbly, and Slug flow regimes are shown in Figure 4.14. The region where bubbly and foggy flow regimes are observed is mostly in the negative section of the horizontal axis. This is due to the fact that the bubbly and foggy flows are observed in the parts in the microgap that are surrounded by single-phase flow. As shown in Figure 4.14, the slug flow regime is found on the positive side of the vapor quality axis, where the microgap was covered by purely two-phase flow. The visualizations illustrate the flow patterns under each of the above-mentioned flow regime condition.

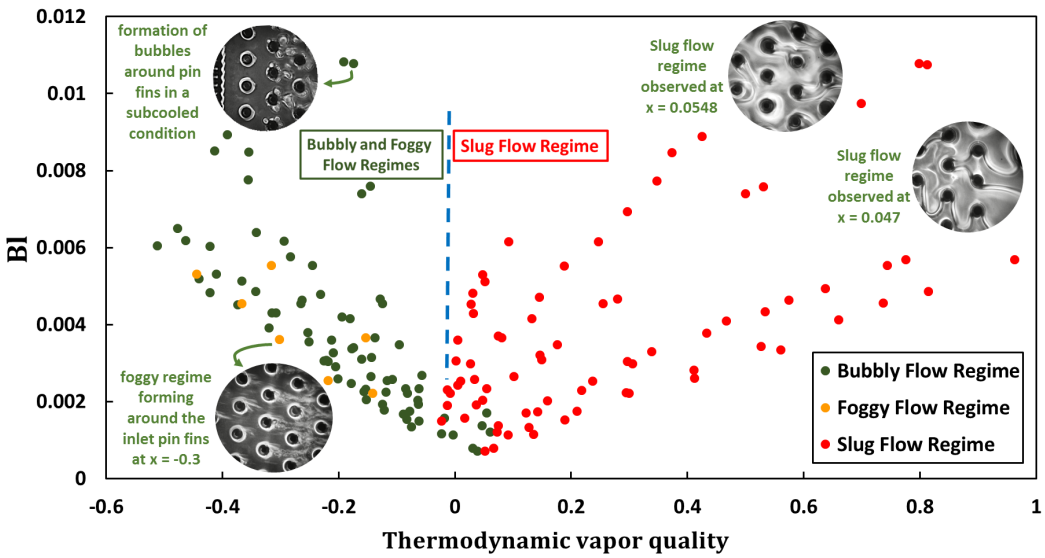

Figure 4.14 Flow regime mapping: The foggy and bubbly regimes were observed in the areas in the microgap mostly covered by single-phase flow where the thermodynamic vapor quality was calculated as negative.

CHAPTER 5. FLOW BOILING OF R245FA IN A MICROGAP WITH HYDROFOIL AND CYLINDRICAL STAGGERED PIN FINS AND FLIPPED INLET/OUTLET

In this chapter, an experimental study of two phase flow of R245fa refrigerant in two different microgaps for a range of heat fluxes between 7 W/cm^2 to 326 W/cm^2. The gaps have a surface area of 1cm x 1cm with the height of 200 μm. In one device, an array of hydrofoil (densely packed) and the other cylindrical (sparsely packed) shaped pin fins covers from bottom to top of the microchannels. The pin fins with hydrofoil shape have diameter, longitudinal pitch, and transversal pitch of 75μm, 450μm and 225μm, respectively. The cylindrical pin fin pins have longitudinal pitch, and pin-fin diameter of 225 μm, 225 μm, and 75 μm, respectively. On the back side of each chip, four platinum heaters are fabricated in series to enable two-phase flow in the gap. The microgap is installed in a pumped flow loop. The results demonstrate the heaters and surface temperature data versus heat flux dissipated through the microchannel. Also, the flow visualization using a high-speed camera is provided for the power ranging from 7 W/cm^2 to 326 W/cm^2. The amount of heat loss across the test section is also provided. At the end, single-phase and two-phase heat transfer coefficient as well as pressure drop correlations are developed that match the data from current experimental study [71] as well as a previous study done by the current author.

5.1 Test Vehicle and Chips Configuration

Figure 5.1 shows the schematic of the experimental setup. The air inside the loop is fully evacuated using a vacuum pump (VN-200N, JB Industries Inc.). In order to charge the system with R245fa, the source tank is heated up to a temperature higher than ambient temperature. After charging the reservoir with enough refrigerant, the reservoir is heated up to few ^{o}C higher than ambient temperature in order to make sure that the pressure inside the reservoir is enough to have the flow always going towards the syringes. The continuous flow is insured by having one of the pumps pushing, and the other one pulling instantly. Once the pumps are fully charged, the refrigerant is pushed by one of the syringe pumps towards the pre-cooler in order to become all in liquid phase. After leaving the pre-cooler, the working fluid volumetric flow rate is measured by a microturbine flow meter (S-114, Mcmillan Co.). R245fa then becomes contaminant free by passing through a 0.5 μm filter (SS-4F-05, Swagelok Co.). The 0.5 μm in-line filter prevents contaminants from entering the device. The flow loop is equipped with a back-wash circuit to be able to run the fluid through the chip in both directions for the purpose of cleaning it before running the actual test. The fluid comes back to the reservoir after cooling down in the heat exchanger that is located right after the test section. The refrigerant is pushed through the test device at a certain flow rate and becomes hot. It then enters the heat exchanger (LL510G14, Lytron Co.) to become cool enough before coming back to the reservoir.

The system is run for a few hours and all properties such as pressures, temperatures, and flow rate are recorded by the data acquisition unit to guarantee steady state before running the thermal test. The systems properties (temperature and pressure) need to stay at a certain constant value in each cycle of pushing in order to guarantee the steady state

condition of running the experiment. Once steady state is reached, the heaters are powered gradually starting from heat flux of ~1 W/cm^2. The voltage and current applied to the heaters are recorded for heat flux calculations.

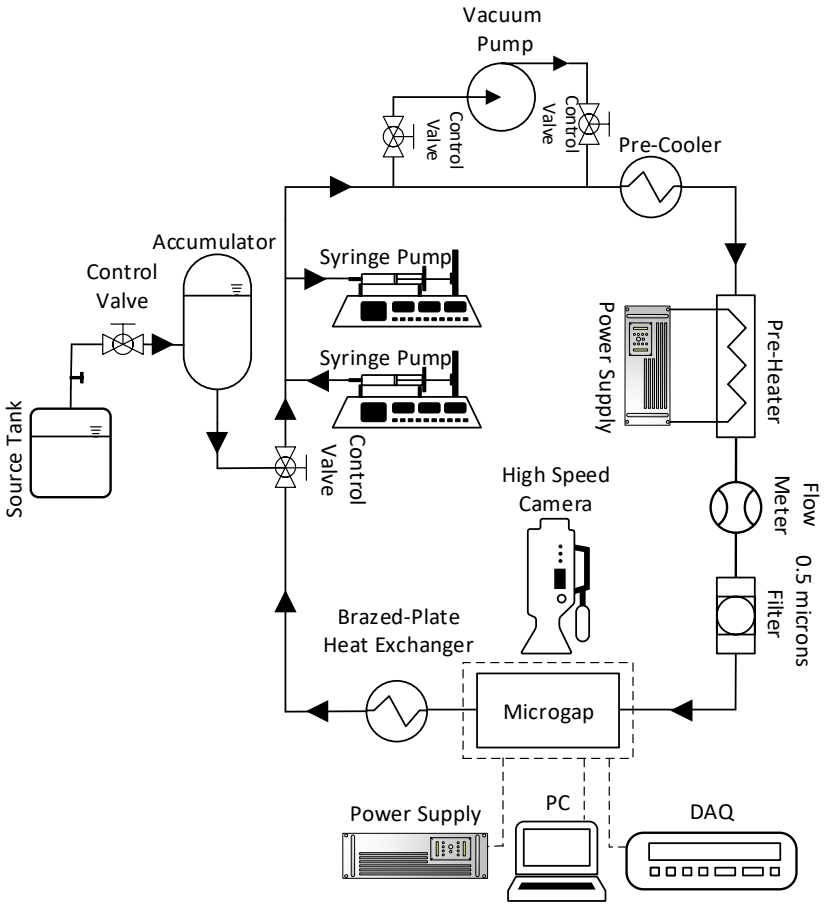

Figure 5.1 Flow loop schematic

The flow boiling inside the microgap is visualized by a high-speed camera (Phantom V211, VISION Research Co.), at 2,229 frames per second. All measured data for temperature, pressure, voltage and the current are recorded for each heat flux value. Figure 5.2 illustrates the schematic of the test devices. The fabrication process is described in detail in the next section. The chips are sealed between a printed circuit board (PCB) and a package made of peek material with melting temperature of 313 ^{o}C. O-rings are used to

seal the ports on the device. Using wirebonding process, the electrical connection from the chip to the PCB is done. Two T-type 1.56 mm diameter thermocouples are utilized to obtain temperature data at the inlet and outlet of the devices. The pressures at the inlet and outlet are also recorded using two pressure transducers connected to the pressure measurement ports fabricated on the chip (shown in Figure 5.2). Staggered hydrofoil and cylindrical pin fins are arranged inside the 1cm^2 microgap. The pin fins are NACA 66-021 hydrofoils that were also investigated previously by Kosar et al. [56]. The arrays of flow redistribution pin fins upstream of the hydrofoil pin fins are to evenly distribute the flow towards the microgap pin fin arrays.

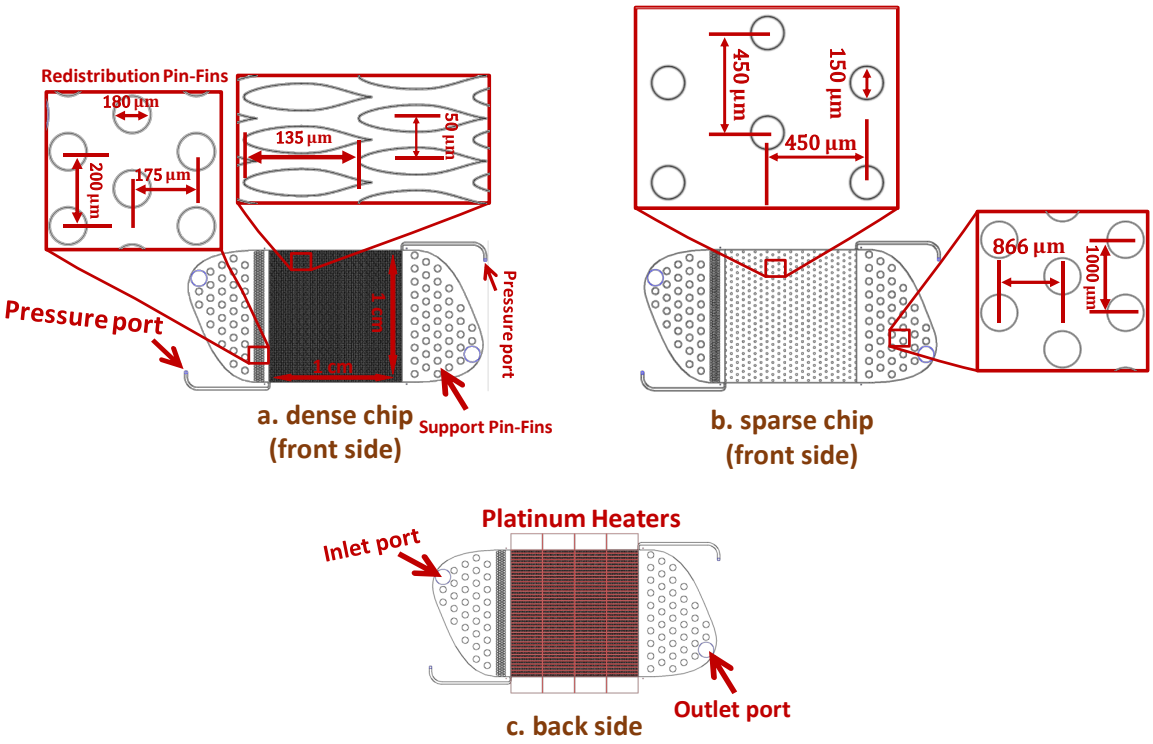

Figure 5.2 Detailed chips configuration: a. front side (dense chip), b. front side (sparse chip), c. platinum heaters configuration

Four serpentine platinum heaters which are deposited on the back of the chip (Figure 5.2c), provide power, and also serve as resistance temperature detector (RTDs). In order to calibrate the heaters, the chip is heated in an oven up to 140 ^{o}C before turning it off. The calibration process is performed based on a quasi-steady-state when the oven is turned off and the chip is cooled off over a few hours. The calibration curves were nearly linear. The details of the fabrication process of test devices is described in detail in chapter 3.

5.2 Uncertainty Analysis

The Kline-McClintock method is implemented to find out the uncertainty in the analyzed results, based on determination of the uncertainties of multiple primary measurements [70]. Calibration for thermocouples is done in the range of 19 ^{o}C to 110 ^{o}C using a four-wire precision platinum thermometer connected to a heating and cooling block calibrator (OMEGA CL122). Also, pressure transducers are calibrated using a pressure calibrator that can instantly generate a voltage correspondent to an input pressure (OMEGA DPI 610). The uncertainty in temperature using thermocouples, pressure, voltage, current, flow rate, heat flux, single-phase heat transfer coefficient, and two-phase heat transfer coefficient are 0.03 ^{o}C, 2%, 0.02%, 0.02%, 0.04%, 0.11%, 1.5%, and 1.6% respectively.

5.3 Data Reduction

A detailed data reduction related to single-phase and two-phase heat transfer coefficients as well as sinlge-phase and two-phase surface temperatures is represented in detail in chapters 2 and 4 about.

5.4 Results and Discussions

The conditions for the tests that are done on both sparse and dense devices are summarized in the table below. The maximum values for mass flux are obtained based on the open cross-sectional area in the microgap that are reported here:

Table 5.1 Test conditions

	Test No.	Inlet Temperature	Heat Flux (W/cm^2)	Flow Rate (mL/min)	Max. Mass Flux (kg/m^2s)
Dense Device	1	T_{in} = 10 °C	150	120	1,586
	2		213	120	1,586
	3		293	120	1,586
	4	T_{in} = 10 °C	41	30	394
	5		79	30	394
	6		102	30	394
Sparse Device	7	T_{in} = 25 °C	8	15	193
	8		25	15	193
	9		34	15	193

5.4.1 Test No. 1-3: T_{in} = 10 °C, Q = 120 mL/min (maximum heat flux reached)

In this set of experiments, the dense device is tested and the flow rate is fixed at 120 mL/min and inlet temperature is set to 10 °C. The two-phase flow in the microgap first appeared as a bulk boiling zone that covered part of the microgap in a triangular shape. The reason for this is the configuration of the inlet and outlet ports that are in opposite side of the longitudinal axis of the chip. By increasing heat flux to higher values, this region expands in the microgap and eventually part of it becomes completely dried out. A set of

flow visualizations as well as a schematic of the flow boiling evolution inside the microgap is depicted in Figure 5.3 and Figure 5.4, respectively.

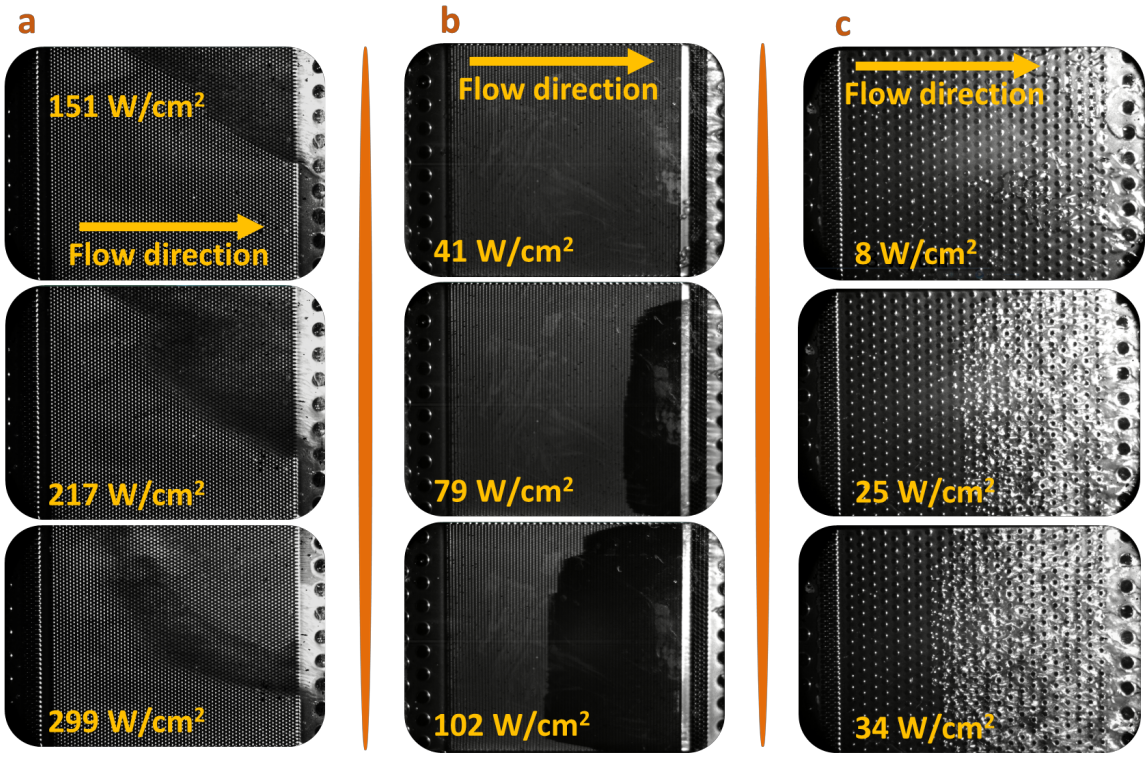

Figure 5.3 High-speed flow visualization set for: a) Tests 1-3 b) Tests 4-6 c) Tests 7-9

Figure 5.4 illustrates the schematic interpretations of the visualization set presented in Figure 5.3. As shown in the pictures, for the first few heat flux values the majority of the chip is covered by liquid phase (blue solid region). However, as the power was raised, the two phase region expands more through the microgap. For heat fluxes between 264-326 W/cm^2 a third region is developed close to the outlet of the chip, which is mostly covered by vapor (solid gray region). This region caused the surface temperature to increase significantly.

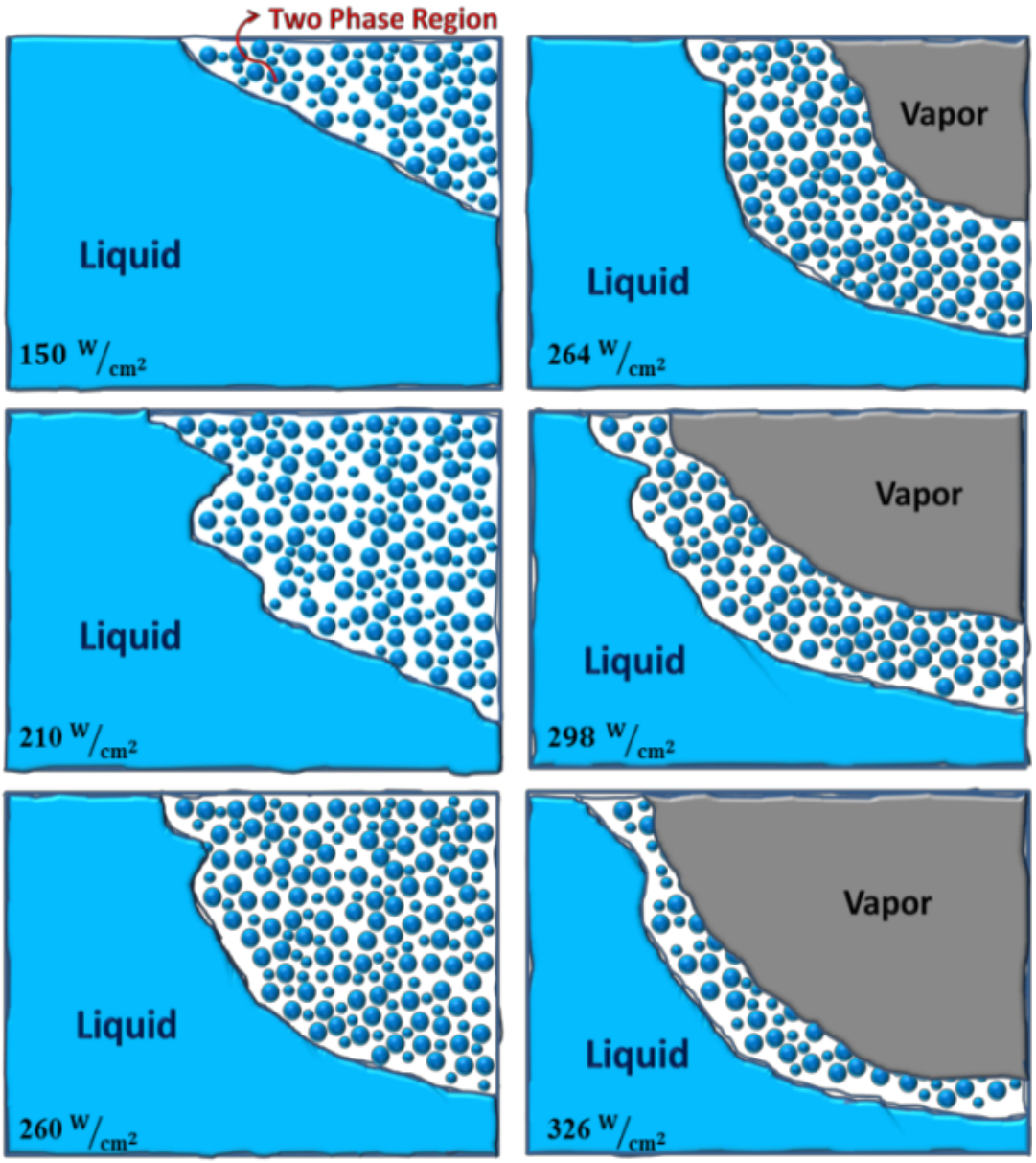

Figure 5.4 Drawing of tow-phase flow versus heat flux

Figure 5.5 shows the surface temperature distribution for the surfaces 3 and 4 as well as the exit vapor quality of refrigerant versus effective heat flux. At heat flux of around 60 W/cm^2, the microgap started being under dry-out condition. This caused the surface temperature to drastically increase until complete dry-out of the microgap at the heat flux

of 326 W/cm^2. The flow visualization set in Figure 5.3a shows how the vapor zone expands in the microgap until the complete dry-out condition.

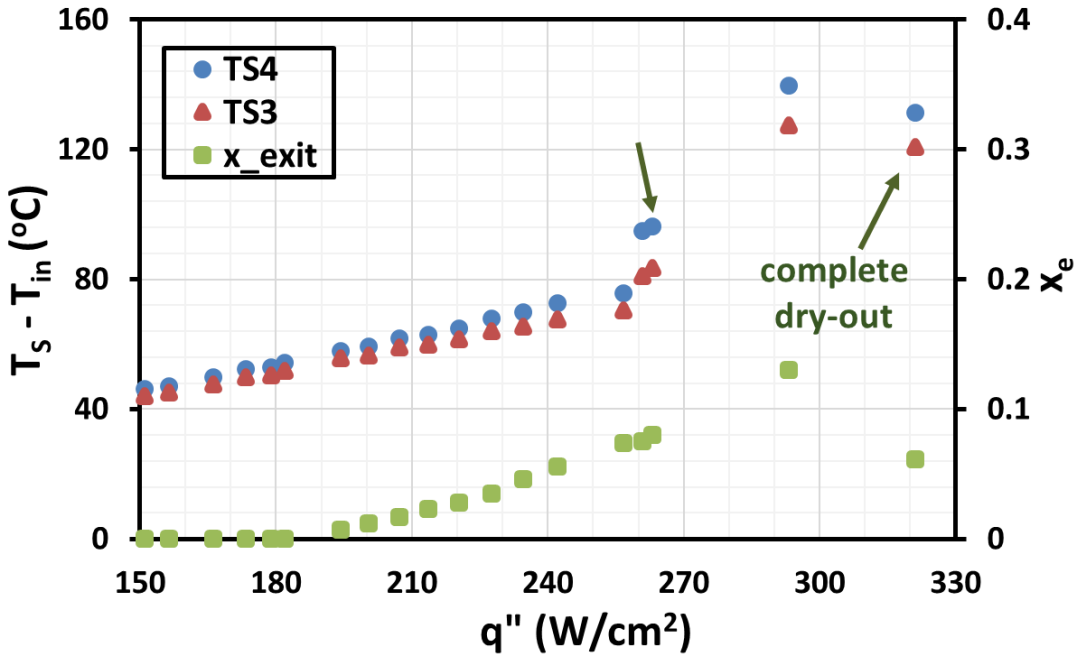

Figure 5.5 Surface temperature distribution for surfaces 3 and 4 as well as exit vapor quality distribution versus effective heat flux, tests 1-3.

5.4.2 Test No. 4-6: T_{in} = 10 °C, Q = 30 mL/min

In this set of experiemtns, the dense chip is flipped with respect to y-axis in order to avoid large pressure drop at the inlet of the microgap. The inlet temperature is still set to 10 °C and the flow rate is reduced to 30 mL/min. As shown in Figure 5.3b, the first signs of boiling appeared in the form of bubbles attached to the last row of pin fins in the microgap. Two-phase region enlarged in the form of rectangular region by increasing heat flux to higher values. The evolution of the flow boiling can clearly be observed in Figure 5.6. Also, surfaces 3 and 4 are almost under same temperature at maximum heat flux value of 102 W/cm^2 (Figure 5.6).

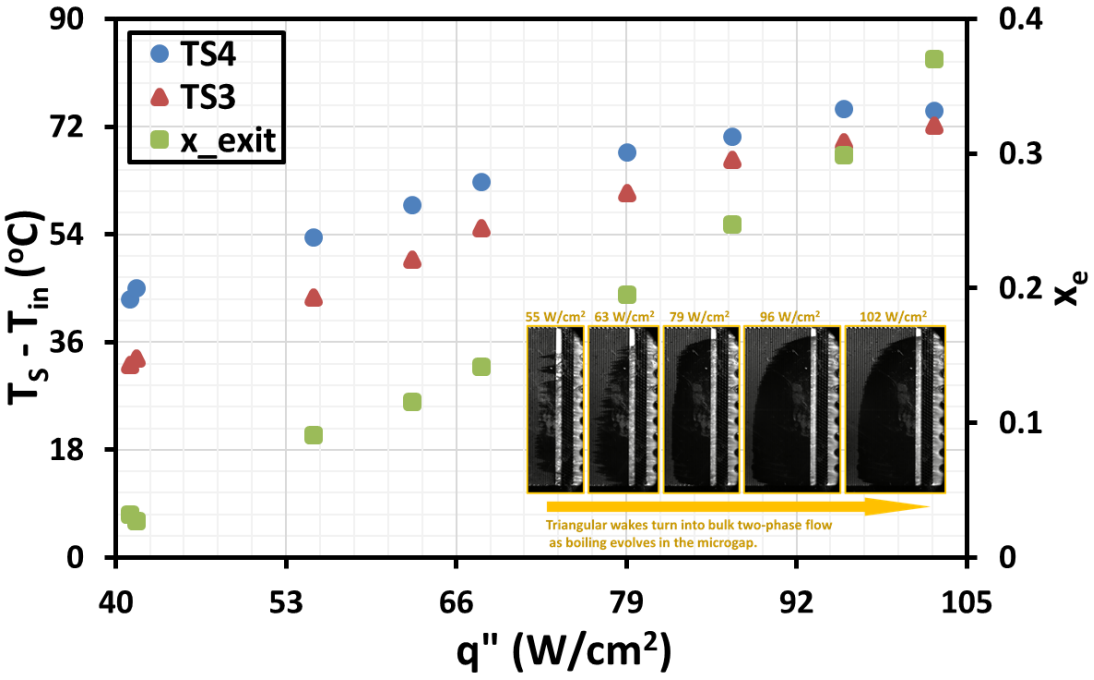

Figure 5.6 Surface temperature distribution for surfaces 3 and 4 as well as exit vapor quality distribution versus effective heat flux, tests 4-6.

5.4.3 Test No. 7-9: T_{in} = 25 °C, Q = 15 mL/min (Triangular wakes appeared)

In Tests 7-9, the sparse device is tested at a reduced of 15 mL/min and a fixed inlet temperature of 25 °C. Flow boiling appeared in the microgap first in a triangular wakes shape and then was replaced by a bulk two-phase flow in the microgap (Figure 5.3c). However, bubbly flow regime was still the incipient of the boiling in the microgap (very first row of pin fins covered by two-phase flow). Surfaces 3 and 4 were almost under same temperature condition throughout the entire test. This is because the boiling expanded quickly in the microgap from the beginning. Due to the low flow rate value, it was not possible to increase the heat flux above 32 W/cm^2. In this set of experiment, due to the the sparse configuration of pin fins and low flow rate condition compared to previous experiments done on dense device, higher quality of vapor in the microgap was achievable.

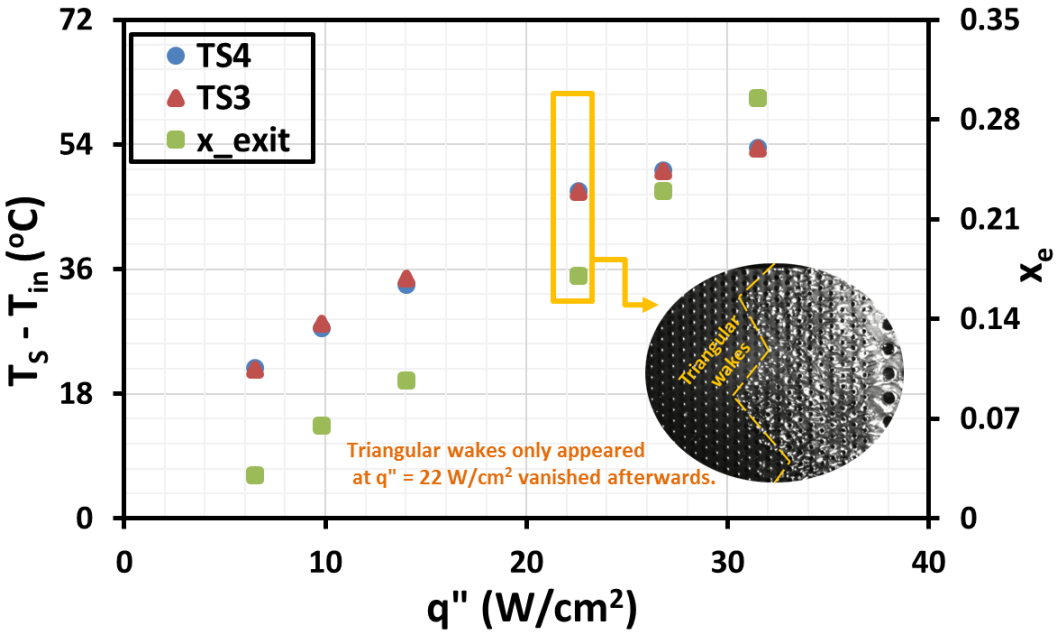

5.4.4 Two-Phase Heat Transfer Coefficient

A two-phase length in the microgap is calculated by subtracting the single-phase length from the entire heated microgap length. A 1-D fin analysis with the adiabatic tip assumption is used and the average two-phase heat transfer coefficient is computed, and shown in Figure 5.7. Tests 4-6 showed the highest thermal performance compared to the other tests since the inlet temperature was set to a low value of 10 °C. In tests 1-3 on the dense device with mass flux of 1586 kg/m^{2}s, even though the mass velocity is the highest among all tests presented in this chapter, the minimum calculated two-phase heat transfer coefficient is found, since only a small portion of the footprint area in the microgap was covered by two-phase flow. The dry-out condition which was observed for this test at the maximum heat flux, resulted in drop in thermal performance. The results are compared with the existing literature [10, 32] for water at 420 kg/m^{2}s and R-123 at 976 kg/m^{2}s and 2349 kg/m^{2}s, respectively.

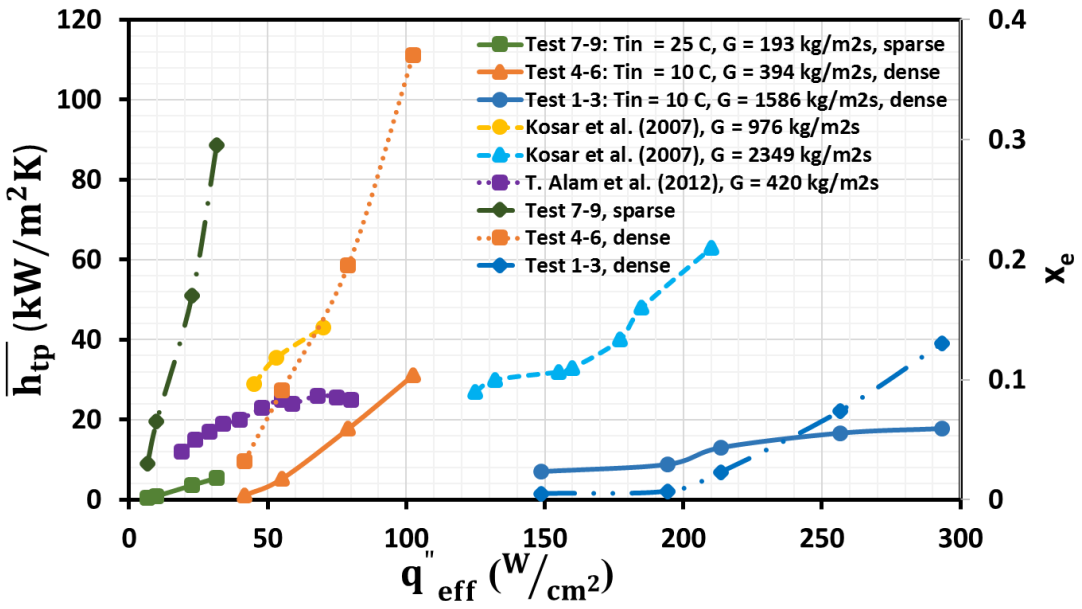

Figure 5.7 Average two-phase heat transfer for representative test conditions and comparison with the existing literature.

5.4.5 Single-Phase Friction Factor Correlation

Pressure drop across a tube bank can be obtained using the expression:

$$\Delta P = N_p f \rho u^2{}_{max} \quad (1)$$

To obtain a correlation that fits to all experiments done on dense and sparse devices from chapter 3 to 5, geometrical parameters should be carefully paid attention. Reviewing the relations in the literature from other studies to calculate f, the correlation should have the following components:

$$f = C(\frac{S_L}{D_p})^a(\frac{S_T}{D_p})^b(\frac{H_{ch}}{D_p})^c Re^d \quad (2)$$

C, a, b, c, and d are all constants determined from experimental data. The terms incorporate S_L (longitudinal pitch), S_T (transversal pitch), H_{ch} (channel height), Re

(Reynolds number), and D_p (pin fins diameter) for all dense and sparse tests. The expression for the friction factor based on the above-mentioned model is developed as:

$$f = 5\left(\frac{S_L}{D_p}\right)^{-2.7}\left(\frac{S_T}{D_p}\right)^{-1.3}\left(\frac{H_{ch}}{D_p}\right)^{5} Re^{-0.05} \quad (3)$$

The Reynolds number is determined based on the hydraulic diameter of the pin fins and the maximum velocity u_{max} flowing in the microgaps. The MAE for the above correlation is 10.2% which is compared with other correlations in the literature in the below table:

Table 5.2 Comparison of single-phase friction factor with the existing literature and the corresponding MAE

Study	Correlation	Scale	MAE
Present study	$f = 5\left(\frac{S_L}{D_p}\right)^{-0.02}\left(\frac{S_T}{D_p}\right)^{-0.37}\left(\frac{H_{ch}}{D_p}\right)^{5} Re^{-0.22}$	Micro	10.2%
Kosar et al. [12]	$f = \pi_1 + \pi_2$ $\pi_1 = \frac{1739}{Re_f^{107}}\left(\frac{h_f/D_f}{h_f/D_f + 1}\right)^{11}\left(\frac{S_t S_L}{A_f}\right)^{-0.3}$ $\pi_2 = \frac{345}{Re^{1}}\left(\frac{h_f/D_f}{h_f/D_f + 1}\right)^{2}\left(\frac{S_t S_L}{A_f}\right)^{-0.3}$	Micro	51.76%
Qu and Siu-Ho [72]	$f = 20.09 Re_f^{-0.547}$	Micro	45.2%
Prasher [73]	$f = 3.5\left(\frac{h_f}{D_f}\right)^{0.724}\left(\frac{S_L - D_f}{D_f}\right)^{-0.442}\left(\frac{S_t - D_f}{D_f}\right)^{-0.245} Re^{-0.58}$	Micro	21.7%

Wan Z. and Joshi Y. [74]	$Re < 100: f = 2.15Re^{-0.613}$ $Re > 100: f = 0.9807Re^{-0.440}$	Micro	23.4%

In Figure 5.8, the experimentally obtained pressure drop data is compared with those predicted utilizing the correlation in Equation 3. The predictive accuracy of a correlation is defined by the mean absolute error equation:

$$\text{MAE} = \frac{1}{n}\sum\left|\frac{f_{pred} - f_{exp}}{f_{exp}}\right| \times 100\% \tag{4}$$

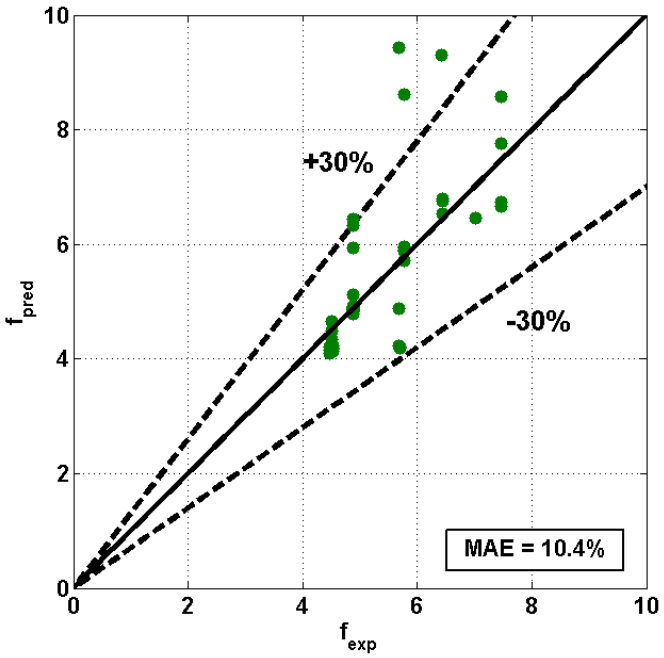

Figure 5.8 Comparison of experimentally obtained single-phase friction factor data with prediction.

5.4.6 Two-Phase Heat Pressure Drop Correlation

In this section, a correlation for two-phase pressure drop is developed which is inspired by the method explained by Qu and Mudawar [75]. The pressure drop across the microgap in this study includes two different terms:

$$\Delta P = \Delta P_{sp} + \Delta P_{tp} \tag{5}$$

The pressure gradient equivalent from friction factor across an array of pin fins can be written in the form of:

$$\Delta P_{sp} = \int -\left(\frac{dP}{dz}\right)_{sp} , dz = \sum_{j=1}^{N_{tr}} f_{sp,i} \frac{{G^2}_{max}}{2\rho_l} \tag{6}$$

where N_{tr} is the number of row of the pin fins where the transition between single-phase and two-phase flow happens and $f_{sp,i}$ is the friction factor at j^{th} row of pin fins from inlet through $Re_j = G_{max} D/\mu$.

The two-phase component of the pressure drop in equation 5 can be splitted to two terms of frictional and accelerational:

$$\Delta P = \Delta P_{tp,f} + \Delta P_{tp,a} \tag{7}$$

where $\Delta P_{tp,f}$ stands for the frictional effects and $\Delta P_{tp,a}$ accounts for the acceleration part of the pressure drop.

The frictional pressure drop can be obtained from:

$$\Delta P_{tp,f} = \int -\left(\frac{dP}{dz}\right)_{tp,f} , dz = \int -\left(\frac{dP}{dz}\right)_{l} {\varphi_l}^2 dz \tag{8}$$

where ${\varphi_l}^2$ is the two-phase multipier and is defined in the form of:

$$\varphi_l{}^2 = \left[\frac{(dP/dz)_{tp,f}}{(dP/dz)_l}\right]^{0.5} \quad (9)$$

and subscript l denotes the frictional pressure drop that would result if the liquid flows alone at a mass flux of $G_{max}\ (1-x)$.

Therefore, the frictional pressure drop for a bank of pin fins can be expressed as:

$$\Delta P_{tp,f} = \sum_{j=N_{tr}}^{N_t} f_{sp,i} \frac{G^2{}_{max}(1-x)^2}{2\rho_l} \varphi_l{}^2 \quad (10)$$

The acceleration term is:

$$-\left(\frac{dP}{dz}\right)_{tp,a} = G^2{}_{max} \frac{d}{dz}\left[\frac{x^2}{\rho_v \alpha} - \frac{(1-x)^2}{\rho_l(1-\alpha)}\right] \quad (11)$$

where α stands for void fraction. The accelerational pressure drop can be eventually represented in the form of:

$$\Delta P_{tp,a} = G^2{}_{max}\left[\frac{x^2}{\rho_v \alpha} - \frac{(1-x)^2}{\rho_l(1-\alpha)}\right]_{outlet} - G^2{}_{max}\left[\frac{x^2}{\rho_v \alpha} - \frac{(1-x)^2}{\rho_l(1-\alpha)}\right]_{inlet} \quad (12)$$

Total two-phase pressure drop can be obtain by summation of equations 10 and 12.

The Chisholm and Laird [76] two-phase multipier is formulated utilizing the Martinelli parameter as:

$$\varphi_l{}^2 = 1 + \frac{C}{X} + \frac{1}{X^2} \quad (13)$$

where C is an empirically determined constant and X is the Martinelli parameter:

$$X = \left(\frac{\rho_G}{\rho_L}\right)^{0.5} \left(\frac{\mu_L}{\mu_G}\right)^{0.1} \left(\frac{1-x}{x}\right)^{0.9} \quad (14)$$

where the x is defined as the exit quality of vapor in the current study.

The homogeneous flow void fraction α_H is used in the calculations which is defined as:

$$\alpha_H = \frac{x/\rho_v}{\frac{(1-x)}{\rho_l}+\frac{x}{\rho_v}} \tag{15}$$

In the present study, the empirical constant C is considered to be as a function of Reynolds number and geometrical parameters defined as:

$$C = a\,(\frac{S_L}{D})^b(\frac{S_L}{D})^c Re^d \tag{16}$$

a, b, c, and d are determined based on the correlation that is developed based on utilizing the collected experimental data and investigating the best fit curve. The obtained correlation is in the form of:

$$C = 1.19\,(\frac{S_L}{D})^{1.9}(\frac{S_L}{D})^{2.4} Re^{0.05} \tag{17}$$

The MAE for the above correlation is 9.1%. The comparison between the predicted and the experimental data is shown in Figure 5.9.

Below table represents the comparison of the correlations in the literature for C with the current study experimental data and the corresponding MAE.

Table 5.3 Comparison of two-phase pressure drop correlations with the existing literature and the corresponding MAE

Study	C	Scale	MAE

Present study	$C = 1.19\,(\frac{S_L}{D})^{1.9}(\frac{S_L}{D})^{2.4}Re^{0.05}$	Micro	9.1%
Krishnamurthy and Peles [77]	$0.0358\ Re_{sp,l}$	Micro	92.7%
Qu and Mudawar [75]	$21(1-\exp(-319d_h))(0.00418G_{max}+0.0613)$	Micro	121.3%
Reeser et al. [33]	8	Micro	147.1%
Lockhart and Martinelli [78]	5	Micro	77.3%

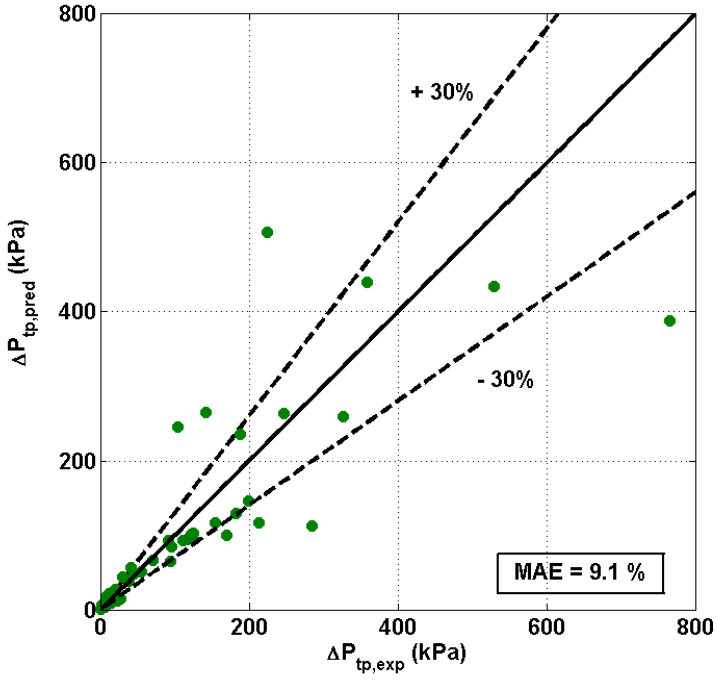

Figure 5.9 Comparison of experimentally obtained two-phase pressure drop data with predictions.

Geometrical effects are important in the present study since different geometry of devices are considered as test vehicles. Therefore, in order to improve the error associated with comparison with the correlations in the literature, a unifying correction multiplier is added to some of the above-mentioned literature to improve the MAE of the results. A significant improvement is resulted which is listed in .

Table 5.4.

Table 5.4 Effect of correction multiplier on improving the comparison of the correlations in the literature with the current study

Study	C	Correction multiplier	MAE	MAE

			(without correction factor)	(correction factor applied)
Krishnamurthy and Peles [77]	$0.0358\ Re_{sp,l}$	$(\frac{S_L}{D})^{-1.14}(\frac{S_T}{D})^{3.82}$	92%	48%
Reeser et al. [33]	8		147.1%	48%
Lockhart and Martinelli [78]	5		77.3%	38%

Figure 5.10 shows the comparison of the experimentally determined two-phase pressure drop with predictions as well as the effect of correction multiplier based on Krishnamurthy and Peles [77], Reeser et al. [33], and Lockhart and Martinelli [78]. The unifying multiplier

has made the works in the literature to be in a much better fit with the experimental collected data.

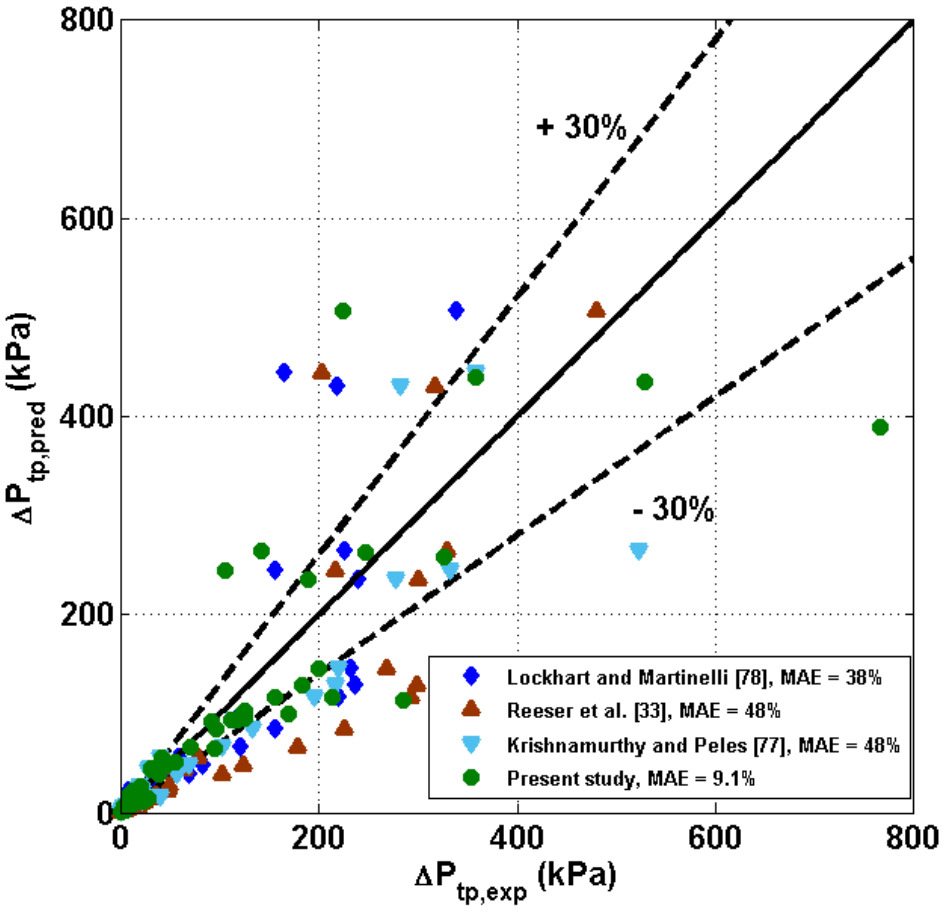

Figure 5.10 Comparison of the experimentally determined two-phase pressure drop with predictions as well as the effect of correction factor based on Krishnamurthy and Peles [77], Reeser et al. [33], and Lockhart and Martinelli [78]

5.4.7 Single-Phase Heat Transfer Coefficient Correlation

The Nu for a flow over arrays of tube banks is conventionally in the form of:

$$Nu = CRe^{a}Pr^{b} \tag{5}$$

Which is developed by Zukauskas [79] where C, a, and b are constants. Since the height, shape and spacing of pin fins are changing in the current study, the new correlation incorporates more components to further define the geometry of pin fins. Utilizing the collected experimental data and investigating the best fit curve, the above expression for the single-phase flow data is modified and presented in the form of:

$$Nu_{sp} = C\left(\frac{S_L}{D_p}\right)^a \left(\frac{S_T}{D_p}\right)^b \left(\frac{H_{ch}}{D_p}\right)^c Re^d Pr^e \left(\frac{Pr}{Pr_s}\right)^f \quad (6)$$

Where Pr_s is the surface Prandtl number and C, a, b, c, d, e, and f are the constants. The correlation that presents all single-phase experimental data is developed in the form of:

$$Nu_{sp} = 0.001\left(\frac{S_L}{D_p}\right)^{-0.17} \left(\frac{S_T}{D_p}\right)^{0.07} \left(\frac{H_{ch}}{D_p}\right)^{-0.76} Re^{0.88} Pr^{2.46} \left(\frac{Pr}{Pr_s}\right)^{0.09} \quad (7)$$

Or

$$h_{sp} = 0.001\left(\frac{S_L}{D_p}\right)^{-0.17} \left(\frac{S_T}{D_p}\right)^{0.07} \left(\frac{H_{ch}}{D_p}\right)^{-0.76} Re^{0.88} Pr^{2.46} \left(\frac{Pr}{Pr_s}\right)^{0.09} \left(\frac{k_{f,sp}}{D_p}\right) \quad (8)$$

The Reynolds number is determined based on the hydraulic diameter of the pin fins and the maximum velocity u_{max} flowing in the microgaps. The MAE for the above correlation is 6.7% which is compared with other correlations in the literature in the below table:

Table 5.5 Comparison of single-phase heat transfer coefficient with the existing literature and the corresponding MAE

Study	Correlation	Scale	MAE
Present study	$Nu_{sp} = 0.001\,(\frac{S_L}{D_p})^{-0.17}(\frac{S_T}{D_p})^{0.07}\,(\frac{H_{ch}}{D_p})^{-0.76}\,Re^{0.88}Pr^{2.46}(\frac{Pr}{Pr_s})^{0.09}$	Micro	6.7%
Kosar and Peles [80]	$Nu_f = 0.0423{Re_f}^{0.99}Pr^{0.21}(\frac{Pr}{Pr_s})^{0.25}$	Micro	63.3%
Qu and Siu-Ho [81]	$Nu_f = 0.0241{Re_f}^{0.953}Pr^{0.36}(\frac{Pr}{Pr_s})^{0.25}$	Micro	35.7%
Zukauskas [79]	$Nu_f = 0.9{Re_f}^{0.4}Pr^{0.36}(\frac{Pr}{Pr_s})^{0.25}$	Micro	41.2%
Tullius et al. [82]	$Nu = 0.08\,(\frac{S_L}{D_f})^{0.2}(\frac{S_T}{D_f})^{0.2}\,(\frac{H_f}{D_f})^{0.25}(1+\frac{dh}{D_f})Re^{0.6}Pr^{0.36}(\frac{Pr}{Pr_s})^{0.25}$	Micro	33.5%

The experimental sinlge-phase Nu data is compared with predicted ones obtained from Equation 7. The results are represented in Figure 5.11. The calculated MAE is 6.7%.

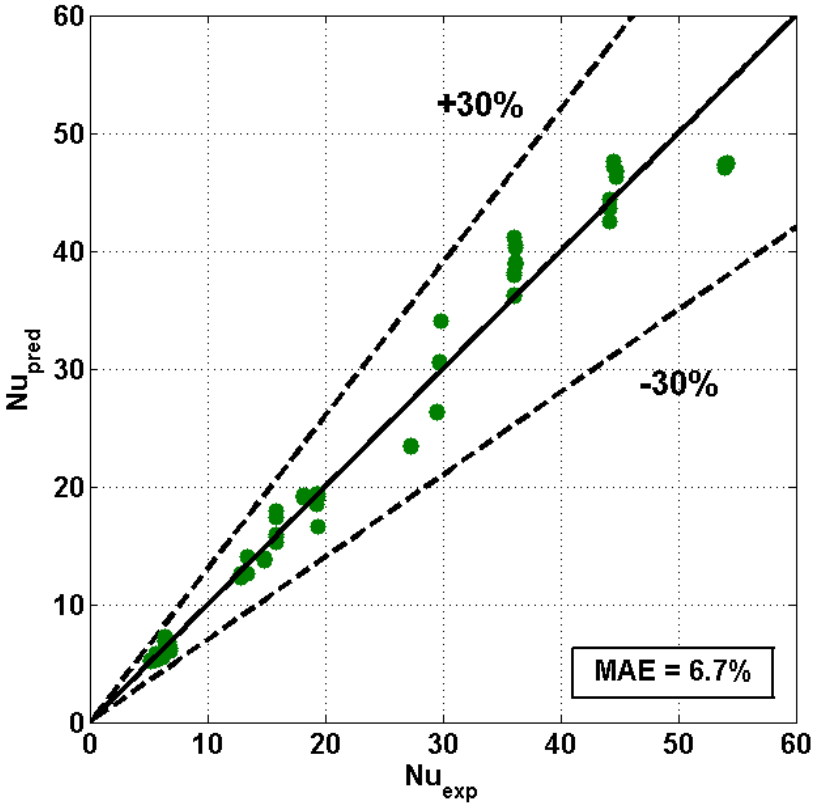

Figure 5.11 Comparison of experimentally obtained single-phase heat transfer coefficient data with prediction correlation.

5.4.8 Two-Phase Heat Transfer Coefficient Correlation

In order to obtain a correlation for two phase heat transfer coefficient, the method here is inspired by Kirshnamurthy and Peles [77]. In the present study, chen-type correlation is used to account for the two-phase heat transfer coefficient. Chen [83] suggest the following expression:

$$h_{tp} = Fh_{sp} \tag{9}$$

Where F is the enhancement factor and is defined as:

$$F = (X)^a \tag{10}$$

X is the Martinelli parameter [84] and is defined by equation 14.

The expression for the h_{sp} already has the geometrical parameters and operating conditions non-dimensional parameters. Since all the experimental data follows subcooled inlet conditions, another dimensionless parameter is represented here:

$$\frac{C_p(T_{sat} - T_{in})}{h_{fg}} \tag{12}$$

Which plays a significant role in taking account for inlet subcooled condition. Having all components employed in the first equation, the two-phase heat transfer coefficient is presented in the form of:

$$h_{tp} = (X)^a \frac{C_p(T_{sat} - T_{in})}{h_{fg}} h_{sp} \tag{13}$$

Therefore, by substituting all above parameters in the two-phase heat transfer coefficient equation, it becomes:

$$h_{tp} = C(X)^a (\frac{C_p(T_{sat} - T_{in})}{h_{fg}})^a \left(\frac{S_L}{D_p}\right)^b \left(\frac{S_T}{D_p}\right)^c \left(\frac{H_{ch}}{D_p}\right)^d Re^e Pr^f (\frac{Pr}{Pr_s})^g \tag{14}$$

Having the collected data and investigating the best fit curve, the final correlation for the two-phase heat transfer coefficient data is:

$$h_{tp} = 0.04(X)^{-0.6} (\frac{C_p(T_{sat} - T_{in})}{h_{fg}})^{0.9} \left(\frac{S_L}{D_p}\right)^{-0.17} \left(\frac{S_T}{D_p}\right)^{0.07} \left(\frac{H_{ch}}{D_p}\right)^{-0.76} Re^{0.88} Pr^{2.46} \left(\frac{Pr}{Pr_s}\right)^{0.09} \tag{15}$$

In Figure 5.8, the experimentally obtained pressure drop data is compared with those predicted utilizing the correlation in Equation 3.The MAE for the above correlation is 9.6%.

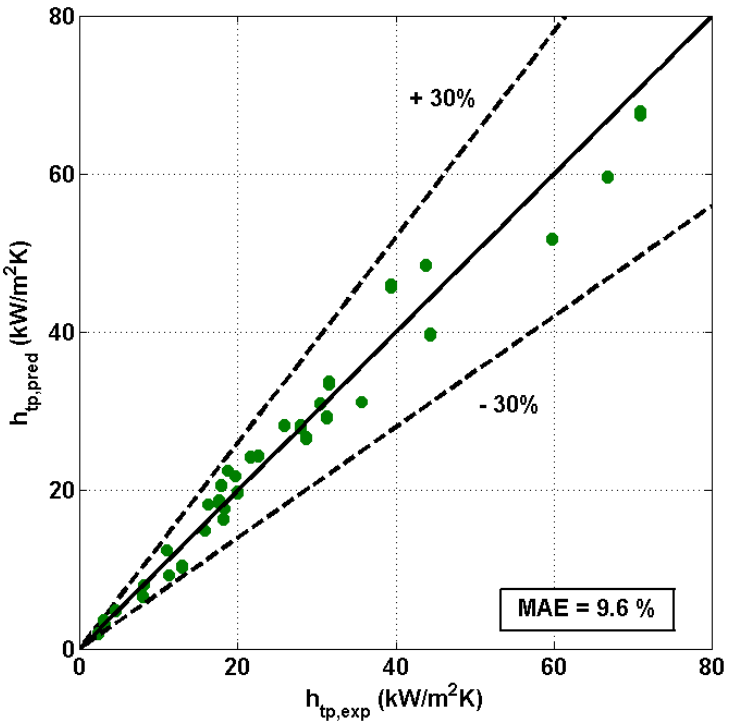

Figure 5.12 Comparison of experimentally obtained two-phase heat transfer coefficient data with prediction correlation.

Table below represents the comparison of the two-phase heat transfer coefficient correlation of the present study with the existing literature:

Table 5.6 Comparison of two-phase heat transfer coefficient with the existing literature and the corresponding MAE

Study	Correlation	Scale	MAE
Present study	$h_{tp} = 0.04(X)^{-0.6}\left(\frac{C_p(T_{sat}-T_{in})}{h_{fg}}\right)^{0.9}\left(\frac{S_l}{D_p}\right)^{-0.17}\left(\frac{S_T}{D_p}\right)^{0.07}\left(\frac{H_{ch}}{D_p}\right)^{-0.76} Re^{0.88} Pr^{2.46}\left(\frac{Pr}{Pr_s}\right)^{0.09}$	Micro	9.6%
Kosar and Peles [47]	$h_{tp} = 0.76\left(\frac{S_t}{d}\right)^{0.16}\left(\frac{S_l}{d}\right)^{0.16}\left(\frac{L}{d}\right)^{-0.11} {Re_{tp}}^{0.33}\left(\frac{k_{f,tp}}{d}\right)$	Micro	83.4%
Oh and Son [85]	$h_{tp} = 0.034 {Re_f}^{0.8} Pr^{0.3}[1.58\left(\frac{1}{X_{tt}}\right)^{0.87}]\left(\frac{k_f}{D_h}\right)$	Micro	61.2%
Kosar et al. [37]	$h_{tp} = 4.068 \times 10^4 (Re_l)^{0.12}(1-x_e)^{0.8}\left(\frac{1-x_e}{x_e}\right)^{0.02}$	Micro	57%
Li and Wu [86]	$h_{tp} = 334 Bo^{0.3}(BdRe_f{}^{0.36})^{0.4}\frac{k_f}{D_h}, Bd = \frac{g(\rho_f-\rho_g){D_h}^2}{\sigma}$	Micro	97.1%

Since all the tests in the current study are performed in subcooled inlet condition, in order to improve the comparison of the experimental data with the existing literature, the correction multiplier $\left(\frac{C_p(T_{sat}-T_{in})}{h_{fg}}\right)$ is added to some of the above-mentioned literatures to improve the MAE of the results. A huge improvement is observed by applying a unifying correlction multiplier and the results a=re summarized in Table *5.7*.

Figure 5.13 shows the comparison of the experimentally determined two-phase heat transfer coefficient with predictions as well as the correction multiplier effect based on: a) Kosar and Peles [47], b) Kosar et al. [37]. The correction multiplier has significantly improved the error to best fit the experimental data that are all collected in subcooled inlet condition.

Table 5.7 Effect of correction multiplier on improving the comparison of the correlations in the literature with the current study

Study	Correction multiplier	MAE (without correction factor)	MAE (correction factor applied)
Kosar and Peles [47]	$(\frac{C_p(T_{sat}-T_{in})}{h_{fg}})^{-0.66}$	83.4%	44%
Kosar et al. [37]		57%	42%

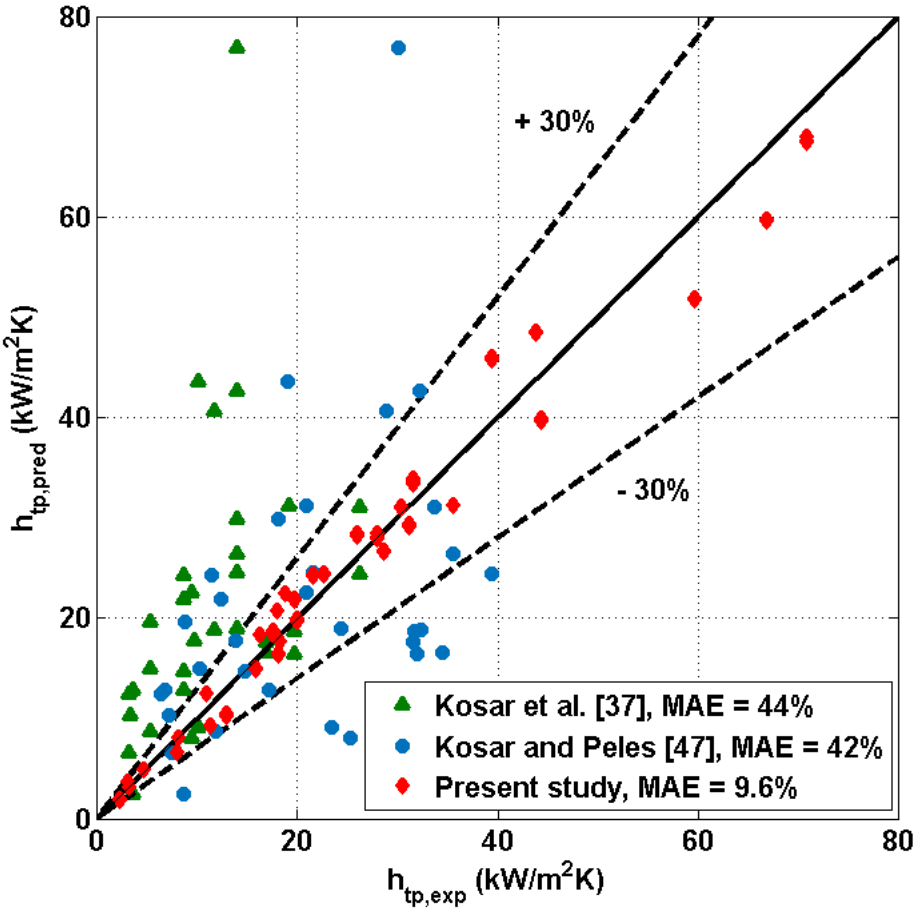

Figure 5.13 the comparison of the experimentally determined two-phase heat transfer coefficient with predictions as well as the correction multiplier effect based on Kosar and Peles [47] and Kosar et al. [37]

CHAPTER 6. CONCLUSIONS AND RECOMMENDATIONS

This research addresses the two-phase transfer behavor of R245fa refrigerant in microgaps populated with different different size of microstructures. For a range of heat flux up to almost 0.5 KW/cm^2 and mass flux up to 7,896 kg/m^{2}s, extensive number of experimentations are done to study the flow boiling behavior of R245fa and the flow regimes it creates in the microgaps.

Pin fins with staggered arrangement and in cylindrical and hydrofoil shapes, were fabricated in microgaps to enhance heat transfer performance. The pin fins were wth a height, pitch and diameter of 200 μm, 200-450 μm, and 150, respectively. A closed flow loop was constructed capble of running thermal and hydraulic experimentations of devices. Bubbly, foggy, and slug flow regimes were detected in the microgaps and a flow regime mapping was developed to help validat the convective boiling mechanism. The nucleated bubbles migrated in transverse direction instead of directly moving dounstream of the microgap due to the very smaill and limited gap between pin fins.The liquid films of adjacent pin fins merged together in them icrogap by increasing the heat flux. Vapor acc Single-phase and two-phase heat transfer distributions were generally dependant on mostly heat flux and mass flux values. In experiments with flow rates as low as 15 mL/min, the majority of the microgap was covered by two-phase flow since the vapors had more opportunity to become advanced and get expanded in the microgap. Triangular wakes were observed for these experiments. For the cases with dry-out conditions or with small two-phase region in the microgap, the thermal performance was dropped significantly. In dry-out conditions, for the dense and sparse devices, this reduction was by 50% and 80% of the

maximum value, respectively. The single-phase heat transfer performance was higher in these situations. According to flow visualizations, vapor bubbles departure in the microgap was observed be strongly dependant on surface temperature. Overall, the experiments done on sparse chips with mid-range flow rate of 100 mL/min and inlet temperature of 13 ^{o}C (below R245fa saturation temperature), showed the highest heat transfer performance. Table 6.1 summarizes the main key factors from all tests done on the sparse and dense devices:

Table 6.1 Summary of key points from all tests

	Pin Fin Shape	Pin Fin Arrangements	Longitudinal Pitch (µm)	Transversal Pitch (µm)	Mass Flux (kg/m^{2}s)	Heat Flux (W/cm^2)	Flow Rate (mL/min)	Two-Phase Heat Transfer Coefficient (kW/m^{2}s)	Pressure Drop (kPa)	Exit Quality
Symmetric Devices	Circular	Staggered	200	200	781 - 7,896	11 - 498	15 - 150	8 – 72	20 – 500	0 - 1
	Circular		400	400	312 - 2,105	12 - 207	15 - 100	4 – 80	2 – 27	0 - 1
Asymmetric Devices	Circular		135	50	394 - 1,586	7 - 32	15	8 – 90	1 – 3	0.02 – 0.3
	Hydrofoil		450	450	193	41 - 293	30 - 120	2 - 8	21 - 91	0.02 – 0.38

Relating the high-speed flow visualizations to the surface temperature dataset for the onset of boiling conditions, the temperature drop of the heater on the two-phase was justifiable. The low saturation temperature in operating pressure allowed to increase the heat flux and subsequently the heat removal capacity of the chips. The overall pattern of the flow boiling in the microgap was significantly inspired by the inlet and outlet locations as well as inlet plenum geometry. Comparing the existing literature with the obtained data, showed reasonable agreement with the behavior of single-phase and two-phase heat transfer coefficients. The results showed that the area of two-phase region in the microgap has a significant role on the range of two phase heat transfer coefficient. The pressure drops across the chip for all the experiments done on dense devices were at least one order of

magnitude higher the identical experiments for the sparse device. Single-phase and two-phase pressure drop, single-phase heat transfer coefficient, and two-phase heat transfer coefficient correlations were developed for the current experimental data matching all devices experiments. The correlations are equipped with geometrical parameters in order to support a range of pin fin spacing diameter size. Since all the tests were performed under subcooled inlet condition, a non-dimensional parameter ($\frac{C_p(T_{sat}-T_{in})}{h_{fg}}$) was employed in the correlations to support this and increase the accuracy. The MAE for all these correlations were in the range of 6-10% which showed that the correlations were perfectly in agreement with the experimental data.

It would be useful to perform computational simulations on the geometries that have been studied here experimentally. This would allow for a better understanding of the flow behavior, and verification of the results. A simulation that is run in the range of heat flux and mass fluxes associated with the experimental ranges, can possibly predict flow regime one can expect.

In many of the experiments with high flow rate, only a small portion of the microgap was covered by two-phase flow. Therefore, decreasing the width of the foot print area can improve the thermal performance of the test devices by having a more efficient distribution of single-phase and two-phase region across the gap. Figure 6.1 shows two different microgaps one with shorter to better understand the idea.

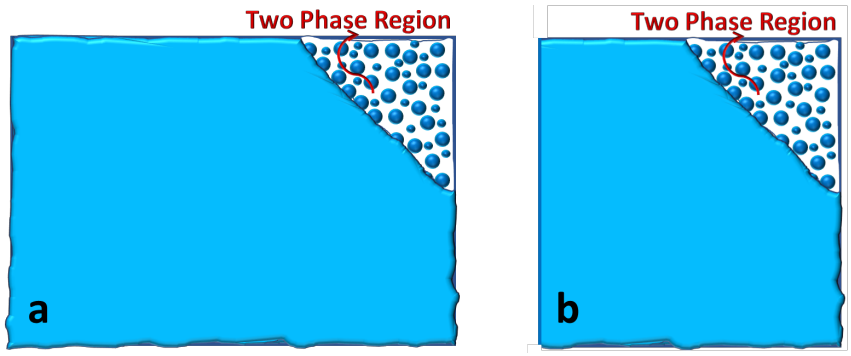

Figure 6.1 microgaps with: a) larger length b) shorter length

REFERENCES

[1] S. Krishnamurthy, Y. Peles, Flow boiling of water in a circular staggered micro-pin fin heat sink, International Journal of Heat and Mass Transfer, 51(5) (2008) 1349-1364.

[2] M. Law, P.-S. Lee, K. Balasubramanian, Experimental investigation of flow boiling heat transfer in novel oblique-finned microchannels, International Journal of Heat and Mass Transfer, 76 (2014) 419-431.

[3] D. Lorenzini, C. Green, T.E. Sarvey, X. Zhang, Y. Hu, A.G. Fedorov, M.S. Bakir, Y. Joshi, Embedded single phase microfluidic thermal management for non-uniform heating and hotspots using microgaps with variable pin fin clustering, International Journal of Heat and Mass Transfer, 103 (2016) 1359-1370.

[4] Y. Zhang, M. Bakir, Independent interlayer microfluidic cooling for heterogeneous 3D IC applications, Electronics Letters, 49(6) (2013) 404-406.

[5] P. Asrar, X. Zhang, C.D. Woodrum, C.E. Green, P.A. Kottke, T.E. Sarvey, S. Sitaraman, A. Fedorov, M. Bakir, Y.K. Joshi, Flow boiling of R245fa in a microgap with integrated staggered pin fins, in: Thermal and Thermomechanical Phenomena in Electronic Systems (ITherm), 2016 15th IEEE Intersociety Conference on, IEEE, 2016, pp. 1007-1012.

[6] M. Arik, A. Bar-Cohen, Effusivity-based correlation of surface property effects in pool boiling CHF of dielectric liquids, International Journal of Heat and Mass Transfer, 46(20) (2003) 3755-3764.

[7] J. Lee, I. Mudawar, Fluid flow and heat transfer characteristics of low temperature two-phase micro-channel heat sinks–Part 1: Experimental methods and flow visualization results, International Journal of Heat and Mass Transfer, 51(17) (2008) 4315-4326.

[8] A. Watwe, A. Bar-Cohen, A. McNeil, Combined pressure and subcooling effects on pool boiling from a PPGA chip package, Journal of Electronic Packaging, 119(2) (1997) 95-105.

[9] R. Zhuan, W. Wang, Simulation of subcooled flow boiling in a micro-channel, international journal of refrigeration, 34(3) (2011) 781-795.

[10] T. Alam, P.S. Lee, C.R. Yap, L. Jin, Experimental investigation of local flow boiling heat transfer and pressure drop characteristics in microgap channel, International Journal of Multiphase Flow, 42 (2012) 164-174.

[11] D.W. Kim, E. Rahim, A. Bar-Cohen, B. Han, Thermofluid characteristics of two-phase flow in micro-gap channels, in: Thermal and Thermomechanical Phenomena in Electronic Systems, 2008. ITHERM 2008. 11th Intersociety Conference on, IEEE, 2008, pp. 979-992.

[12] A. Koşar, Y. Peles, Convective flow of refrigerant (R-123) across a bank of micro pin fins, International Journal of Heat and Mass Transfer, 49(17) (2006) 3142-3155.

[13] D. Bogojevic, K. Sefiane, A. Walton, H. Lin, G. Cummins, D. Kenning, T. Karayiannis, Experimental investigation of non-uniform heating effect on flow boiling instabilities in a microchannel-based heat sink, International Journal of Thermal Sciences, 50(3) (2011) 309-324.

[14] C.T. Lu, C. Pan, A highly stable microchannel heat sink for convective boiling, Journal of Micromechanics and microengineering, 19(5) (2009) 055013.

[15] A. Megahed, Experimental investigation of flow boiling characteristics in a cross-linked microchannel heat sink, International Journal of Multiphase Flow, 37(4) (2011) 380-393.

[16] K. Chang, C. Pan, Two-phase flow instability for boiling in a microchannel heat sink, International Journal of Heat and Mass Transfer, 50(11) (2007) 2078-2088.

[17] T. Harirchian, S.V. Garimella, An investigation of flow boiling regimes in microchannels of different sizes by means of high-speed visualization, in: Thermal and Thermomechanical Phenomena in Electronic Systems, 2008. ITHERM 2008. 11th Intersociety Conference on, IEEE, 2008, pp. 197-206.

[18] S.G. Kandlikar, A.V. Bapat, Evaluation of jet impingement, spray and microchannel chip cooling options for high heat flux removal, Heat Transfer Engineering, 28(11) (2007) 911-923.

[19] J. Lee, I. Mudawar, Low-temperature two-phase microchannel cooling for high-heat-flux thermal management of defense electronics, IEEE transactions on components and packaging technologies, 32(2) (2009) 453-465.

[20] S.N. Ritchey, J.A. Weibel, S.V. Garimella, Effects of non-uniform heating on the location and magnitude of critical heat flux in a microchannel heat sink, (2015).

[21] C.B. Tibirica, G. Ribatski, Flow boiling in micro-scale channels–Synthesized literature review, International Journal of Refrigeration, 36(2) (2013) 301-324.

[22] Y. Lie, J. Ke, W. Chang, T. Cheng, T. Lin, Saturated flow boiling heat transfer and associated bubble characteristics of FC-72 on a heated micro-pin-finned silicon chip, International Journal of Heat and Mass Transfer, 50(19-20) (2007) 3862-3876.

[23] J. Sheehan, D.W. Kim, A. Bar-Cohen, Thermal Imaging of Two-Phase Coooled Microgap Channel Wall, in: ASME 2009 InterPACK Conference collocated with the ASME 2009 Summer Heat Transfer Conference and the ASME 2009 3rd International Conference on Energy Sustainability, American Society of Mechanical Engineers, 2009, pp. 491-499.

[24] W. Qu, A. Siu-Ho, Experimental study of saturated flow boiling heat transfer in an array of staggered micro-pin-fins, International Journal of Heat and Mass Transfer, 52(7-8) (2009) 1853-1863.

[25] A. Ma, J. Wei, M. Yuan, J. Fang, Enhanced flow boiling heat transfer of FC-72 on micro-pin-finned surfaces, International Journal of Heat and Mass Transfer, 52(13-14) (2009) 2925-2931.

[26] T. Harirchian, S.V. Garimella, Microchannel size effects on local flow boiling heat transfer to a dielectric fluid, International Journal of Heat and Mass Transfer, 51(15) (2008) 3724-3735.

[27] T.-H. Yen, M. Shoji, F. Takemura, Y. Suzuki, N. Kasagi, Visualization of convective boiling heat transfer in single microchannels with different shaped cross-sections, International Journal of Heat and Mass Transfer, 49(21-22) (2006) 3884-3894.

[28] D. Bogojevic, K. Sefiane, G. Duursma, A. Walton, Bubble dynamics and flow boiling instabilities in microchannels, International Journal of Heat and Mass Transfer, 58(1-2) (2013) 663-675.

[29] C.-J. Kuo, Y. Peles, Local measurement of flow boiling in structured surface microchannels, International journal of heat and mass transfer, 50(23-24) (2007) 4513-4526.

[30] G. Wang, P. Cheng, H. Wu, Unstable and stable flow boiling in parallel microchannels and in a single microchannel, International Journal of Heat and Mass Transfer, 50(21-22) (2007) 4297-4310.

[31] S.A. Isaacs, Y.J. Kim, A.J. McNamara, Y. Joshi, Y. Zhang, M.S. Bakir, Two-phase flow and heat transfer in pin-fin enhanced micro-gaps, in: Thermal and Thermomechanical Phenomena in Electronic Systems (ITherm), 2012 13th IEEE Intersociety Conference on, IEEE, 2012, pp. 1084-1089.

[32] A. Koşar, Y. Peles, Boiling heat transfer in a hydrofoil-based micro pin fin heat sink, International Journal of Heat and Mass Transfer, 50(5) (2007) 1018-1034.

[33] A. Reeser, A. Bar-Cohen, G. Hetsroni, High quality flow boiling heat transfer and pressure drop in microgap pin fin arrays, International Journal of Heat and Mass Transfer, 78 (2014) 974-985.

[34] C. Woodcock, X. Yu, J. Plawsky, Y. Peles, Piranha Pin Fin (PPF)—Advanced flow boiling microstructures with low surface tension dielectric fluids, International Journal of Heat and Mass Transfer, 90 (2015) 591-604.

[35] P. Asrar, X. Zhang, C.E. Green, P.A. Kottke, T.E. Sarvey, A. Fedorov, M.S. Bakir, Y.K. Joshi, Flow visualization of two phase flow of R245fa in a microgap with integrated staggered pin fins, in: Thermal Measurement, Modeling & Management Symposium (SEMI-THERM), 2016 32nd, IEEE, 2016, pp. 86-89.

[36] M.K. Sung, I. Mudawar, Experimental and numerical investigation of single-phase heat transfer using a hybrid jet-impingement/micro-channel cooling scheme, International journal of heat and mass transfer, 49(3-4) (2006) 682-694.

[37] A. Koşar, C.-J. Kuo, Y. Peles, Boiling heat transfer in rectangular microchannels with reentrant cavities, International Journal of Heat and Mass Transfer, 48(23-24) (2005) 4867-4886.

[38] S. Krishnamurthy, Y. Peles, Flow boiling heat transfer on micro pin fins entrenched in a microchannel, Journal of Heat Transfer, 132(4) (2010) 041007.

[39] T. Alam, P.S. Lee, C.R. Yap, L. Jin, A comparative study of flow boiling heat transfer and pressure drop characteristics in microgap and microchannel heat sink and an evaluation of microgap heat sink for hotspot mitigation, International Journal of Heat and Mass Transfer, 58(1-2) (2013) 335-347.

[40] A. Morshed, T.C. Paul, J.A. Khan, Effect of cross groove on flow boiling in a microgap, in: ASME 2012 Heat Transfer Summer Conference collocated with the ASME 2012 Fluids Engineering Division Summer Meeting and the ASME 2012 10th International Conference on Nanochannels, Microchannels, and Minichannels, American Society of Mechanical Engineers, 2012, pp. 457-463.

[41] X. Dai, F. Yang, R. Fang, T. Yemame, J.A. Khan, C. Li, Enhanced single-and two-phase transport phenomena using flow separation in a microgap with copper woven mesh coatings, Applied Thermal Engineering, 54(1) (2013) 281-288.

[42] T. David, D. Mendler, A. Mosyak, A. Bar-Cohen, G. Hetsroni, Thermal management of time-varying high heat flux electronic devices, Journal of Electronic Packaging, 136(2) (2014) 021003.

[43] C.L. Ong, S. Paredes, A. Sridhar, B. Michel, T. Brunschwiler, Radial hierarchical microfluidic evaporative cooling for 3-d integrated microprocessors, in: Fourth European Conference on Microfluidics, Limerick, Ireland, Dec, 2014, pp. 10-12.

[44] M. Schultz, F. Yang, E. Colgan, R. Polastre, B. Dang, C. Tsang, M. Gaynes, P. Parida, J. Knickerbocker, T. Chainer, Embedded two-phase cooling of large 3D compatible chips with radial channels, in: ASME 2015 International Technical Conference and Exhibition on Packaging and Integration of Electronic and Photonic Microsystems collocated with the ASME 2015 13th International Conference on Nanochannels, Microchannels, and Minichannels, American Society of Mechanical Engineers, 2015, pp. V003T010A007-V003T010A007.

[45] H.J. Lee, S.Y. Lee, Heat transfer correlation for boiling flows in small rectangular horizontal channels with low aspect ratios, International Journal of Multiphase Flow, 27(12) (2001) 2043-2062.

[46] Y. Yang, Y. Fujita, Flow boiling heat transfer and flow pattern in rectangular channel of mini-gap, in: ASME 2004 2nd International Conference on Microchannels and Minichannels, American Society of Mechanical Engineers, 2004, pp. 573-580.

[47] S. Krishnamurthy, Y. Peles, Flow boiling of water in a circular staggered micro-pin fin heat sink, International Journal of Heat and Mass Transfer, 51(5-6) (2008) 1349-1364.

[48] X. Yu, C. Woodcock, J. Plawsky, Y. Peles, An investigation of convective heat transfer in microchannel with Piranha Pin Fin, International Journal of Heat and Mass Transfer, 103 (2016) 1125-1132.

[49] O.A. Kabov, D. Zaitsev, V. Cheverda, A. Bar-Cohen, Evaporation and flow dynamics of thin, shear-driven liquid films in microgap channels, Experimental Thermal and Fluid Science, 35(5) (2011) 825-831.

[50] A. Bar-Cohen, J.R. Sheehan, E. Rahim, Two-phase thermal transport in microgap channels—theory, experimental results, and predictive relations, Microgravity Science and Technology, 24(1) (2012) 1-15.

[51] M. Ohadi, K. Choo, S. Dessiatoun, E. Cetegen, Next generation microchannel heat exchangers, Springer, 2013.

[52] E. Al-Hajri, A.H. Shooshtari, S. Dessiatoun, M.M. Ohadi, Performance characterization of R134a and R245fa in a high aspect ratio microchannel condenser, International journal of refrigeration, 36(2) (2013) 588-600.

[53] T. Adams, S. Abdel-Khalik, S. Jeter, Z. Qureshi, An experimental investigation of single-phase forced convection in microchannels, International Journal of Heat and Mass Transfer, 41(6-7) (1998) 851-857.

[54] F. Yang, M. Schultz, P. Parida, E. Colgan, R. Polastre, B. Dang, C. Tsang, M. Gaynes, J. Knickerbocker, T. Chainer, Local measurements of flow boiling heat transfer on hot spots in 3D compatible radial microchannels, in: ASME 2015 International Technical Conference and Exhibition on Packaging and Integration of Electronic and Photonic Microsystems collocated with the ASME 2015 13th International Conference on Nanochannels, Microchannels, and Minichannels, American Society of Mechanical Engineers, 2015, pp. V003T010A006-V003T010A006.

[55] A. Koşar, Y. Peles, Convective flow of refrigerant (R-123) across a bank of micro pin fins, International Journal of Heat and Mass Transfer, 49(17-18) (2006) 3142-3155.

[56] A. Koşar, Y. Peles, Boiling heat transfer in a hydrofoil-based micro pin fin heat sink, International Journal of Heat and Mass Transfer, 50(5-6) (2007) 1018-1034.

[57] A. Agrawal, S.G. Singh, A review of state-of-the-art on flow boiling of water in microchannel, International Journal of Microscale and Nanoscale Thermal and Fluid Transport Phenomena, 2(1) (2011) 1.

[58] F. Alfieri, M.K. Tiwari, I. Zinovik, D. Poulikakos, T. Brunschwiler, B. Michel, 3D integrated water cooling of a composite multilayer stack of chips, Journal of Heat Transfer, 132(12) (2010) 121402.

[59] C. Green, P. Kottke, X. Han, C. Woodrum, T. Sarvey, P. Asrar, X. Zhang, Y. Joshi, A. Fedorov, S. Sitaraman, A review of two-phase forced cooling in three-dimensional stacked electronics: technology integration, Journal of Electronic Packaging, 137(4) (2015) 040802.

[60] G.-Y. Su, M. Bucci, T. McKrell, J. Buongiorno, Transient boiling of water under exponentially escalating heat inputs. Part II: Flow boiling, International Journal of Heat and Mass Transfer, 96 (2016) 685-698.

[61] J.R. Mita, W. Qu, M.H. Kobayashi, F.E. Pfefferkorn, Experimental Study and Numerical Analysis of Water Single-Phase Pressure Drop Across an Array of Circular Micro-Pin-Fins, in: ASME/JSME 2011 8th Thermal Engineering Joint Conference, American Society of Mechanical Engineers, 2011, pp. T10131-T10131-10139.

[62] C.A. Konishi, W. Qu, F.E. Pfefferkorn, Experimental study of water liquid-vapor two-phase pressure drop across an array of staggered micropin-fins, Journal of Electronic Packaging, 131(2) (2009) 021010.

[63] C.A. Konishi, R. Hwu, W. Qu, F.E. Pfefferkorn, Experimental study and numerical analysis of water single-phase pressure drop across a micro-pin-fin array, in: 2010 14th International Heat Transfer Conference, American Society of Mechanical Engineers, 2010, pp. 711-719.

[64] S.G. Kandlikar, M. Bulut, An experimental investigation on flow boiling of ethylene-glycol/water mixtures, Journal of heat transfer, 125(2) (2003) 317-325.

[65] R. Mandel, S. Dessiatoun, P. McCluskey, M. Ohadi, Embedded Two-Phase Cooling of High Flux Electronics via Micro-Enabled Surfaces and Fluid Delivery Systems (FEEDS), in: ASME 2015 InternationalTechnical Conference and Exhibition on Packaging and Integration of Electronic and Photonic Microsystems collocated with the

ASME 2015 13th InternationalConference on Nanochannels, Microchannels, and Minichannels, 2015, pp. V003T010A012-V003T010A012.

[66] D. McNeil, A. Raeisi, P. Kew, P. Bobbili, A comparison of flow boiling heat-transfer in in-line mini pin fin and plane channel flows, Applied thermal engineering, 30(16) (2010) 2412-2425.

[67] C. Soffientini, G.J. Zyhowski, M.W. Spatz, HFC-245fa: an overview of properties and applications, in: Proceedings of the X European Conference, Latest Technologies in Refrigeration and Air Conditioning under the Auspices of the Italian Ministry of the Environment, 2003, pp. 27-28.

[68] C. Vandervort, A. Bergles, M. Jensen, Heat transfer mechanisms in very high heat flux subcooled boiling, ASME, NEW YORK, NY(USA). 217 (1992) 1-9.

[69] B. Schneider, A. Koşar, Y. Peles, Hydrodynamic cavitation and boiling in refrigerant (R-123) flow inside microchannels, International Journal of Heat and Mass Transfer, 50(13) (2007) 2838-2854.

[70] Comparison of the Volume of Fluid and CLSVOF Methods for the Assessment of Flow Boiling in Silicon Microgaps

[71] P. Asrar, X. Zhang, C.E. Green, M. Bakir, Y.K. Joshi, Flow boiling of R245fa in a microgap with staggered circular cylindrical pin fins, International Journal of Heat and Mass Transfer, 121 (2018) 329-342.

[72] W. Qu, A. Siu-Ho, Liquid single-phase flow in an array of micro-pin-fins—part I: heat transfer characteristics, Journal of heat transfer, 130(12) (2008) 122402.

[73] R.S. Prasher, J. Dirner, J.-Y. Chang, A. Myers, D. Chau, D. He, S. Prstic, Nusselt number and friction factor of staggered arrays of low aspect ratio micropin-fins under cross flow for water as fluid, Journal of heat transfer, 129(2) (2007) 141-153.

[74] Z. Wan, Y. Joshi, Pressure drop and heat transfer characteristics of pin fin enhanced microgaps in single phase microfluidic cooling, International Journal of Heat and Mass Transfer, 115 (2017) 115-126.

[75] W. Qu, I. Mudawar, Measurement and prediction of pressure drop in two-phase micro-channel heat sinks, International Journal of Heat and Mass Transfer, 46(15) (2003) 2737-2753.

[76] D. Chisholm, and Laird, A., Two-phase flow in rough tubes, Trans. ASME, 80(2) (1958) 276-286.

[77] S. Krishnamurthy, Y. Peles, Gas-liquid two-phase flow across a bank of micropillars, Physics of fluids, 19(4) (2007) 043302.

[78] R. Lockhart, R. Martinelli, Proposed correlation of data for isothermal two-phase, two-component flow in pipes, Chem. Eng. Prog, 45(1) (1949) 39-48.

[79] A. Žukauskas, Heat transfer from tubes in crossflow, in: Advances in heat transfer, Elsevier, 1972, pp. 93-160.

[80] A. Koşar, C. Mishra, Y. Peles, Laminar flow across a bank of low aspect ratio micro pin fins, Journal of fluids engineering, 127(3) (2005) 419-430.

[81] W. Qu, A. Siu-Ho, Liquid Single-Phase Flow in an Array of Micro-Pin-Fins—Part II: Pressure Drop Characteristics, Journal of heat transfer, 130(12) (2008) 124501.

[82] J. Tullius, T. Tullius, Y. Bayazitoglu, Optimization of short micro pin fins in minichannels, International Journal of Heat and Mass Transfer, 55(15-16) (2012) 3921-3932.

[83] J.C. Chen, Correlation for boiling heat transfer to saturated fluids in convective flow, Industrial & engineering chemistry process design and development, 5(3) (1966) 322-329.

[84] S.M. Ghiaasiaan, Two-phase flow, boiling, and condensation: in conventional and miniature systems, Cambridge University Press, 2007.

[85] H.-K. Oh, C.-H. Son, Evaporation flow pattern and heat transfer of R-22 and R-134a in small diameter tubes, Heat and Mass Transfer, 47(6) (2011) 703-717.

[86] W. Li, Z. Wu, A general criterion for evaporative heat transfer in micro/mini-channels, International Journal of Heat and Mass Transfer, 53(9-10) (2010) 1967-1976.